

## Department of Precision and Microsystems Engineering

### Design and Testing of a Controllable Hinge for a Flapping-wing Micro Air Vehicle

Tieme Moens

Report no : 2023.023  
Professor : Dr. Ir. J. F. L. Goosen  
Specialisation : SOM  
Type of report : Master Thesis  
Date : 6 April 2023



# Abstract

---

Flying drones have been a well-established field of engineering for many years now. With the wave of bio-inspired design came the idea of flapping wing micro air vehicles (FWMAVs). These drones use flapping wings instead of fixed or rotary wings to generate their lift, giving them the potential for agile movement and application in confined spaces such as search and rescue for example. The Atalanta project is one of the groups trying to create a working and efficient FWMAV. The Atalanta drone operates using a set of four wings attached to a resonating structure actuated by a single linear actuator. While a lot of progress has been made in optimizing the flying motion, the vehicle so far does not have a control mechanism yet. This master thesis seeks to compare methods to achieve this control and propose a final design for a hinge that will be verified experimentally.

A selection of materials and methods for inducing structural changes is tested using analytical models. After picking the most viable options a numerical model seeks to find which of the remaining materials or methods has the highest effectiveness given a set of volume constraints. The most effective design is adapted into a proposed final design for the Atalanta project. The theoretical finalized design fulfills the constraints and functions using a voltage as low as 15 V. To verify the physical principle behind the design experimentally, a few changes are made to the design to allow the construction of a simplistic measurement setup. After the experimental validation it is concluded that the design in its current form is not effective enough to achieve control in the Atalanta FWMAV, and some suggestions are offered to improve the design in future research.

# Contents

---

Abstract.....	i
List of Figures .....	iv
List of Tables .....	vi
Preface .....	vii
1. Introduction .....	1
1.1 Background .....	1
1.2 Micro Air Vehicles .....	1
1.3 The Atalanta project .....	2
1.4 Problem Description .....	4
1.5 Report Outline .....	5
2. Analytical Model .....	6
2.1 The Quasi-Steady Aerodynamic Model .....	6
2.2 The Stiffness Model .....	9
2.2.1 Piezoelectric Materials.....	10
2.2.2 Cross-section Expansion .....	12
2.2.3 Stick-slip Method .....	14
2.3 The Damping Model .....	15
2.4 Conclusions .....	18
3. Numerical Model .....	19
3.1 Piezoelectric Material Designs.....	19
3.2 Cross-section Expansion Designs .....	23
3.3 Stick-slip Method Design .....	26
3.4 Design Variations .....	26
3.4.1 Design Variations of Design 1 .....	27
3.4.2 Design Variations of Design 2 .....	30
3.5 Conclusions .....	35
4. Design Details and Experiment Adaptation .....	37
4.1 Finalization of Design.....	37
4.1.1 Material.....	37
4.1.2 Electric Potential .....	38
4.1.3 Dimensions.....	39
4.1.4 Final Design .....	40
4.2 Experiment Adaptation.....	42
4.2.1 Material.....	42

4.2.2 Electric Potential .....	42
4.2.3 Dimensions.....	43
4.2.4 Experiment Design .....	43
5. Experimental Analysis.....	45
5.1 Goal.....	45
5.1.1 Static Method .....	45
5.1.2 Dynamic Method .....	47
5.2 Methodology .....	48
5.3 Materials.....	52
5.4 Results.....	55
5.4.1 Measurement Processing .....	55
5.4.2 Prototype 1 .....	56
5.4.3 Prototype 2 .....	57
5.4.4 Prototype 3 .....	58
5.4.5 Validation.....	59
5.5 Conclusions .....	60
6. Discussion .....	61
6.1 Key Findings.....	61
6.2 Unexpected Results and Research Limitations.....	63
6.2.1 Unexpected Results .....	63
6.2.2 Research Limitations.....	64
6.3 Research Implications.....	65
7. Conclusions and Recommendations .....	66
References .....	67
Appendix A: Hinge Construction.....	73
Appendix B: Experimental Set-up .....	76

# List of Figures

---

Figure 1: Cross-section of the thorax of an insect in the Diptera order. The red parts are the two muscle groups that transfer energy to the wings by deforming the thorax shell. Image from (Snodgrass, 2018).	2
Figure 2: Atalanta design without actuator. 1) The ring-shaped frames. 2) and 3) are part of the amplification mechanism. 4) is the wing root. 5), 6), 7) and 9) are parts of the wings, and 8) is a crossbar to couple the wings. Image from (Bolsman, 2010).	3
Figure 3: Schematics of the different approaches for controllability. From (Peters, 2016).	4
Figure 4: Visualization of the kinematics of the flapping wing (Wang, 2017).	6
Figure 5: Plot of lift generated in a single wing beat.	8
Figure 6: Stiffness plotted versus total lift.	8
Figure 7: Damping increase plotted versus total lift.	9
Figure 8: Location of the elastic hinge at the wing base.	10
Figure 9: Illustration of the expansion (black arrows) and the potential (red arrow). Image from (Park, 2020).	11
Figure 10: Plot of the electromechanical coupling coefficient versus the stiffness of the hinge.	12
Figure 11: Definition of dimensions of a hollow ellipse cross-section.	13
Figure 12: Relative length of short diameter versus Relative stiffness.	14
Figure 13: Number of layers plotted versus the relative rotational stiffness.	15
Figure 14: Time versus damping moment.	17
Figure 15: Plot of the pitching torque versus time.	17
Figure 16: Design 1 featuring piezoelectric strips at the root of the beam.	20
Figure 17: Design 2 featuring piezoelectric strips sandwiched between two steel plates.	20
Figure 18: Voltage plotted versus relative deformation for Design 1 Scenario 1.	21
Figure 19: Voltage plotted versus relative deformation for Design 1 Scenario 2.	21
Figure 20: Voltage plotted versus relative deformation for Design 2 Scenario 1.	22
Figure 21: Voltage plotted versus relative deformation for Design 2 Scenario 2.	22
Figure 22: Schematic illustration of the three design principles. a) Deformation of hollow rectangular cross-section. b) Curvature deformation of solid rectangular cross-section. c) Uniform cross-section expansion using honeycomb structure material.	23
Figure 23: Design 1 featuring a hollow rectangular cross-section.	24
Figure 24: Design 2 featuring a solid rectangular cross-section.	24
Figure 25: Voltage plotted versus relative deformation for Design 1.	25
Figure 26: Voltage plotted versus relative deformation for Design 2.	25
Figure 27: Pitching amplitude of the wing plotted versus the applied voltage, image from (Wang, 2017).	26
Figure 28: Comparison of first four designs.	27
Figure 29: Design 1 Variation 1.	28
Figure 30: Voltage plotted versus relative deformation for Design 1 Variation 1.	29
Figure 31: Design 1 Variation 2.	29
Figure 32: Voltage plotted versus relative deformation for Design 1 Variation 2.	30
Figure 33: Design 2 Variation 1.	31
Figure 34: Voltage plotted versus relative deformation for Design 2 Variation 1.	31
Figure 35: Design 2 Variation 2.	32
Figure 36: Voltage plotted versus relative deformation for Design 2 Variation 2.	32
Figure 37: Design 2 Variation 3.	33
Figure 38: Voltage plotted versus relative deformation for Design 2 Variation 3.	33
Figure 39: Design 2 Variation 4.	34
Figure 40: Voltage plotted versus relative deformation for Design 2 Variation 4.	34
Figure 41: Comparison Design 1 and its variations.	35

Figure 42: Comparison Design 2 and its variations. ....	36
Figure 43: Relative deformation of design with PVDF. ....	39
Figure 44: Voltage vs relative deformation for an array of different sandwich layer thicknesses. ....	40
Figure 45: Final dimensions as seen from the top. ....	41
Figure 46: Final dimensions as seen from the side. ....	41
Figure 47: Dimensions of experiment design as seen from the top. ....	44
Figure 48: Dimensions of experiment design as seen from the side. ....	44
Figure 49: Angled perspective of experiment design to show contact offset. ....	44
Figure 50: Illustration of the static measurement. ....	46
Figure 51: Difference between minimum and maximum deformations of different design iterations. ....	47
Figure 52: Illustration of the dynamic measurement. ....	48
Figure 53: Example of eigenfrequency determination through a frequency-acceleration plot. Image from (Elshamy, 2018). ....	49
Figure 54: Hinge with additional structure. ....	49
Figure 55: Illustration of mass-spring system. ....	50
Figure 56: Eigenfrequencies of analytical model compared to numerical results. ....	52
Figure 57: Relative eigenfrequencies of analytical model compared to numerical results. ....	52
Figure 58: Schematic depiction of the experimental set-up. ....	53
Figure 59: Experimental set-up with different parts numbered. ....	55
Figure 60: Illustration of data process. ....	56
Figure 61: Frequency vs Displacement for Prototype 1. ....	57
Figure 62: Frequency vs Displacement for Prototype 2. ....	58
Figure 63: Frequency vs Displacement for Prototype 3. ....	59
Figure 64: Repeat of Figure 27, showing pitching amplitude of the wing plotted versus the applied voltage. Image from (Wang, 2017). ....	62
Figure 65: Voltage plotted versus relative stiffness in the research of (Drexhage, 2014). ....	63
Figure 66: Lasea laser cutter. ....	73
Figure 67: The cut shape for the adhesion layer, and the corresponding cut adhesion film (a). b) Shows the cut PVDF film. ....	73
Figure 68: Adhesion layer on top of steel strip, with PVDF film placed in the corresponding hole. ....	74
Figure 69: Laser cut through all layers to form the final shape of the hinge. ....	75
Figure 70: Three final hinge prototypes. ....	75
Figure 71: Schematic drawing of the experimental set-up. ....	76
Figure 72: Photo of the experimental set-up. ....	77
Figure 73: Labview interface. ....	77
Figure 74: Photo of a hinge with additional components glued to it. ....	78
Figure 75: Crocodile clips transferring electric potential to the hinge. ....	79

# List of Tables

---

Table 1: Curated list of methods and materials from literature survey. ....	5
Table 2: Open-circuit and short-circuit stiffness values. ....	11
Table 3: Effectiveness of stiffness methods and materials. ....	18
Table 4: Effectiveness of the designs and their variations. ....	35
Table 5: Recap of changes made in the three characteristic categories. ....	40
Table 6: Recap of changes made to the design for the experimental set-up. ....	43
Table 7: Eigenfrequencies for the modified structure. ....	50
Table 8: Overview of the components used in the experimental set-up. ....	53
Table 9: Eigenfrequency values for a 30 V set-up. ....	55
Table 10: Numerical values for Prototype 1. ....	57
Table 11: Numerical values for Prototype 2. ....	58
Table 12: Numerical values for Prototype 3. ....	58
Table 13: $R^2$ values for the trendlines. ....	59
Table 14: Error estimates for the mean of the average displacement. ....	60
Table 15: Recap of experiment results. ....	60
Table 16: Effectiveness of the different design iterations throughout the research. ....	61
Table 17: Experimental set-up components. ....	76

# Preface

---

This is the report for my master thesis as part of the High-Tech Engineering track of the Mechanical Engineering master at the Delft University of Technology. The project is carried out at the Precision and Microsystems Engineering department under the supervision of Dr. Ir. Hans Goosen.

The thesis is a part of the Atalanta project; A project which aims to design a flapping-wing micro air vehicle (FWMAV). The Atalanta project aims specifically to create a small lightweight flying vehicle which uses the resonance frequency of the vehicle structure to create the flapping motion in four separate wings placed at a 90-degree angle of each other. The use of the resonance frequency minimizes the energy required to fly while the position of the wings allows the vehicle to hover in place rather than needing a forward velocity to be able to fly. This hovering ability is similar to conventional drones using four or more propellers to be able to hover, but has the benefit that the system can be designed to be much more lightweight and due to the structure of the system can be actuated using a single linear actuator. The resonance system is based on real life, where insects use similar structures in their exoskeletons to be able to fly very efficiently and achieve spectacular maneuverability.

What drew me to the project was the opportunity for a more design-based thesis, as opposed to the often very theoretical nature of mechanics studies. The idea of working on a part of a project to later see that part physically applied in real life is something that I always liked. I hope my contributions to this project will help other students in the future to perfect the design and hopefully one day get a prototype in the air!

So, without further ado, let's get in to the report. I hope you enjoy reading it!

# 1. Introduction

---

## 1.1 Background

Drones are becoming more and more of a common sight these days. Their applications range from monitoring fertilizing rate and crop growth (Hedley, 2015), to delivery of medical supplies to remote environments (Ling, 2019) and military applications (Kindervater, 2016). Other uses might include surveying of roads and pipelines, humanitarian and security assessment at disaster sites and monitoring construction progress (Floreano, 2015). In all these fields drones have established themselves as a useful technology by being lightweight, flexible, easy to deploy, autonomous and airborne.

Drones are defined as flying vehicles not carrying a human operator (Hassanalian, 2017), but this definition leaves a lot of room for variation. Drones can use different forms of propulsion and lift generating techniques and can vary in size a lot. This master thesis focusses on a specific type of drone, a Flapping Wing Micro Air Vehicle (FWMAV) known as Atalanta. The Atalanta project is a continuous research collaboration between students, PhD candidates and professors of different engineering fields, of which this thesis is but a small part. The Atalanta drone falls into the Micro Air Vehicles (MAV) subset of the Pico Air Vehicles category, which is defined to have a maximum wingspan of 15cm. The main focus of this category is vehicles with low weight, high flexibility and high maneuverability (Ward, 2017).

## 1.2 Micro Air Vehicles

Within the subcategory of MAVs there are once again a number of variations in design. The most important distinction between different MAV projects is its lift generation system. By far the most common sight for drones is a rotary wing mechanism, which functions similarly to a helicopter, generating lift using one or more spinning blades. In recent years these MAVs, usually sporting multiple rotors (quadcopters, octocopters, etc.), have risen hugely in popularity due to their stability, maneuverability and ease in remote piloting (Ward, 2017). However, these rotary MAVs suffer from low lift-to-drag ratio and problems in flight control when scaled down to sizes of only a few centimeters (Liu, 2016). A second lift generating method for drones is based on probably the most common design of flight machines used, the fixed wing MAVs. These drones use wings that are rigidly attached to the body structure and generate a forward motion which creates an airflow over the wings, achieving flight. Studies as early as 2007 were able to design fixed wing MAVs with a wingspan of 15 centimeter and a weight of 65 grams, showing that the concept was able to scale down (Lin, 2007). However, at smaller sizes the fixed-wing MAVs also suffer from the same problems in lift-to-drag ratio and maneuverability (Liu, 2016). On top of this fixed-wing MAVs have problems functioning in confined spaces due to the constantly needed forward motion to generate lift.

So, if small energy-efficient drones are required that are able to maneuver confined spaces and hover in place to collect data or monitor a situation what option is left? In recent years there has been a sharp increase in research done into flapping-wing MAVs (Ward, 2015) - (Farrell-Helbling, 2018). These flapping-wing mechanisms are bio-inspired, and when scaled down to insect scale can overcome some of the challenges the other two categories struggle with, such as taking advantage of unsteady fluid effects. Wing inversions during the stroking motion can result in augmented lift and the flapping-wing motion allows for angles of attack can greatly exceed angles of attack that would result in stall for conventional fixed-wing aircrafts (Farrell-Helbling, 2018). For this reason, a number of research groups have invested time into developing prototypes for flapping-wing MAVs, including the Atalanta project.

### 1.3 The Atalanta project

Although there is still much to learn from nature, several groups have successfully built flying prototypes of FWMAVs. For example, the CalTech microbat, which is a palm-sized ornithopter that achieved flight as early as October 1998. This prototype achieved flight for 42 seconds while weighing approximately 12.5 grams. It is capable of turning left and right and can pitch up and down (Pornsin-Sirirak, 2001). There is also the DelFly Nimble, which can achieve stationary hover flight and move in any direction in a rapid and smooth manner. It has a wingspan of 33 cm and weighs 28.2 g, and is able to fly for 5 minutes on a single battery (Karásek, 2018). Finally, a bit more relevant to the Atalanta project as will be seen later is a FWMAV which achieves a high efficiency using resonance driven system. This prototype weighs 2.7 g and achieved tethered liftoff (Hines, 2013).

Similarly, to these other research groups the Atalanta project is a FWMAV from the Delft University of technology which has a wingspan of 10 cm and a weight of 8.85 g (Bolsman, 2010). However, it differs from the previous research projects in a number of ways. Unlike the CalTech Microbat, the Atalanta project is capable of hovering in place. Unlike the DelFly nimble, the Atalanta project uses a resonance system to drive its wings. And unlike the resonance based FWMAV in (Hines, 2013), the Atalanta project uses four wings for increased stability, and uses one single actuator to drive all four wings simultaneously to save on weight.

The idea of using resonance to drive the wings of a FWMAV is taken from nature, specifically insects. Insects are among the nimblest flyers in nature, being able to achieve feats such as landing upside down or evading fly swatters. So how can one achieve this maneuverability and control in a mechanical system? The two most important factors for the flight performance of insects are the thorax and their wings. The mechanical energy generated in muscles is transferred through the thorax to the wings, see Figure 1.

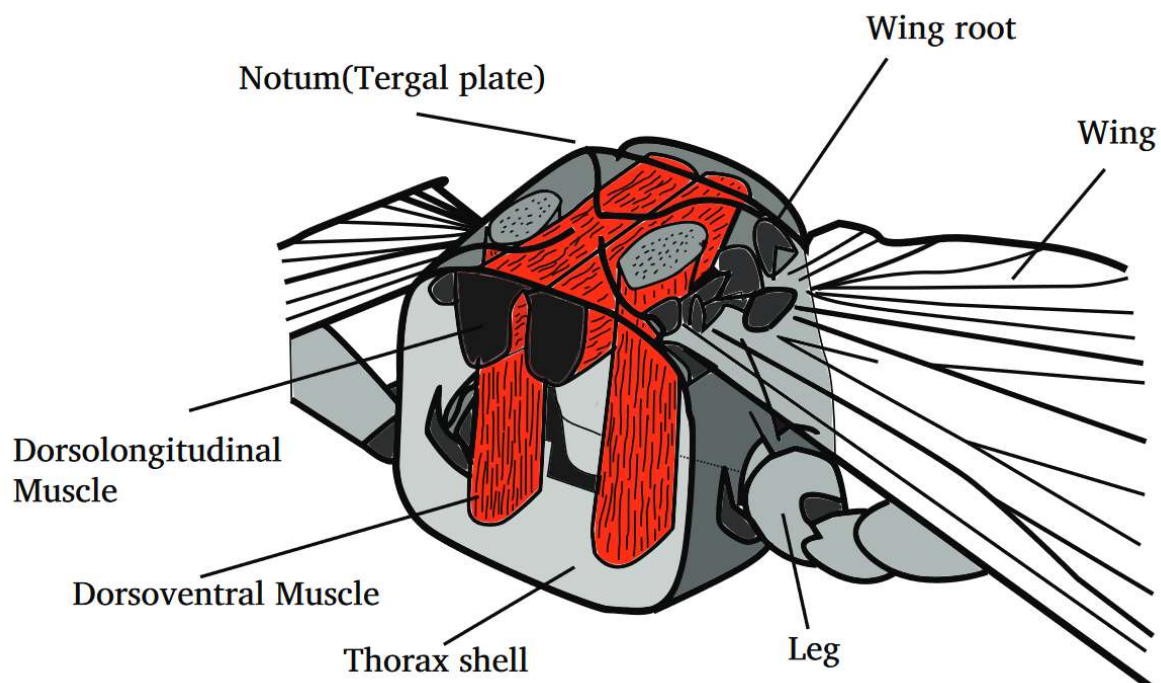


Figure 1: Cross-section of the thorax of an insect in the Diptera order. The red parts are the two muscle groups that transfer energy to the wings by deforming the thorax shell. Image from (Snodgrass, 2018).

The working principle of this system can be described as a driven damped oscillator. The muscles deform the thorax in a rhythmic manner which coincides with the natural frequency of the system. The thorax then transfers this energy to the wings through the wing root (Greenewalt, 1960).

The Atalanta project takes inspiration from this working principle and operates a similar system. Firstly, there is a singular actuator situated in the middle of the system. This actuator mimics the muscle groups in the insect body and actuates all four wings simultaneously. Secondly, there is the ring-shaped frame. This frame mimics the thorax shell, and is actuated in its lowest eigenfrequency by the actuator. Thirdly, there is a compliant four bar mechanism. This mechanism translates and amplifies the deformation of the ring frame to produce a sweeping motion for the wings (Greenewalt, 1960). Lastly, there is the wings themselves, attached to the frame using an artificial wing root consisting of polystyrene and spring steel (Diekerhof, 2016). The design without the actuator is visible in Figure 2.

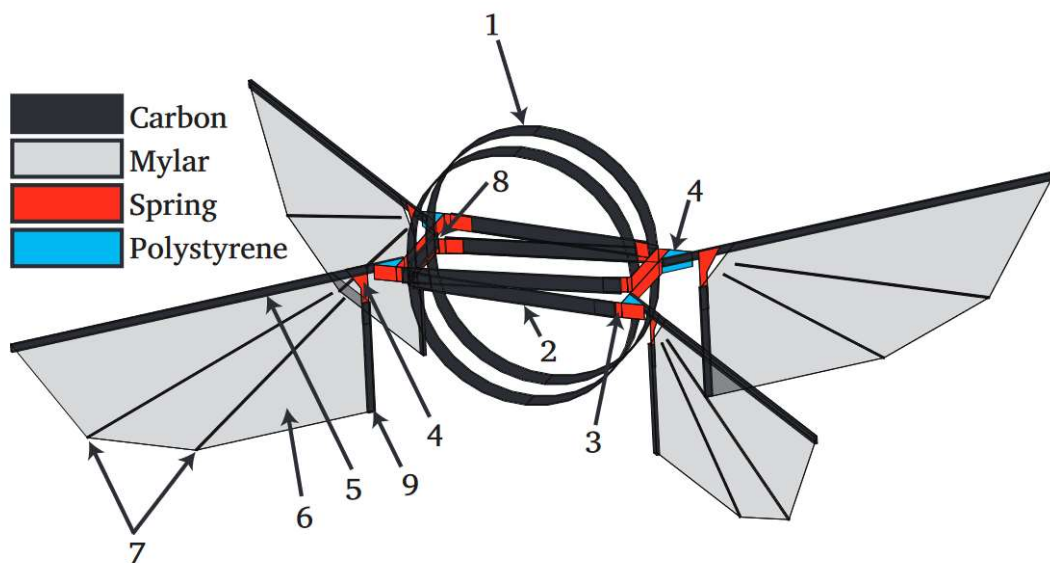


Figure 2: Atalanta design without actuator. 1) The ring-shaped frames. 2) and 3) are part of the amplification mechanism. 4) is the wing root. 5), 6), 7) and 9) are parts of the wings, and 8) is a crossbar to couple the wings. Image from (Bolsman, 2010).

The reason resonance is an important factor in the design is because using resonance will decrease the power required to operate the drone, which is a huge benefit to a vehicle which aims to be as small and lightweight as possible. The power required by a FWMAV to fly can be split into three components (Wang 2017):

1. Aerodynamic power to overcome the aerodynamic drag on the wings
2. Inertial power to accelerate the wings and the air around them
3. Elastic power to compensate for the elastic deformations of the structure

The use of resonance means that energy is continuously stored in the ring-shaped frames which causes both the elastic and inertial power to average out to zero over every cycle (Bolsman, 2010). This means that component 2 and 3 can be neglected and the actuator only needs to generate enough power to overcome the aerodynamic drag on the wings. Through this principle the drone can be designed with a smaller and less powerful actuator. The resonance system, and with it the compliant parts, also allow for a lower complexity of the system and reduced frictional losses (Ras, 2019).

## 1.4 Problem Description

The astute reader may have already noticed a fairly integral part missing from the design if controlled flight is to be achieved. Aside from controllers and cameras to allow remote controlled or autonomous flight an even more basic problem in controllability presents itself. If the vehicle uses only a single actuator that drives all four wings in the same eigenfrequency through the resonance structure, this means all wings will in theory be generating an equal amount of lift at all times. This means that while the vehicle would be able to hover, there is no way to steer or balance the vehicle.

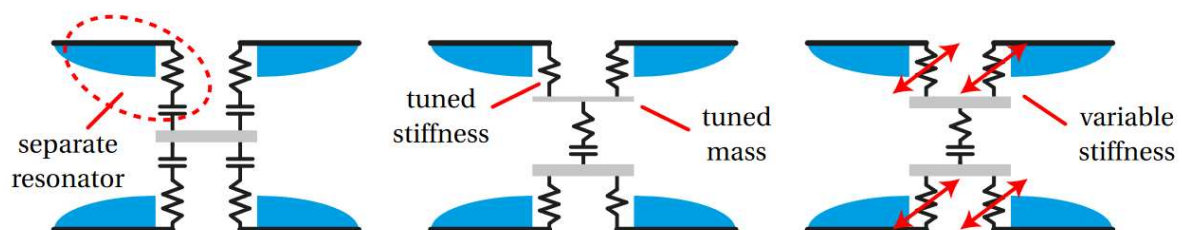
A traditional aviation approach would be to add advanced components or systems dedicated to control (for instance the tail rotor of a helicopter) or to change the structural geometry (for instance aircraft wing-flaps). However, since the aim of the project is to design a FWMAV as small and lightweight as possible, these options become less and less attractive. Not only would integrating advanced systems significantly increase the weight, but a lot of systems commonly used in large scale aviation do not scale down very well. And so, the aim of the master thesis which will follow up this literature survey is to find a simple lightweight controllability method for the Atalanta project.

Within the Atalanta project there has already been a PhD thesis written that focusses on this subject (Peters, 2016). In this report Peters outlines three approaches for controllability, illustrated in Figure 3.

**Approach A:** Divide the resonant system into several coupled resonators which allow for a difference in actuation.

**Approach B:** Proper tuning of the mass and stiffness distribution of the basic resonant system to introduce different resonance responses corresponding to different driving frequencies.

**Approach C:** Induce structural property changes to parts of the basic resonant system to modify the resonance response.



(a) **Approach A:** divide basic resonant system in separate, individually controllable resonators.

(b) **Approach B:** well-tuned property distribution resulting in multiple resonance responses.

(c) **Approach C:** induce structural property changes to modify the resonance response.

Figure 3: Schematics of the different approaches for controllability. From (Peters, 2016).

For the sake of not wanting to do too much, this master thesis will focus solely on **approach C**, since this approach seems to have the most elegant and efficient solutions for a lightweight vehicle. He also recommended for the change in structural properties to be placed in the hinges at the wing bases, as he theorized that that would give the biggest change in amplitude. The literature survey preceding this master thesis focused on collecting as many materials and methods that allow the change of structural properties in the hinge, and executing a multi-round elimination process to produce a curated list of the most promising materials and methods. The results of this elimination process are detailed in Table 1.

Table 1: Curated list of methods and materials from literature survey.

<b>Materials</b>	
1.	Electrorheological Fluids
2.	Magnetorheological Fluids
3.	Piezoelectric Materials
<b>Methods</b>	
1.	Cross-section Expansion
2.	Stick-Slip Method

Using a threshold of a change in lift of 0.5% as set by (Lu, 2013) the goal is to find out which of these methods and materials are most effective at inducing this change in lift, and what kind of design can be created that can be incorporated in the Atalanta project.

## 1.5 Report Outline

In this thesis another elimination process will be executed. First, analytical models will be set up, as detailed in Chapter 2. After that, in Chapter 3, a numerical analysis is done using COMSOL Multiphysics. After each of these steps, a selection is made of the best performing materials and methods and the most promising ones advance to the next round. After the numerical analysis, the most effective material or method is picked and a more detailed design is made, which is done in Chapter 4. To test the final design in a physical way, an experiment is carried out to see if the design performs as expected and is indeed a viable option for achieving control in the Atalanta project. The experiment and its results are detailed in Chapter 5. Chapter 6 discusses the research, detailing its key findings, unexpected results, limitations and implications. Chapter 7 forms the conclusion, in which a brief overview of the research is given and recommendations are made for future researchers, both within the Atalanta project and outside of it. In the appendix, Appendix A details the construction of the hinge prototypes, and Appendix B shows how the experiment was executed.

## 2. Analytical Model

In this chapter, an existing analytical model is analyzed and built upon to gain insight into the precise effectiveness of the change in structural properties induced by the methods and materials selected by the literature survey. The analytical model simulates a single wing beat by the Atalanta project, from which aerodynamic properties such as the lift and the drag can be derived. Using this model, we can get a clear idea of how much structural change needs to be induced to achieve control. Knowing this, we then set up a number of analytical calculations to see which methods and materials show the most promise.

In the first section, the model for simulating the aerodynamics of the Atalanta project is discussed. Section 2.2 calculates a number of stiffness parameters for the methods and materials based on stiffness. A similar process is then followed for the materials based on damping in Section 2.3. The results are compared in Section 2.4 and a selection of the most promising materials and methods is taken into the next step of the research process.

### 2.1 The Quasi-Steady Aerodynamic Model

The base model for this analytical chapter is a model built by a PhD student within the Atalanta project, Qi Wang (Wang, 2017). The model is a quasi-steady model, which means it takes into consideration the change of the angle of attack over time and the velocity variation over the wingspan (Ellington, 1984). The model includes four aerodynamic loading terms, which result from the wings translation, its rotation, their coupling and the added-mass effect. The ultimate goal of the model is to be able to predict the aerodynamic force and torque of the wing.

To properly describe the movement of the wing a summation of successive wing rotations is used, seen in Figure 4. This method is shown using the “cans in series” approach (Schwabb, 2006).

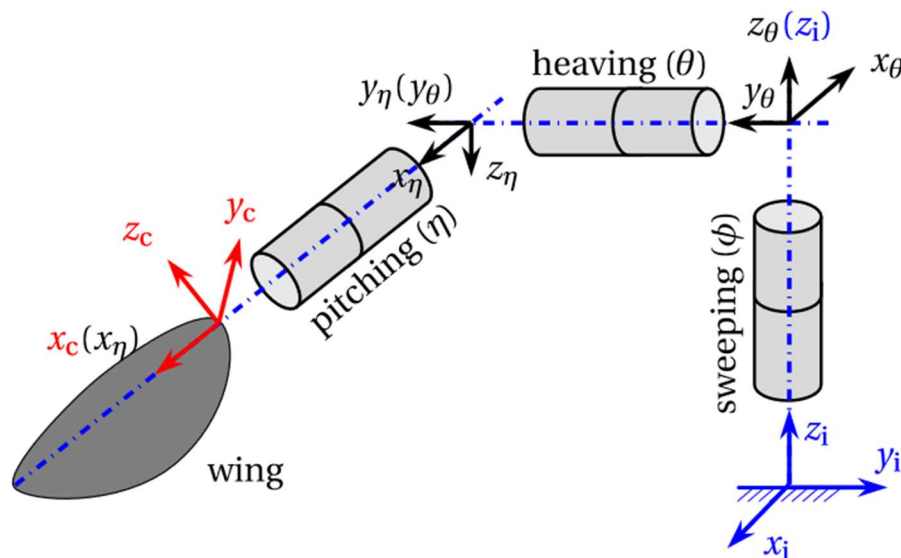


Figure 4: Visualization of the kinematics of the flapping wing (Wang, 2017).

The most important part is that the flapping motion is quantified using three Euler angles: sweeping angle  $\phi$ , heaving angle  $\theta$  and pitching angle  $\eta$ . For the methods and materials based on stiffness, the rotational stiffness in the pitching direction will be used, see Section 2.2. This rotational stiffness is integrated into the model in two places. The first is in the elastic power  $P^{elas}$ , given in Equation 2-1,

which is one of three power components which form the total power consumption of a flapping wing with passive pitching, together with the aerodynamic power and the inertial power.

$$P^{elas} = k_{\eta}\eta\omega_{xc}. \quad (2-1)$$

Here  $k_{\eta}$  is the rotational stiffness in pitching direction,  $\eta$  is the pitching angle as shown in Figure 4, and  $\omega_{xc}$  is the rotational velocity about the x axis in the co-rotating frame, also shown in Figure 4.

The second place  $k_{\eta}$  can be found is in the elastic torque  $\tau^{elas}$  (Equation 2-2), which is integrated into the equations of motion.

$$\tau^{elas} = -k_{\eta}\eta. \quad (2-2)$$

For the aerodynamic modelling, the most relevant forces are the translational and rotational forces on the wing. Wang first defines the drag coefficient on the wing as a function of the translational lift coefficient.

$$C_D^{trans} = C_L^{trans} * \tan(\tilde{\alpha}). \quad (2-3)$$

Here  $C_d^{trans}$  is the translational drag coefficient,  $C_L^{trans}$  is the translational lift coefficient, and  $\tilde{\alpha}$  is the angle of attack for a rigid wing model. This method does neglect the viscous drag at the boundary layer but due to the nature of the angle of attack of flapping wings its contribution is small.

So far this approach only considers the drag coefficient for pure translation normal to the flow. An adjustment is made to incorporate the rotational movement of the wing into the drag coefficient, as shown in Equation 2-4.

$$C_D^{rot} = C_d^{trans} \frac{2\pi * A}{2 + \sqrt{A^2 + 4}}. \quad (2-4)$$

Here  $C_D^{rot}$  is the rotational drag coefficient and  $A$  the aspect ratio of the wing. For the materials based on damping, an additive factor to this drag coefficient will be used to simulate damping of the hinge, see Section 2.3.

Finally, there is the rotational torque about the pitching axis, which will also be used in Section 2.3. This torque is calculated using Equation 2-5 which is based on research done by (Andersen, 2005).

$$\tau_{zc}^{rot} = -\frac{\rho^f}{2} \omega_{xc} |\omega_{xc}| C_D^{rot} \int_0^R \int_{\hat{d}c-c}^{\hat{d}c} z_c |z_c| x_c dz_c dx_c. \quad (2-5)$$

Here  $\omega_{xc}$  is the rotational velocity around the x-axis of the co-rotating frame (shown in Figure 4),  $\hat{d}$  is a local-chord-normalized distance from the leading edge to the pitching axis,  $c$  is the chord length,  $z_c$  and  $x_c$  are the z and x coordinate in the co-rotating frame (also shown in Figure 4), and finally  $\rho^f$  is the fluid density.

With all its components, the model is able to generate a tremendous amount of output, of which in this report mostly the lift is considered. The lift for a single wing beat is shown in Figure 5.

By taking the area under this graph the total amount of lift for a wing beat can be defined. According to (Lu, 2013), changing the lift force by more than half a percent should be sufficient to achieve control in the FWMAV. Changing the stiffness and plotting the absolute lift generated gives Figure 6.

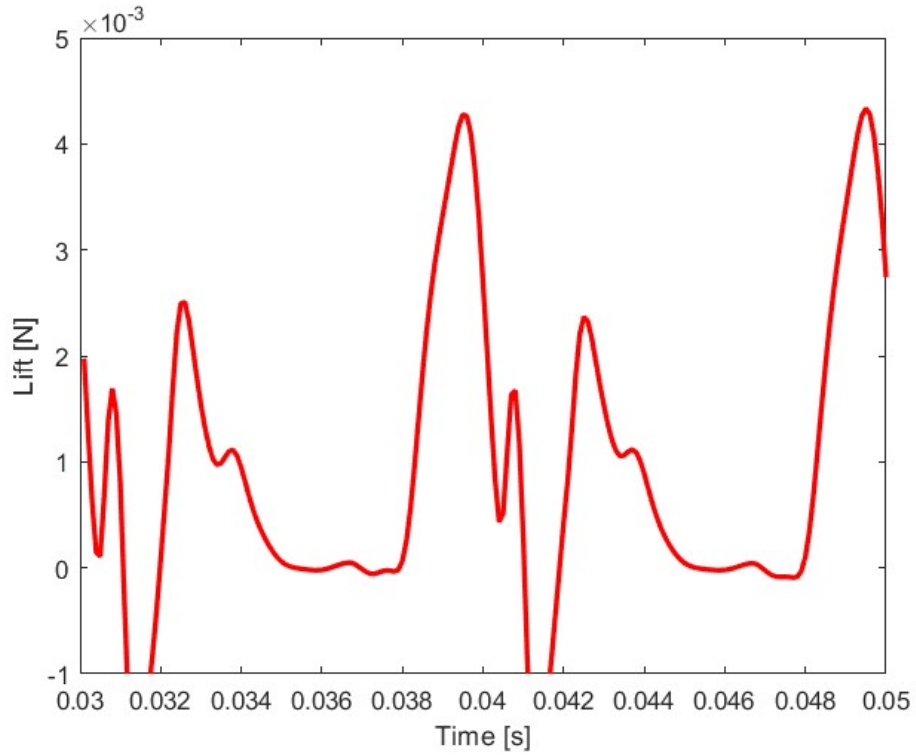


Figure 5: Plot of lift generated in a single wing beat.

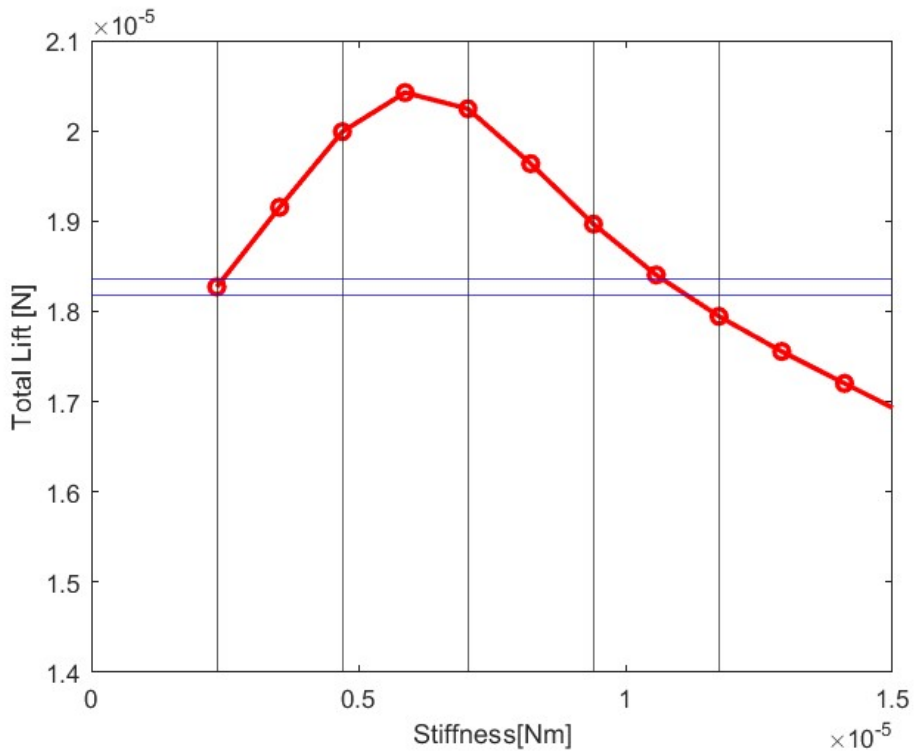


Figure 6: Stiffness plotted versus total lift.

Here the two blue lines represent a lift change of 0.5% and the black lines represent a 100% increase of the stiffness, up to 500%. From this figure it is clear that only a small change in stiffness is required to

achieve the 0.5% change in lift, a stiffness change of 5.15% to be precise. A similar figure can be produced for the damping, shown in Figure 7.

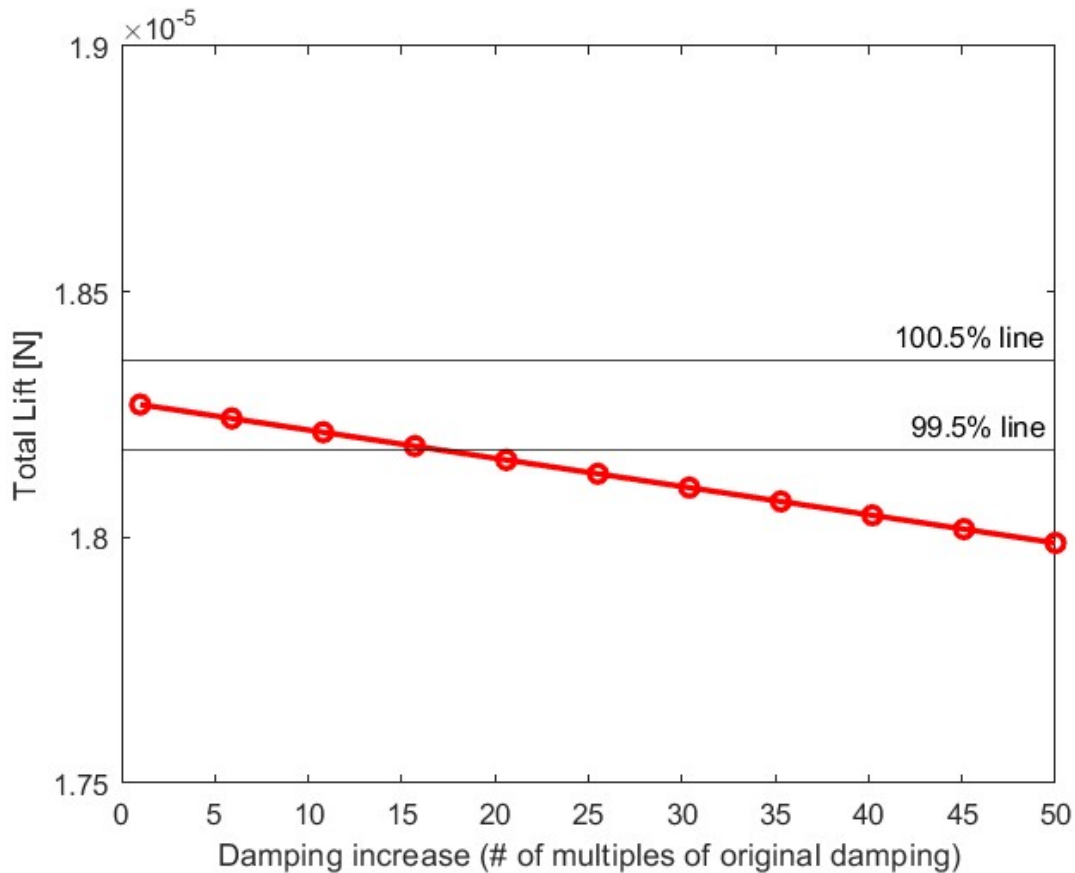


Figure 7: Damping increase plotted versus total lift.

For the damping a much larger increase of about 15x the original damping is needed. It is also important to note that this graph takes the original damping of the entire wing instead of just the hinge, as the hinge damping is not yet built into the model. The real increase in damping is therefore going to have to be even larger.

## 2.2 The Stiffness Model

Both insects and FWMAV's show a myriad of different shapes and stiffness distributions for the wings. One thing that is commonly the case is that the pitching motion of the wing is generated passively using the flexibility of the wing (Wang, 2017). For this, insects use a flexible membrane structure (Dudley, 2002). In FWMAV's this can be emulated using a polymer film reinforced with carbon fiber (De Croon, 2009), or by using an elastically deforming hinge at the base of the wing to simulate the wing stiffness (Wood, 2007). In this section the latter method is used.

The materials and methods that were selected in the literature survey and carried over into this master thesis can be divided into two categories based on the way they influence the mechanical properties of the hinge. In this section we will be looking at modelling the methods and materials that influence the stiffness. These are the piezoelectric materials, the stick-slip method and the cross-section expansion. Since we want to be able compare these materials and methods a standard hinge dimension is used, consisting of length  $L = 5 \text{ mm}$ , width  $d = 12.7 \text{ mm}$  and thickness  $t = 40 \text{ }\mu\text{m}$ . Figure 8 shows the elastic hinge at the base of the wing attached to the wing holder. According to (Howell, 2001) the rotational stiffness for this hinge, which is a compliant hinge loaded in bending, is given by Equation 2-6.

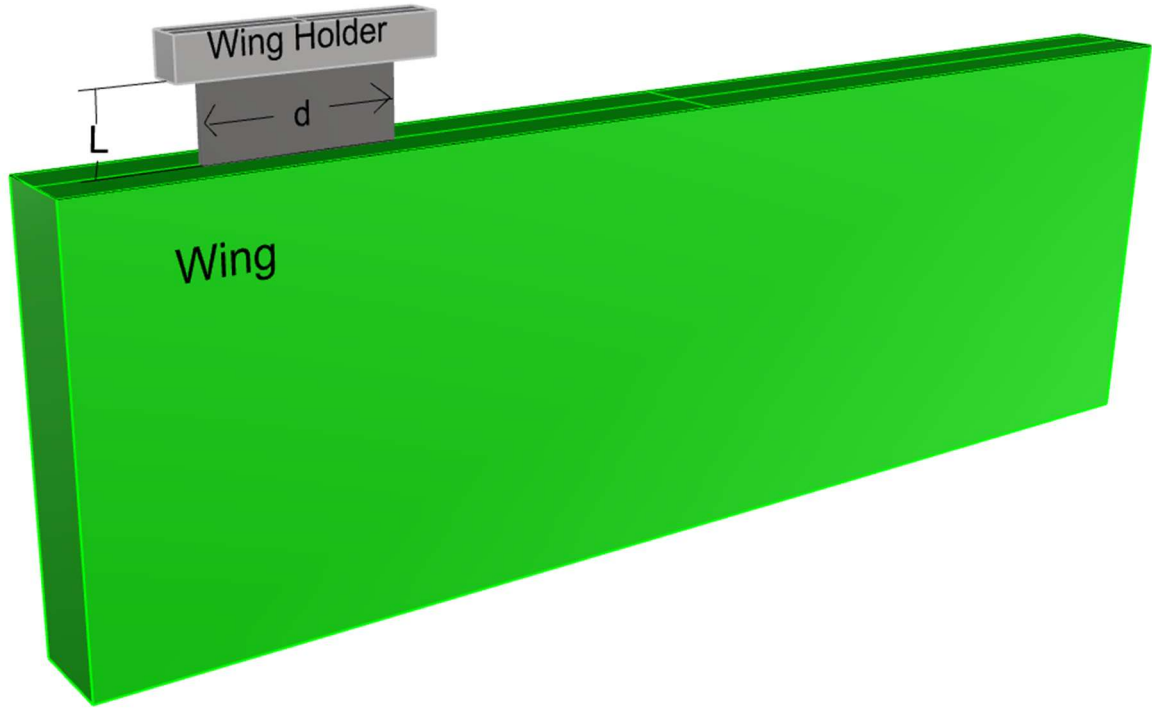


Figure 8: Location of the elastic hinge at the wing base.

$$k_{rot} = \frac{EI}{L}. \quad (2-6)$$

Here  $E$  is the Young's modulus of the hinge and  $I$  is the second moment of area of the hinge. Expressed in terms of the dimensions of the hinge this equation becomes:

$$k_{rot} = \frac{Et^3d}{12L}. \quad (2-7)$$

With this foundation we will now look at the specific methods and materials.

### 2.2.1 Piezoelectric Materials

Piezoelectric materials are nowadays widely used in various micro to nano motion applications, over a large number of technical fields (Sabarianand, 2020). They operate based on their electrical boundary conditions, for instance short circuit, resistive circuit and open circuit. How this affects the stiffness of the material is explored in (Ramaratnam, 2004). Ramaratnam poses that a beam with a piezoelectric film attached to it has a stiffness as detailed in Equation 2-8.

$$EI(x) = EI^b + EI^p * S(x). \quad (2-8)$$

Here  $EI^b$  is the product of the Young's modulus and second moment of area of the beam,  $EI^p$  is the same product for the piezoelectric material, and  $S(x)$  is a function defined as:

$$S(x) = H(x - x_1) - H(x - x_2). \quad (2-9)$$

Here  $H(x - x_1)$  and  $H(x - x_2)$  are Heaviside functions that represent the placement of the piezoelectric strip on the beam.

Two different parameters for elasticity are used, based on the electrical boundary conditions for the piezoelectric material. In a short-circuit mode the product of the Young's modulus and the second moment of area is simply  $EI^p$ , but in open-circuit condition it is defined as:

$$\frac{EI^P}{(1-k_{31}^2)} \quad (2-10)$$

This equation introduces  $k_{31}$ , the 31-component of the electromechanical coupling matrix. This coefficient relates the expansion in length direction orthogonal to an applied potential, as shown in Figure 9 (Park, 2020). The  $k_{31}$  coefficient differs per material and can range from 0.02 (Warner, 1967) to 0.60 (Ye, 2008). Generally, the coupling factor for ceramic piezoelectric materials is significantly higher than for piezoelectric polymers, at the cost of flexibility (Preumont, 2018).

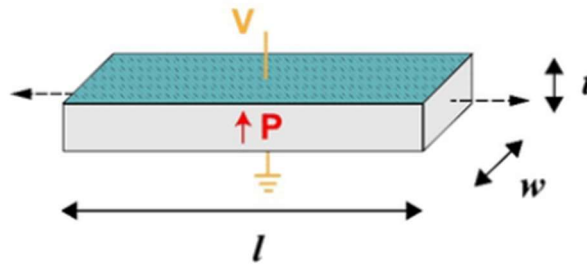


Figure 9: Illustration of the expansion (black arrows) and the potential (red arrow). Image from (Park, 2020).

Table 2: Open-circuit and short-circuit stiffness values.

<b>Electromechanical coupling coefficient</b> $k_{31}$ [-]	<b>Material</b>	<b>Open-circuit stiffness [Nm]</b>	<b>Short-circuit stiffness [Nm]</b>	<b>Sources</b>
0.020	Lithium Niobate	0.0010	0.0010	(Korth Kristalle, 2022)
0.181	Zinc Oxide	0.0002	0.0002	(Desai, 2008)
0.315	Barium Titanate	0.0006	0.0006	(Cordero, 2018)
0.490	Barium Titanate	0.0007	0.0006	(Cordero, 2018)
0.600	Lead Zirconate Titanate	0.0075	0.0048	(Nazeer, 2009)

With the dimensions and underlying principles known a calculation can now be made for the stiffness change. For this part a hinge is considered consisting of a  $10 \mu\text{m}$  layer of steel with a  $30 \mu\text{m}$  piezoelectric film covering the whole surface. The open-circuit and short-circuit stiffnesses of this hinge for the range of values for the electromechanical coupling coefficient  $k_{31}$  are shown in Table 2.

These values are also presented in chart format in Figure 10.

Due to the usage of different materials the short-circuit stiffness varies slightly but there is a clear trend showing an increasing effectiveness the higher the electromechanical coupling coefficient gets. This trend makes sense when considering Equation 2-10, as  $1 - k_{31}^2$  is in the denominator, meaning the closer  $k_{31}$  is to 1 the bigger the change in stiffness is going to be.

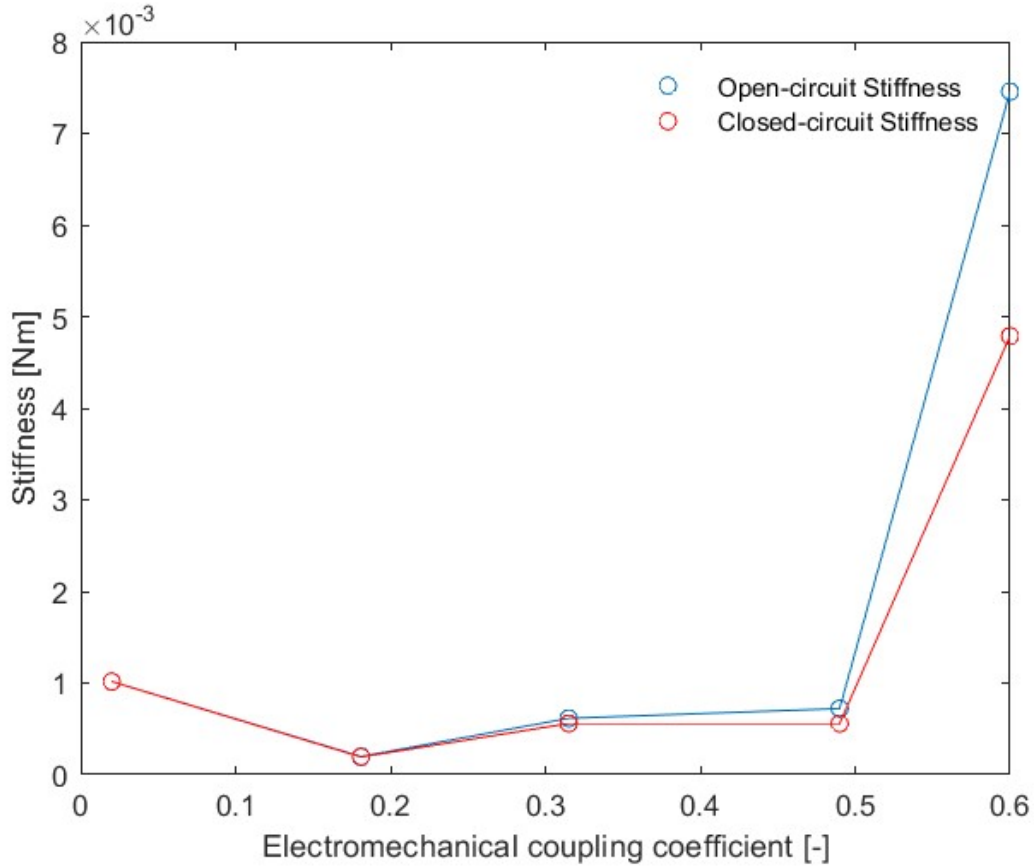


Figure 10: Plot of the electromechanical coupling coefficient versus the stiffness of the hinge.

### 2.2.2 Cross-section Expansion

From elementary beam theory we know that the relation between applied bending moment and beam deflection is as follows.

$$M = EI \frac{d^2w}{dx^2}, \quad (2-11)$$

where  $M$  is the bending moment,  $E$  is the Young's modulus,  $I$  is the second moment of area,  $w$  is the deflection and  $x$  is the distance along the beam. From this formula it can be seen that this relationship depends on the second moment of area, which in turn depends on the cross-sectional area of the beam. There are a few methods to influence this cross-sectional area, but this section will focus on the effect this change in cross-sectional area can have. Calculating second area moments for deformed geometries analytically is often times hard because few analytical formulations for deformation of complex structures exist. Research like (Paulsen, 2001) describes the deformation of a hollow rectangular cross-section but these focus on plastic deformation in a pre-buckling stage. To simplify the calculations for this section while still properly testing the effect of a cross-sectional expansion a hollow ellipse cross-section is used which is assumed to be made from a theoretical incompressible steel type. This incompressibility says that while the cross-section can deform, its area stays the same. This creates a relation between the reduction in length of one of the axes and the increase in length of the other. The area of an ellipse is given as:

$$A = \pi \frac{a}{2} \frac{b}{2}. \quad (2-12)$$

Where  $a$  is the long diameter and  $b$  is the short diameter of the ellipse. Now we imagine an ellipse in undeformed configuration with area  $A_u$ , long diameter  $a_u$  and short diameter  $b_u$ . If the length of the long axis reduces by 10%, or:

$$a_d = 0.9a_u, \quad (2-13)$$

we can deduce a relationship between the undeformed and deformed short diameter by setting the areas of the undeformed and deformed ellipses equal to each other, shown in Equations 2-14 to 2-18.

$$A_u = A_d. \quad (2-14)$$

$$\frac{\pi}{4}a_u b_u = \frac{\pi}{4}a_d b_d. \quad (2-15)$$

Divide out  $\frac{\pi}{4}$  and substitute Equation 2-13:

$$a_u b_u = 0.9a_u b_d. \quad (2-16)$$

$$b_u = 0.9b_d. \quad (2-17)$$

$$b_d = 1.11\bar{1}b_u. \quad (2-18)$$

Equations 2-17 and 2-18 show that if we reduce the length of one axis by 10 percent, we have to increase the length of the other by an inversely proportional percentage to conserve the area. Since a hollow ellipse cross-section consists of the difference between two ellipses, as long as the area of both these ellipses stays the same the area of the difference will also stay the same. Using this and the formulation for the second area moment of a hollow ellipse given in Equation 2-19 with dimensions shown in Figure 11, we can calculate the change in bending stiffness for an expanding ellipse cross-section.

$$I_x = \frac{\pi(ab^3 - a_1 b_1^3)}{64}. \quad (2-19)$$

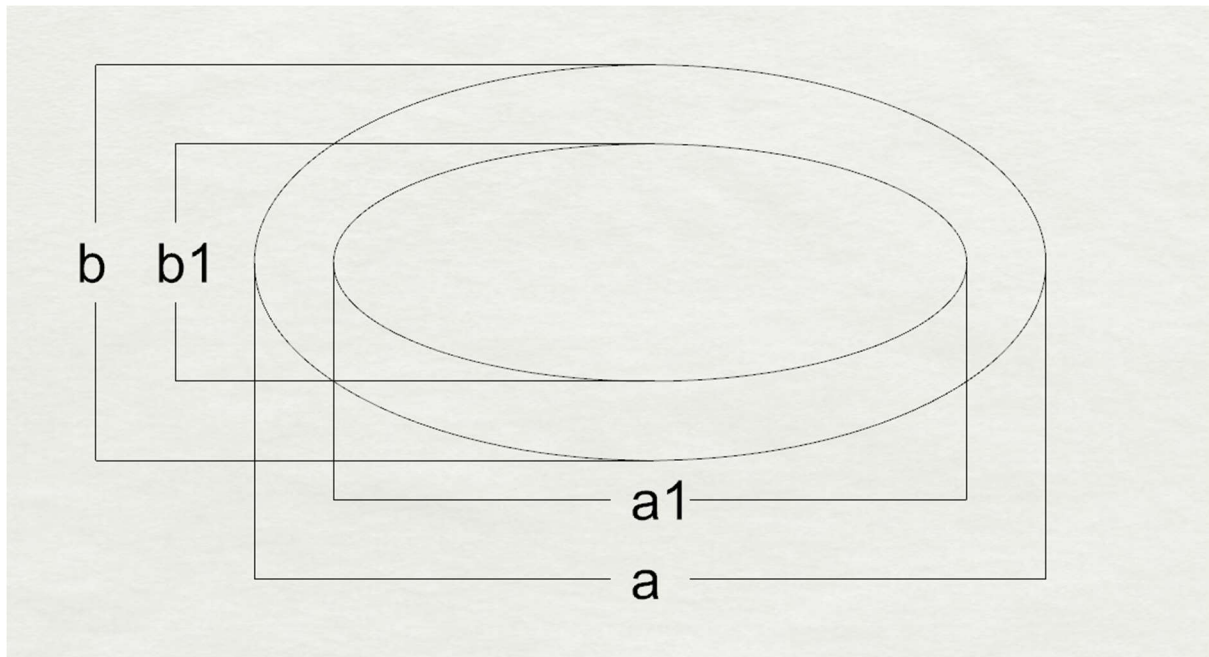


Figure 11: Definition of dimensions of a hollow ellipse cross-section.

For this analytical calculation, the second area moment of the cross-section will be calculated by simulating the long diameter of the ellipse being reduced in length from 0% to 20%. While there are

many different ways to change the cross-sectional area this number is taken from modern piezo actuator achievable strain rates (Ueda, 2009). The dimensions of the cross-section will be similar to the dimensions mentioned in the previous section, with  $a = 12.7 \text{ mm}$ ,  $b = 40 \mu\text{m}$ ,  $a_1 = 12.68 \text{ mm}$  and  $b_1 = 20 \mu\text{m}$ . The results of this calculation are shown in Figure 12.

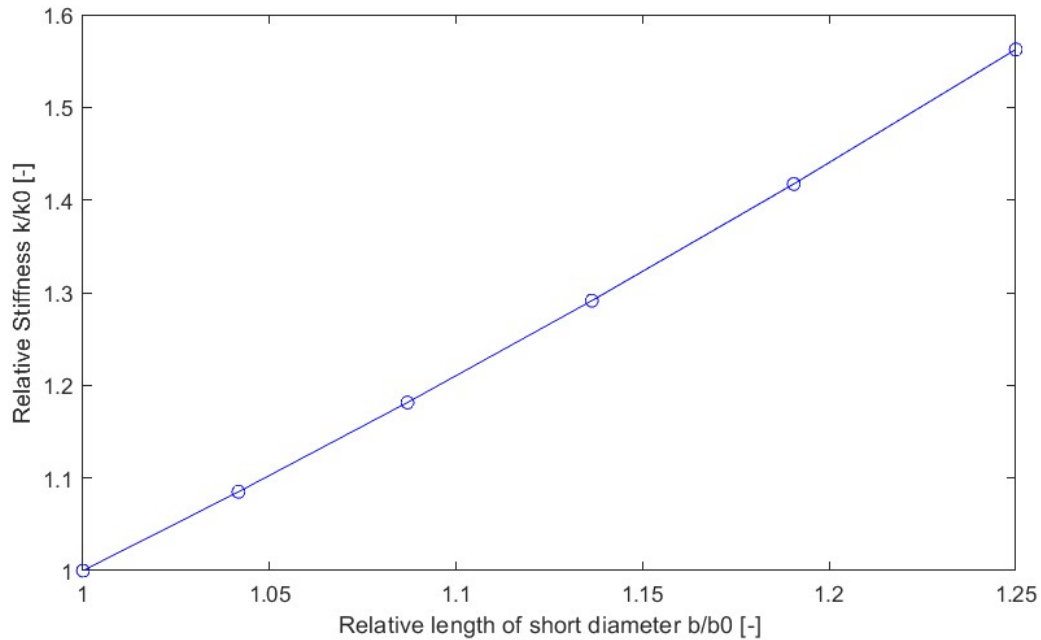


Figure 12: Relative length of short diameter versus Relative stiffness.

With this method a change in stiffness of almost 60% can be achieved. This is less than the change in stiffness in the previous section but the results do look to be more consistent.

### 2.2.3 Stick-slip Method

The literature survey discusses another method within the cross-section expansion section, which is later taken as a separate method due to the promising results in recent research (Tabata, 2001) and its high theoretical effectiveness (Wang, 2017). This method is known as the Stick-slip method and its effect is based on the principle of friction between different layers of for instance a cantilever beam. In an inactivated condition, the layers of the beam slide over each other and the stiffness of the beam is little more than the individual stiffness of one layer. However, when activated, whether it be through electrostatic force (Tabata, 2001), pressure differences (Kawamura, 2002), shape memory wires (Murray, 2009) or variable core stiffness (Henke, 2014), the stiffness of the beam becomes close or equal to the combined stiffness of all layers together. This is due to the induced forces between layers increasing the friction forces and making the layers “stick” together instead of “slipping” over each other.

The formulas dictating the basic change in bending stiffness are given in Equations 2-20 and 2-21.

$$A_{stick} = A_{slip} = nbt. \quad (2-20)$$

$$I_{stick} = n^3 \frac{bt^3}{12} > I_{slip} = n \frac{bt^3}{12}. \quad (2-21)$$

Here  $A$  indicates the area,  $I$  is the second moment of area,  $n$  is the number of layers and  $b$  and  $t$  are the width and thickness of the layers respectively. These equations show that the area of the beam stays the same but the method offers a quadratic relationship between the bending stiffness and the number of layers. For the calculation we will once again take a rectangular beam of cross-section  $12.7 \text{ mm}$  by

40  $\mu\text{m}$ . The number of layers is increased from one to five, and the stiffness difference between the stick and slip conditions are compared. The results are shown in Figure 13.

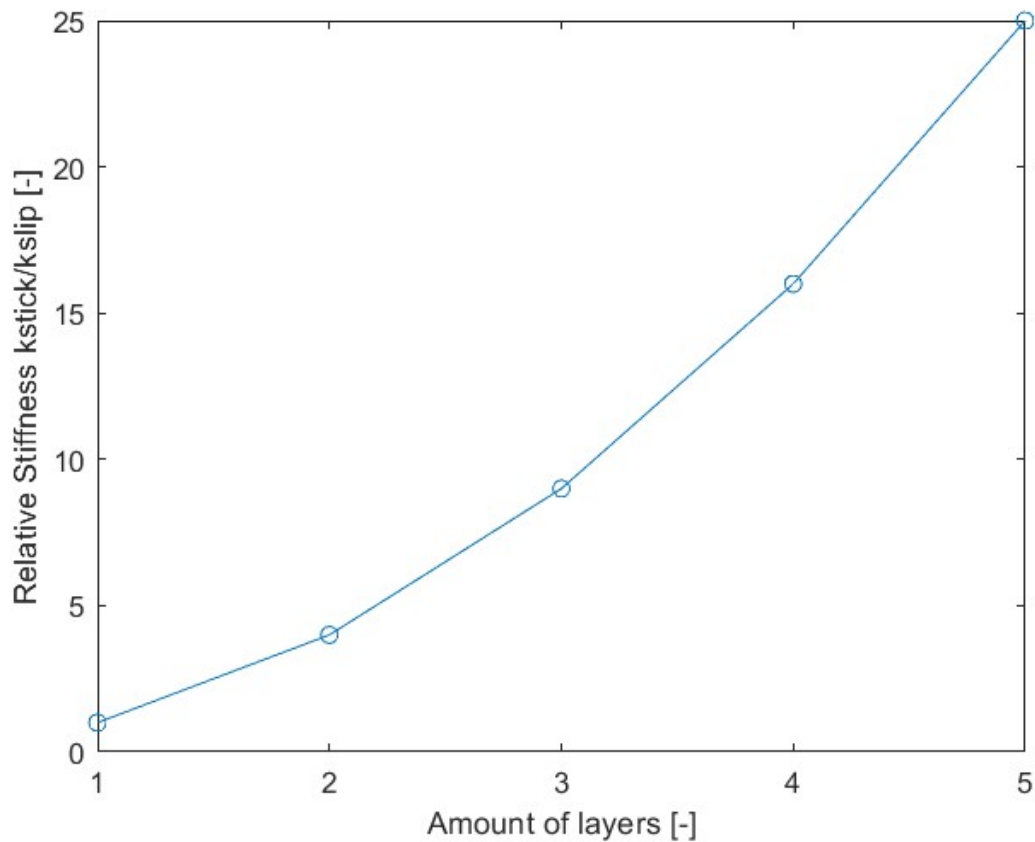


Figure 13: Number of layers plotted versus the relative rotational stiffness.

The promising effectiveness of this method is again reflected in the graph, which shows a stiffness increase of up to 2500% for a design with five layers. Although the Stick-slip method promises the highest effectiveness of the methods so far, the calculations assume that whenever a voltage is applied the layers always stick together. This is not necessarily true to reality, as Stick-slip is a dynamic process (Bergamini, 2006). The applied voltage induces a normal stress at the interface between the layers, which in turn induces friction between the layers. The layers only stick together as long as the shear stress caused by this friction is larger than the shear stress induced by the bending deflection. Therefore, the effectiveness calculated in this section is only a theoretical maximum.

### 2.3 The Damping Model

In the literature survey the smart fluids looked to be some of the most promising materials yet, with research and simulations predicting very high effectiveness up to 100000% (Bonnecaze, 1992). The smart fluids are still most commonly used in large scale applications like structural damping (Zhu, 2012), but small-scale applications are becoming more frequent, for instance in small-scale dampers (Tse, 2004) and soft robotics (Majidi, 2010).

Smart fluids consist of two categories, fluids that increase its viscosity when subjected to a magnetic field, magnetorheological fluids (MR) (De Vicente, 2011), and fluids that increase their viscosity when subjected to an electric field, electrorheological fluids (ER) (Winslow, 1949). These fluids consist of a carrier fluid combined with particles or fibers which forms chains when subjected to their respective

external fields (Phule, 1998). This change in consistency of the system influences its damping capacities, usually in a matter of milliseconds. However, using a change in damping coefficient to influence the movement of the wing in a FWMAV does have its downsides. The main problem with damping is that it is generally an irreversible transfer of mechanical energy into heat or growth of cracks or other defects (Zinoviev, 2018). Both of these effects are of course unwanted, especially in a FWMAV like the Atalanta project. Weight is the biggest constraint and energy storage is one of the biggest contributors to the weight of the vehicle. Therefore, implementing a system that purposely dissipates energy to allow control might seem contradictory. However perhaps the effectiveness of this system can make the trade-off worthwhile, which will be analyzed in this section.

As in the previous section about stiffness modelling the hinge will be modeled as a steel beam with dimensions length  $L$ , width  $d$  and thickness  $t$ . However, while for stiffness the formulations for a beam are fairly straightforward, the damping proves more difficult. Axial damping is still relatively simple, although it does already require an experimentally determined coefficient (JPE Innovations, 2022), the damping in bending motion requires a dive into beam theory (Banks, 1991). Banks defines a formulation for the bending moment in a cantilever beam as follows:

$$M_D = c_d I(x) \frac{\partial^3 u(x,t)}{\partial x^2 \partial t}. \quad (2-22)$$

Here  $c_d$  is an experimentally determined strain-damping coefficient,  $I(x)$  is the second area moment throughout the beam, and  $u(x, t)$  is the displacement function of the beam. For a cantilever beam fixed on one end and free on the other the displacement function consists of a combination of a spatial function  $\phi(x)$  and a temporal function  $a(t)$ , shown in Equations 2-23 to 2-26 (Megahed, 2003).

$$u(x, t) = \phi(x) * a(t). \quad (2-23)$$

With:

$$\phi(x) = \cos(\beta x) - \cosh(\beta x) + \frac{-\cos(\beta L) - \cosh(\beta L)}{\sin(\beta L) + \sinh(\beta L)} (\sin(\beta x) - \sinh(\beta x)). \quad (2-24)$$

Where  $\beta$  is defined as:

$$\beta = \sqrt[4]{\frac{\rho d t}{EI}}. \quad (2-25)$$

$$a(t) = A \cos(\beta^2 t) + B \sin(\beta^2 t). \quad (2-26)$$

Next using boundary conditions, it can be determined that  $B$  equals to zero and  $A$  is equal to Equation 2-27.

$$A = \frac{2}{L} \int_0^L \frac{P x^3}{6EI} \left[ \cos(\beta x) - \cosh(\beta x) + \frac{-\cos(\beta L) - \cosh(\beta L)}{\sin(\beta L) + \sinh(\beta L)} (\sin(\beta x) - \sinh(\beta x)) \right] dx. \quad (2-27)$$

Here  $P$  is a force acting on the free end of the beam, which can be taken from the aerodynamic model from Section 2.1. The resulting damping moment in the end of the beam is plotted in Figure 14 over the span of one wing beat.

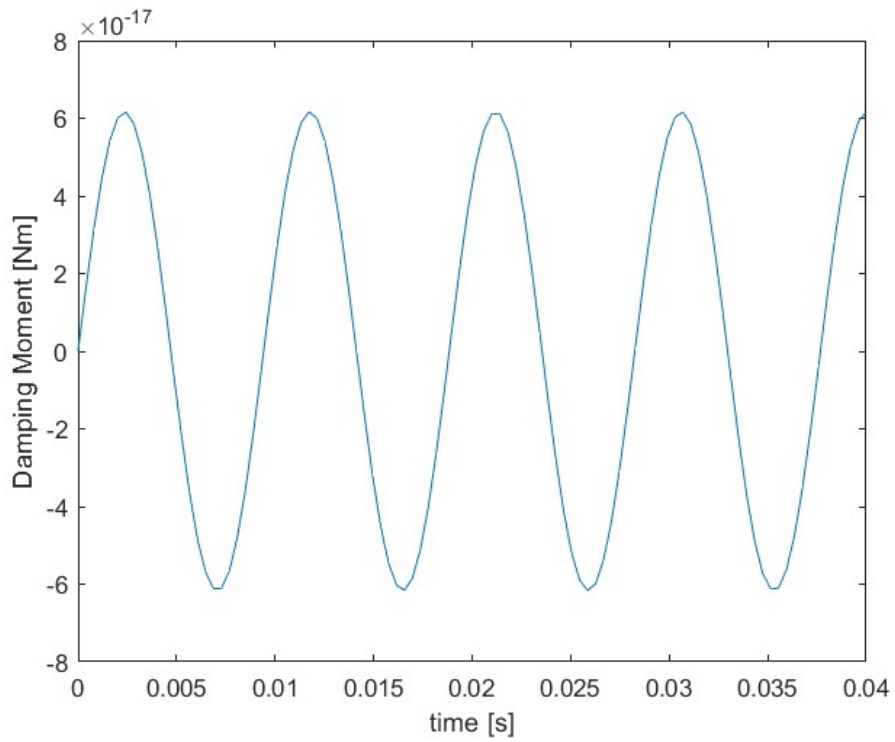


Figure 14: Time versus damping moment.

A Similar plot is made for the torque caused by the pitching motion of the wing, evaluated at the wing root, plotted over the span of one wing beat.

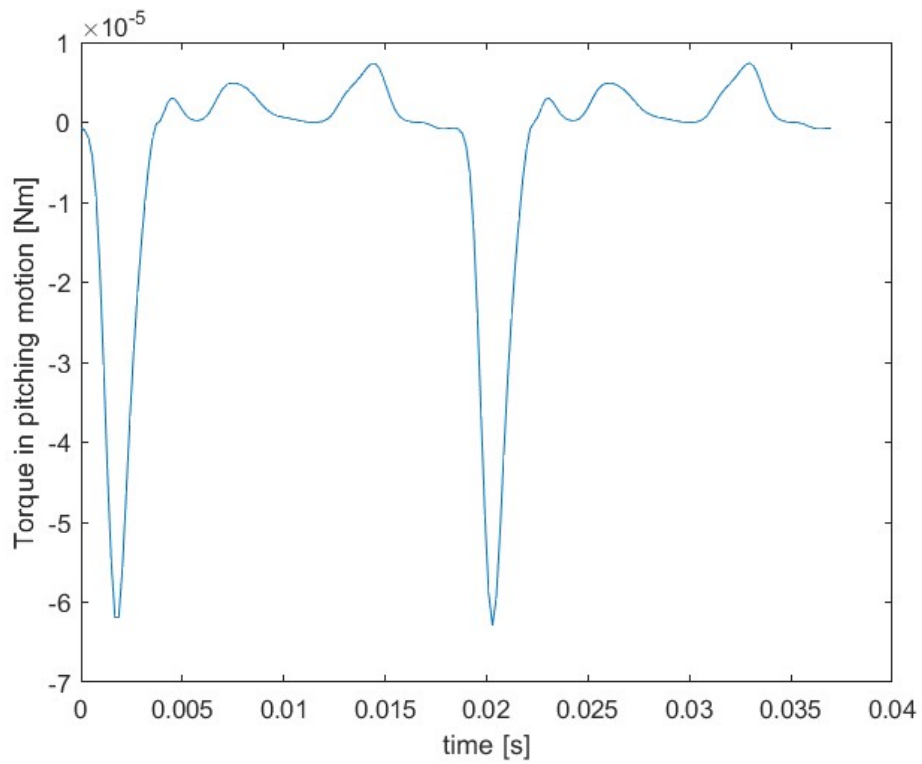


Figure 15: Plot of the pitching torque versus time.

The important thing to notice here is the difference in order of magnitude. The torque on the wing caused by the pitching moment is of order  $1 \cdot 10^{-5} Nm$ , whereas the order of the damping moment is  $1 \cdot 10^{-17} Nm$ . This means that even if the smart fluids are able to increase the damping of the hinge by 100000% as speculated to be possible (Bonnecaze, 1992), the damping moment will still be very insignificant relative to the wing torque, and the increase in damping will have no noticeable effect. The damping coefficient is taken the same as in (Banks, 1991), which is experimentally determined for a composite beam. The ASTM E756 standard (ASTM, 2017) mentions that the loss factor for steel beams is significantly lower than its composite counterparts, and even mentions that in calculations the loss factor can be taken as zero since the structural damping of steel beams is so low it is insignificant.

This large order of difference between the damping and torque moment is somewhat intuitive. According to Banks, for a cantilever beam the relative effect of the strain damping compared to the aerodynamic damping increases as the eigenmode that is excited increases. Since the hinge can be seen as a small beam with a large mass at the end, representing the wing, we can easily estimate the eigenfrequencies. At a flapping frequency of 27 Hz and a first eigenfrequency of about 11 kHz the beam is excited nowhere near its first mode, meaning that the aerodynamic damping is the dominant form of damping. However, when we now consider the aerodynamic damping of a hinge with a surface area of  $6.34 \cdot 10^{-5} m^2$  compared to the aerodynamic damping of a wing with surface area  $1 \cdot 10^{-3} m^2$  it is clear that the hinge damping is not going to play a significant role.

## 2.4 Conclusions

With all the results calculated it is time to look at the different methods and see which are the most viable. As discussed in Section 2.1 while the stiffness only needed a relatively small 5.15 % increase to reach the 0.5% lift threshold, the damping needed to increase about fifteenfold to achieve the same threshold. Table 3 shows the maximum amount of total stiffness change the different materials and methods could cause.

Table 3: Effectiveness of stiffness methods and materials.

Material	Maximum stiffness change
Piezoelectric materials	250%
Cross-section expansion	160%
Stick-slip method	2500%

Using this data and the data from Figure 6 it seems all three of these methods are viable for achieving control in the Atalanta project, and they will all be modelled in Chapter 3.

For the damping materials, Figure 7 in Section 2.1 estimated that a 1500% increase in damping should be enough to reach the 0.5% lift threshold. However, it was already speculated in Section 2.1 that the true increase should be higher because the graph takes into account the damping for the entire wing and not just the hinge. Section 2.3 showed that even for a composite beam that was able to increase its damping by 10000% the damping moment in the hinge would still be insufficient to affect the generated lift. Therefore, it is decided that the smart materials will no longer be considered in this research. Perhaps with a specialized design of the hinge that maximizes damping the effectiveness of these materials could be increased enough to have a significant effect on the wing dynamics, as will be mentioned in the discussion.

## 3. Numerical Model

---

In this chapter the remaining three methods and materials will be tested through numerical modelling in COMSOL Multiphysics. Leaving the calculations to the software allows the designs to be more complicated. The effectiveness of the designs can then be compared to each other to try and find an optimal design for the hinge. This chapter will start off with two major constraints on the hinge, and more constraints will be added later in the report as the designs get more worked out. The two major constraints are the length  $L$ , width  $d$  and thickness  $t$  mentioned in the previous chapter, and a voltage constraint of 500 V.

Section 3.1 will discuss designs integrating the piezoelectric material as the main method of stiffness variation. Section 3.2 will do the same for the cross-section expansion method. Section 3.3 will discuss the stick-slip method and the problems with modelling it numerically. Section 3.4 takes the two most successful designs and discusses a number of design variations. These variations work to find two semi-optimized designs. Finally, Section 3.5 will compare these designs and choose one of them to develop into a final design in Chapter 4.

### 3.1 Piezoelectric Material Designs

In Chapter 2 the piezoelectric materials showed themselves to be in the middle of the pack in terms of effectiveness, with the material with the highest change in stiffness being the material with the highest electromechanical coupling factor  $k_{31}$ , as detailed in Equation 2-10 (Ramaratnam, 2004). From the values detailed in Table 2 Lead Zirconate Titanate (Nazeer, 2009) had by far the highest change in stiffness, so this is the material that will be used for the initial designs. The other main structural components will be modelled as structural steel due to its easy availability and its electrical properties allowing it to act as an electrode as well. The hinge will be modelled as a cantilever beam fixed on one end and with a downward force acting on the other end. The effectiveness can be measured by comparing the deformations at the end of the beam for different applied voltages.

Section 2.1 mentioned that for the desired 0.5% change in lift a 5.15% change in stiffness is required. To more easily compare different designs this 5.15% change in stiffness can be related to a change in deformation for a cantilever beam using Equation 3-1 from the Euler-Bernoulli beam theory (Bauchau, 2009).

$$k = \frac{P}{w}. \quad (3-1)$$

Here  $k$  is the bending stiffness,  $P$  is the applied load at the end of the beam and  $w$  is the deflection at the end of the beam. This equation shows that a 5.15% change in stiffness corresponds with a 5.15% decrease in deflection.

Two initial designs will be tested in this first section, a simple beam design with piezoelectric strips placed at the root based on the research of (Liao, 2012), and a design featuring a core of piezoelectric strips sandwiched between two structural steel layers inspired by (Eichhorn, 2011). The two designs are highlighted in Figure 16 and Figure 17. In both these figures the fixed end is at the left side and the load is applied on the right side. The gray material is steel and the yellow material is Lead Zirconate Titanate, also referred to as PZT. The stripes in Figure 17 for the first few piezoelectric strips show that the strips continue throughout the beam. Space is left around the piezoelectric strips to leave room for methods to apply a voltage but in these two designs the voltage is simply placed at the boundaries of the piezoelectric strips, since the goal for now is to first compare the working principles.

For both the designs two different electrical boundary conditions are attempted. The first design will be tested with an electric potential difference between the top and bottom of each strip, where in the first scenario the strips are actuating in the same direction and in the second scenario in opposite direction. The first scenario allows the two strips to combine their effectiveness (Newton, 1998), whereas the second scenario will induce a stress which will increase the stiffness of the beam (Peters, 2016).

The second design is tested with a potential difference between the top and bottom, and between the left and right sides of the strips.

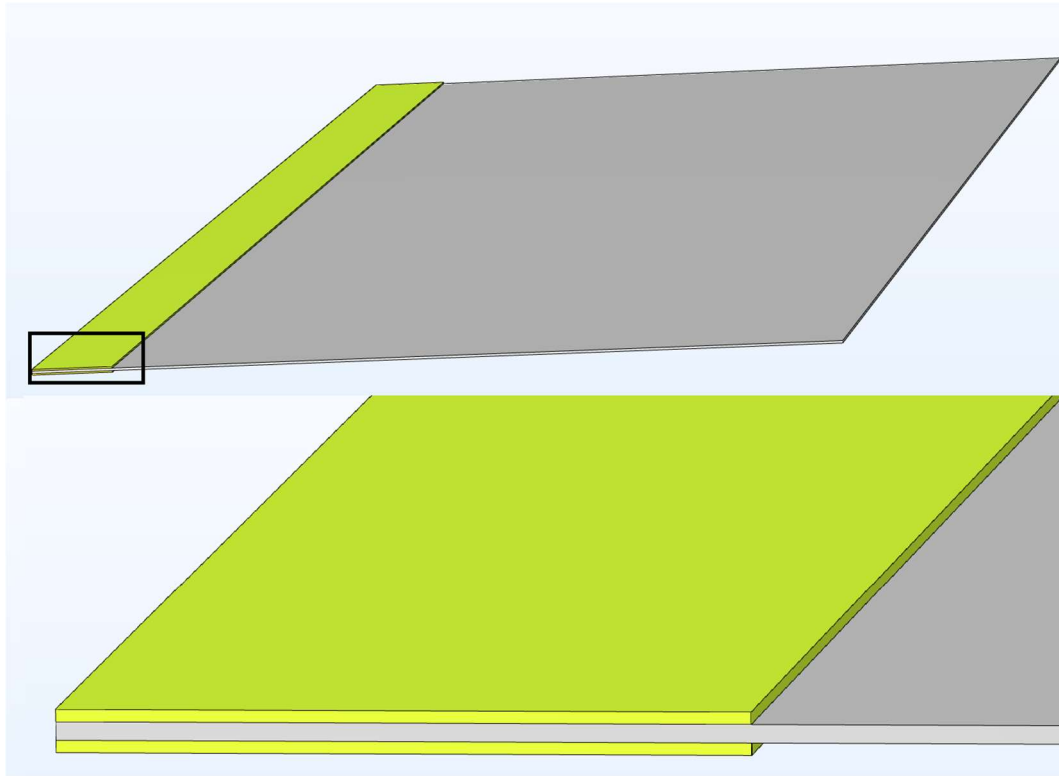


Figure 16: Design 1 featuring piezoelectric strips at the root of the beam.

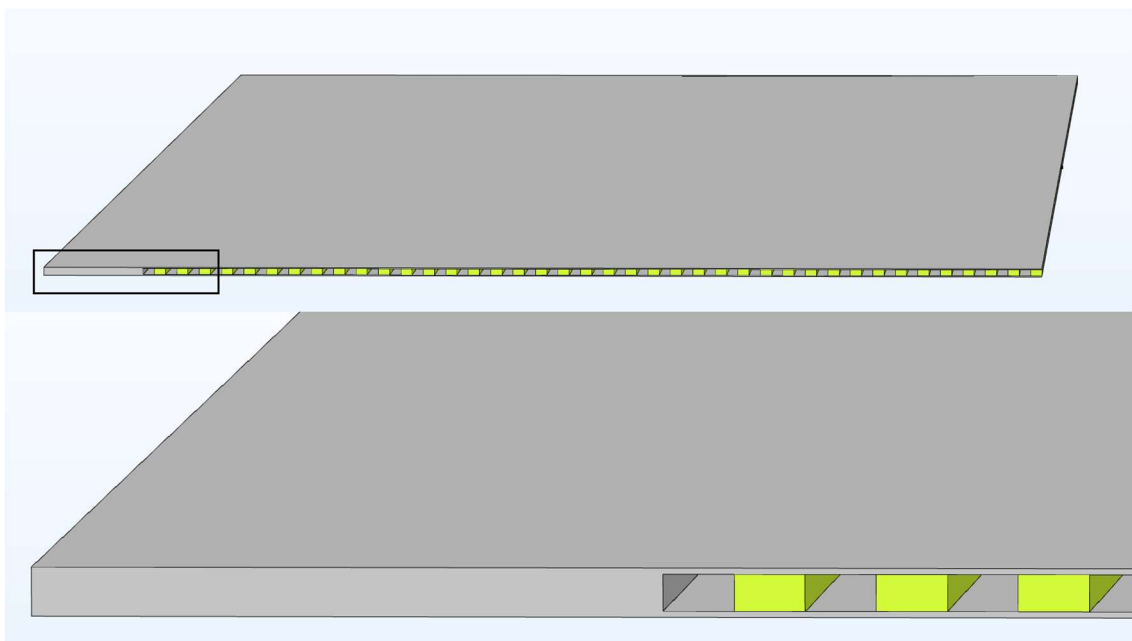


Figure 17: Design 2 featuring piezoelectric strips sandwiched between two steel plates.

Figure 18 and 19 show the relative displacement of Design 1 for the applied voltages in the two detailed scenarios.

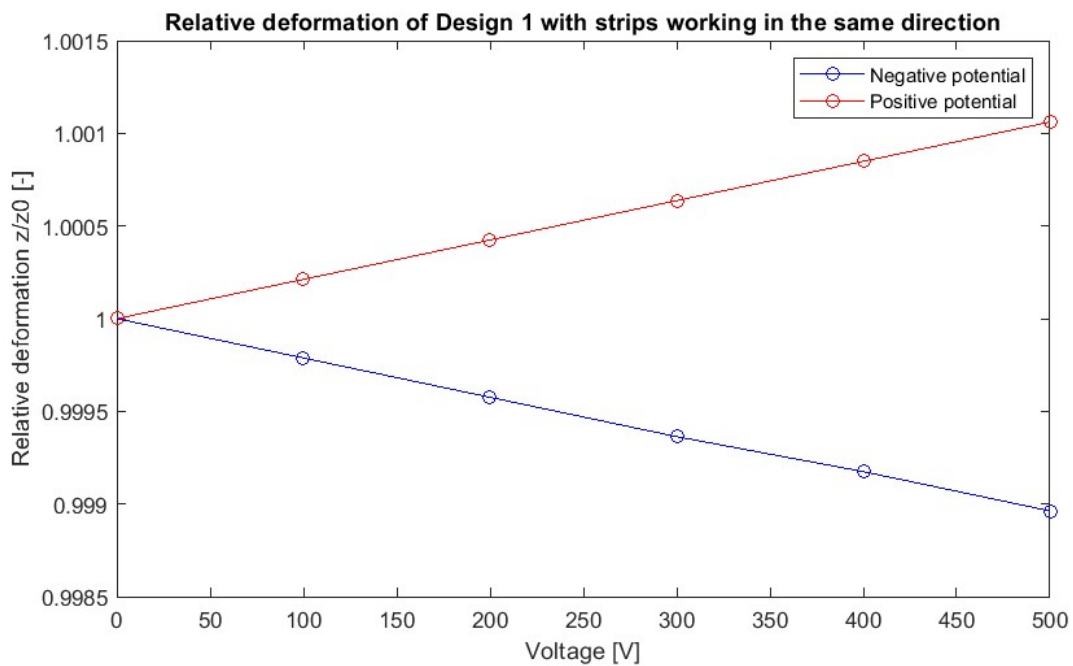


Figure 18: Voltage plotted versus relative deformation for Design 1 Scenario 1.

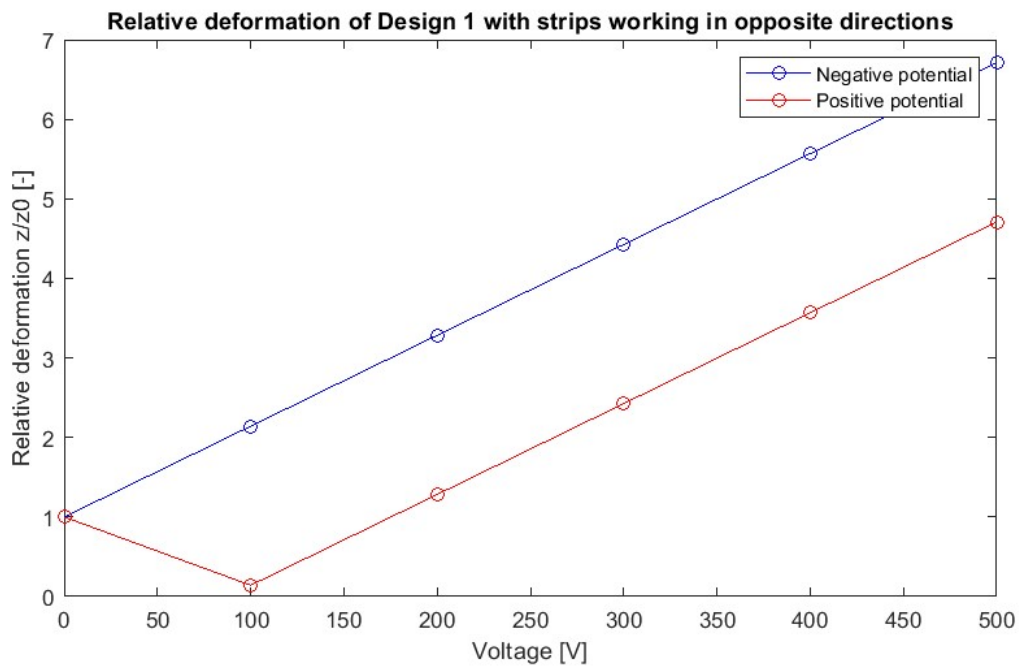


Figure 19: Voltage plotted versus relative deformation for Design 1 Scenario 2.

The most important thing to take away from these figures is the huge difference in effectiveness between the two scenarios. The first scenario is barely able to make a change to the deformation regardless of the potential direction, whereas the second scenario is able to completely undo the deformation caused by the boundary load and even greatly deform the beam in opposite direction for higher voltages. The

reason the line for the positive potential goes down before going up again is due to first having to overcome the initial deformation caused by the force working on the free end of the hinge. In the case of the negative potential the deformations work in the same direction as this initial deformation and therefore do not need to overcome it. It is clear that Scenario 2 is the most promising option for Design 1.

Figure 20 and 21 show the relative displacement of Design 2 for the applied voltages in the two scenarios.

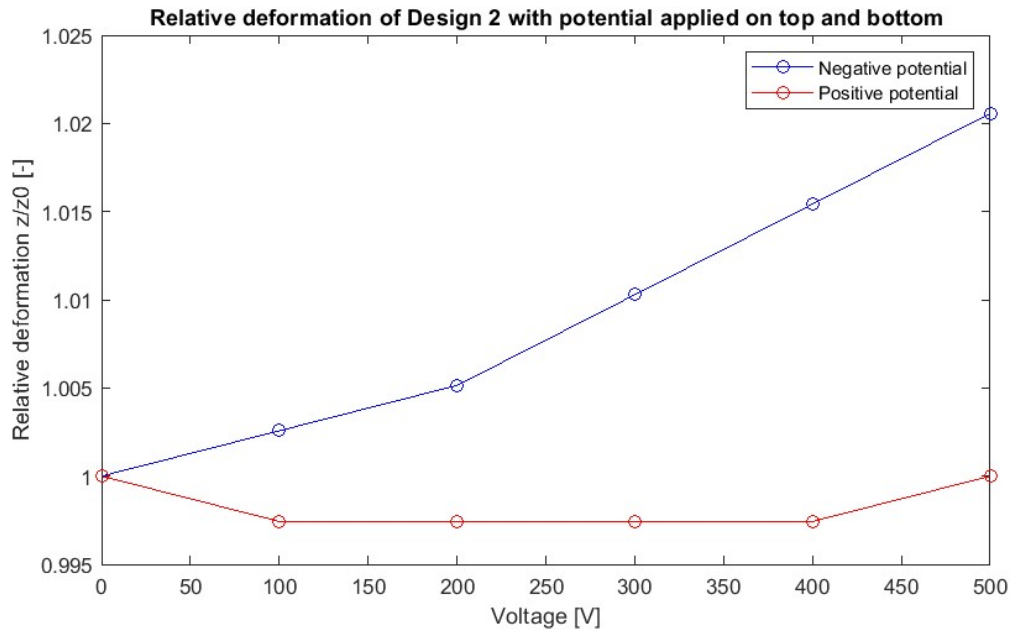


Figure 20: Voltage plotted versus relative deformation for Design 2 Scenario 1.

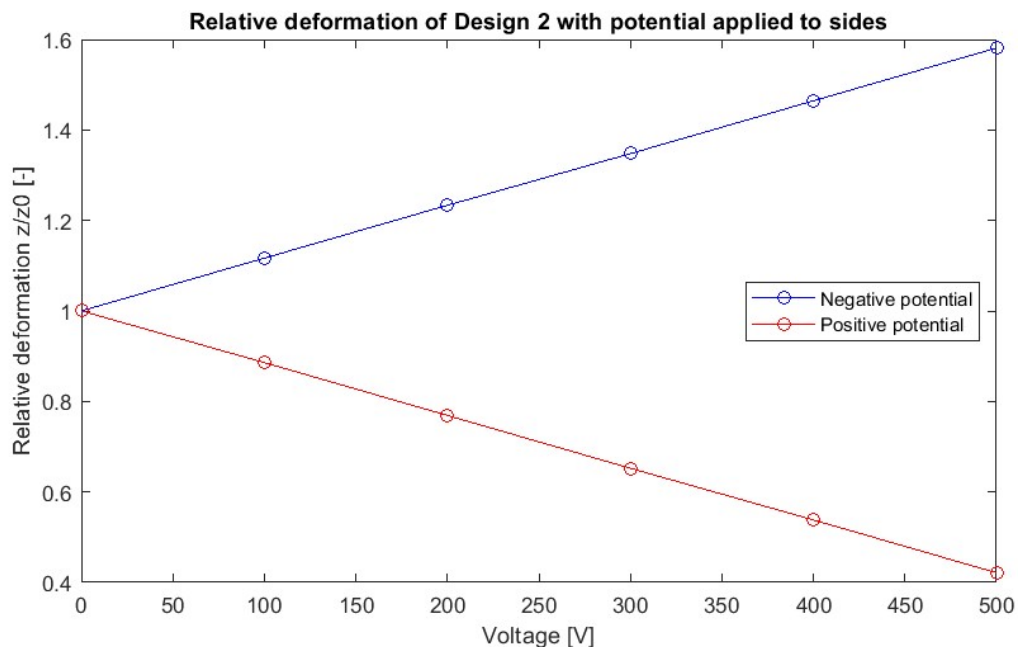


Figure 21: Voltage plotted versus relative deformation for Design 2 Scenario 2.

Again, from these figures a clear difference in effectiveness can be seen. As with the previous design Scenario 2 shows a much higher effectiveness, and the first Scenario is still not able to reach the 5.15% threshold based on the lift threshold posed by (Lu, 2013). It is of course important to keep in mind that higher voltages would probably require more complicated or heavy equipment on the Atalanta design so

effectiveness above the 5.15% threshold is definitely still relevant if it reduces the potential required. In Figure 20 the positive potential line shows the same effect as the positive potential in Figure 19, where it first has to overcome the initial deformation caused by the force working on the free end of the hinge.

### 3.2 Cross-section Expansion Designs

The cross-section expansion method proved to be the least promising in Chapter 2 but was nonetheless still easily able to achieve the 5.15% threshold in stiffness. An ellipse shaped cross-section was chosen in the analytical model since it allowed for easy calculations regarding the deformed cross-section but numerical modelling allows us to create a design with a rectangular cross-section. This will make it easier to compare the results of different methods and makes the design easier to produce for the possibility of an experiment. For these designs too structural steel and PZT will be used, and the hinge is once again modelled as a cantilever beam fixed on one end with a boundary load acting on the other.

For the cross-section expansion, three designs are discussed and two are tested. The first design consists of a hollow rectangular cross-section which will be expanded using piezoelectric strips on the outside of the cross-section, inspired by (Walsh, 1992). The second design is a simpler solid beam which through piezoelectric actuation is bent, increasing its second moment of area, as researched by (Kawai, 2006). The final design involves a honeycomb structure sandwiched between two steel plates, which can expand uniformly when subjected to an electric potential, such as presented in (Wang, 2021). Figure 22a) through c) show these three concepts schematically. Here gray and yellow are steel and PZT respectively, and green is a honeycomb structure material.

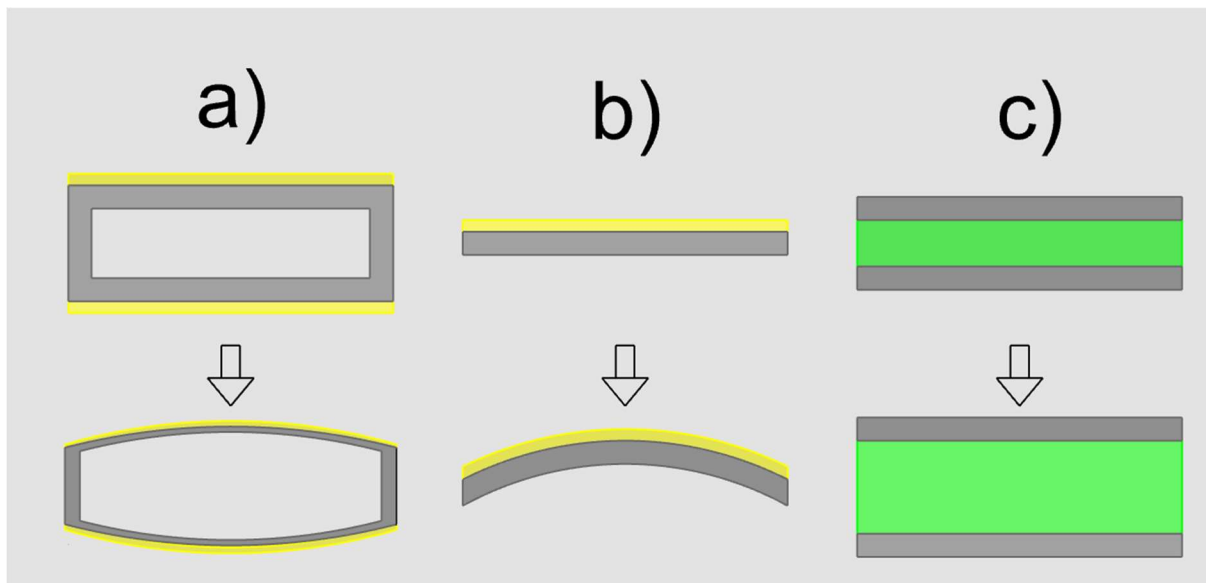


Figure 22: Schematic illustration of the three design principles. a) Deformation of hollow rectangular cross-section. b) Curvature deformation of solid rectangular cross-section. c) Uniform cross-section expansion using honeycomb structure material.

Figures 23 and 24 show the implementation of the first two designs in COMSOL, where once again gray material is steel and yellow material is PZT. In these figures similar as before the fixed edge is on the left and the boundary load is applied on the right. As in the previous section the electric potential is simply applied on the piezoelectric strips since the goal of the initial design is to test the working principle.

The third design is not modelled since the honeycomb structured materials are still in a very experimental stage and not easily implemented yet in COMSOL. There are ways to model uniformly expanding materials, as is discussed in the Discussion, however for this research the first two designs are deemed sufficient.

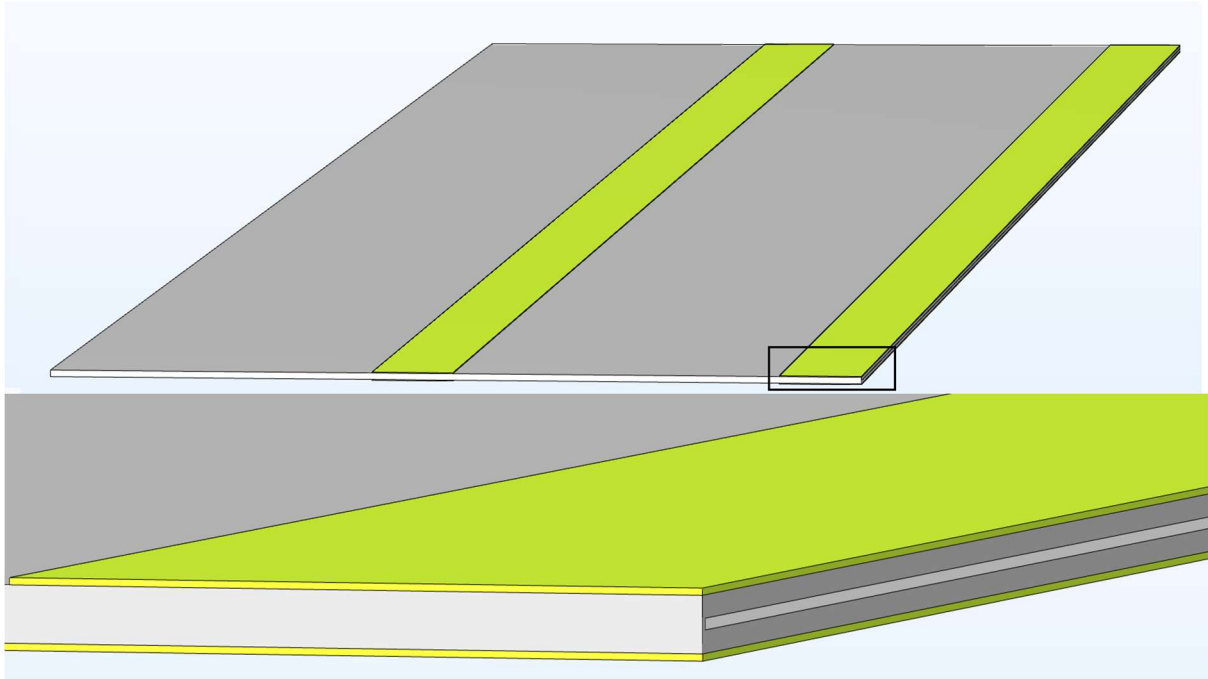


Figure 23: Design 1 featuring a hollow rectangular cross-section.

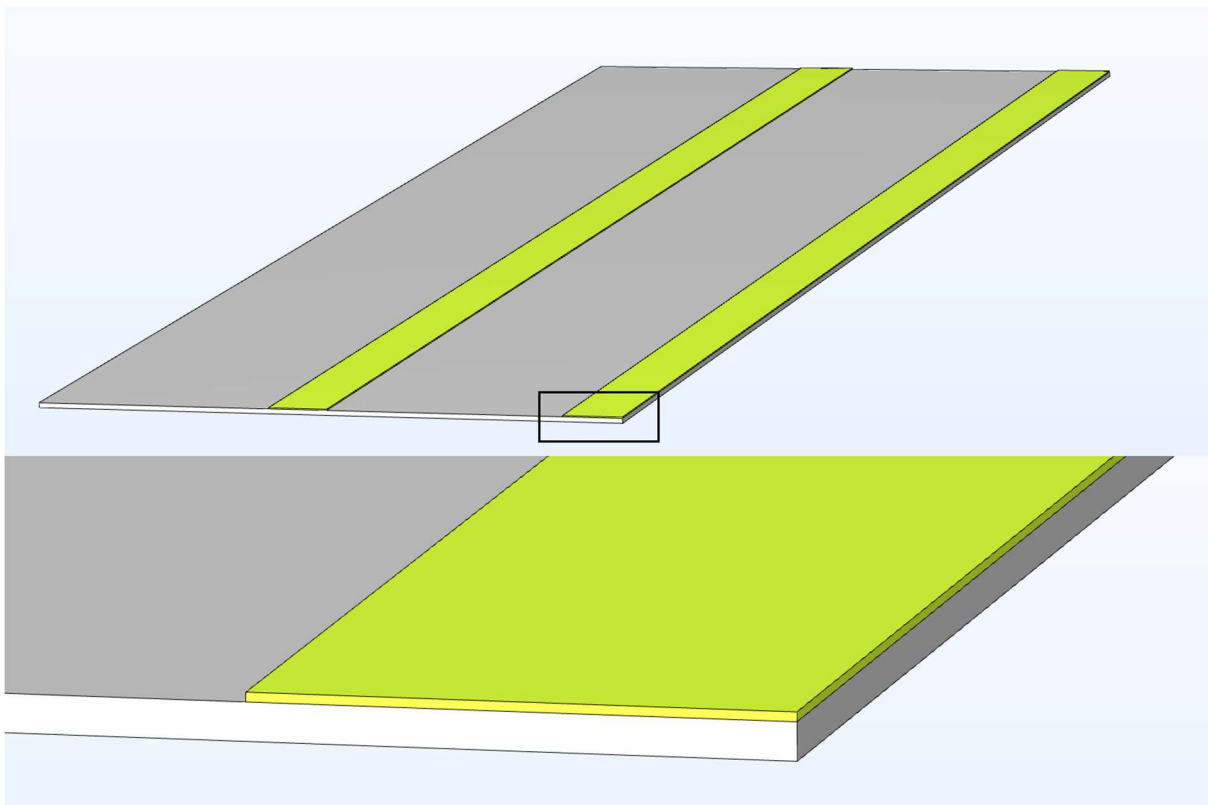


Figure 24: Design 2 featuring a solid rectangular cross-section.

Figure 25 and 26 show the relative displacement of the two designs plotted versus the voltage. In both design the displacement is taken in a node on the side and a node in the middle of the free end, since the deformation of the cross-section can either increase or decrease the deformation locally.

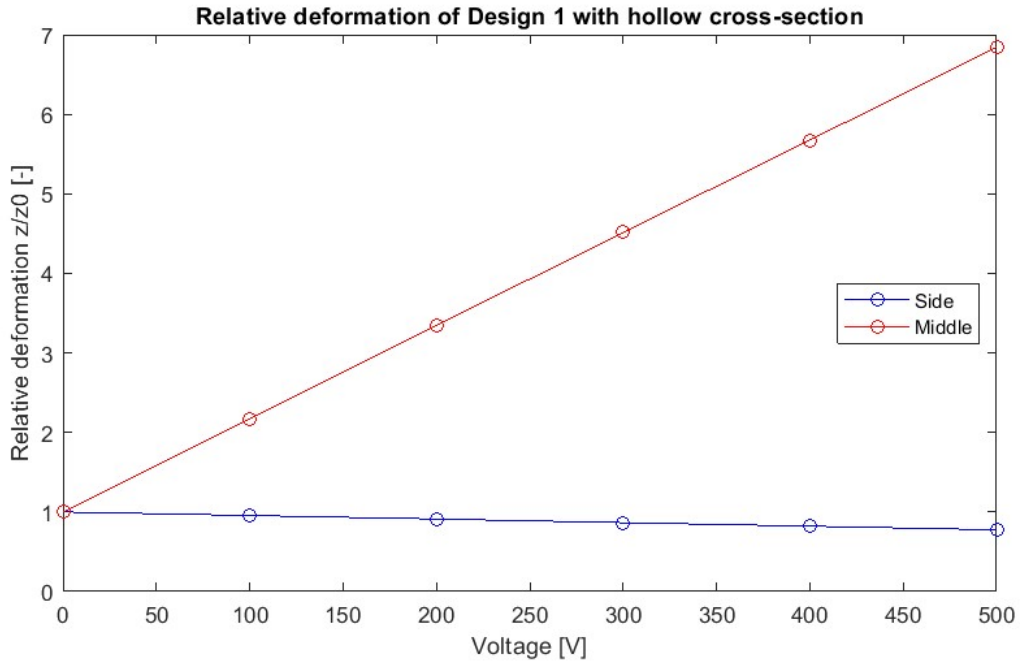


Figure 25: Voltage plotted versus relative deformation for Design 1.

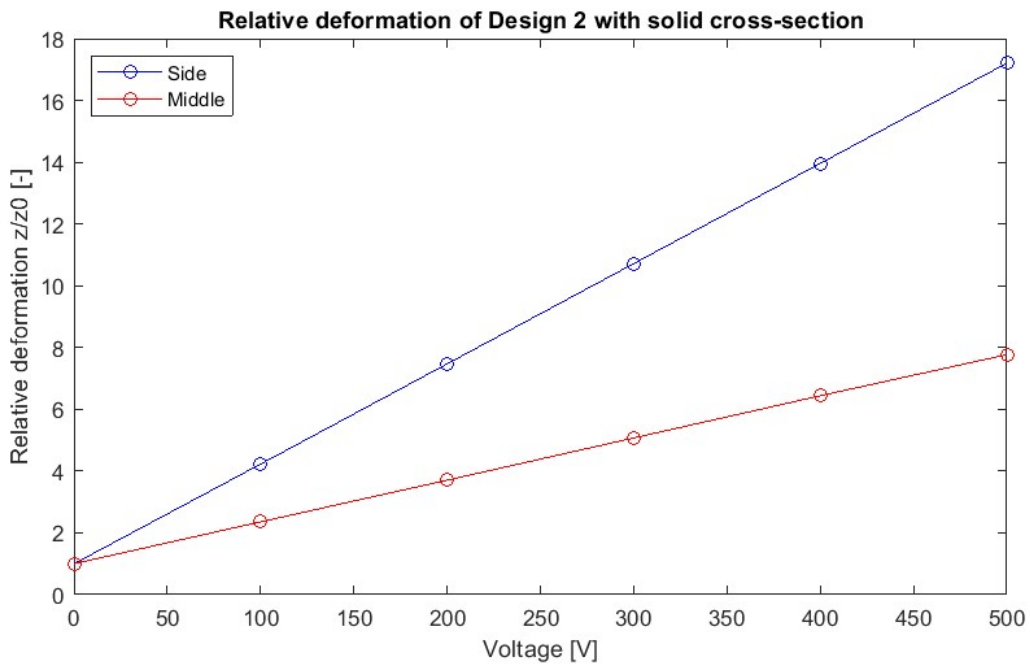


Figure 26: Voltage plotted versus relative deformation for Design 2.

The two cross-section expansion designs both show a high effectiveness, although this effectiveness generally seems based around further increasing the deformation rather than reducing it. This means that the methods effectiveness is due to the deformation of the piezoelectric materials, and not due to the increase in bending stiffness caused by the cross-section expansion. However, this makes sense under the boundary conditions as set for this model. The stiffness of a fixed-free beam has a higher effectiveness the closer to the fixed end it is, as this is where the bending moment is largest (Liao, 2012). But since the cross-section at the fixed end is also fixed, the cross-section deforms the most at the end where the effect of the added bending stiffness is the smallest. Since this is also the end of the beam

where the wing will be affixed, large deformations of the cross-section will also increase the complexity of this connection between the hinge and the wing.

### 3.3 Stick-slip Method Design

The final method from and the most promising one based on the results from Table 3 in Section 2.4 is the Stick-Slip method. However, some problems arose while trying to model the physics behind this specific method. The first attempt used a 2D model modelling the five layers and attempting to induce the normal stress required for the sticking mechanic by using the original intended dielectric effect to induce electrostatic loading (Kawai, 2006). However, after this model failed to converge the loading method was switched to simply using a distributed load on the outer two layers to induce sticking, hoping that the removal of a multi-physics interface might improve convergence. After this also failed to achieve convergence, it was theorized that COMSOL was not able to properly model the highly non-linear and highly dynamic nature of the many contact surfaces sticking and slipping, as was briefly mentioned in Subsection 2.2.3. A foray into literature did turn up a few instances where COMSOL is seemingly used to model Stick-slip behavior, such as in a micro-robot (Jalili, 2018), or for an earthquake (Zhang, 2021). However, upon further inspection this is on a much simpler scale with only one or two contact points.

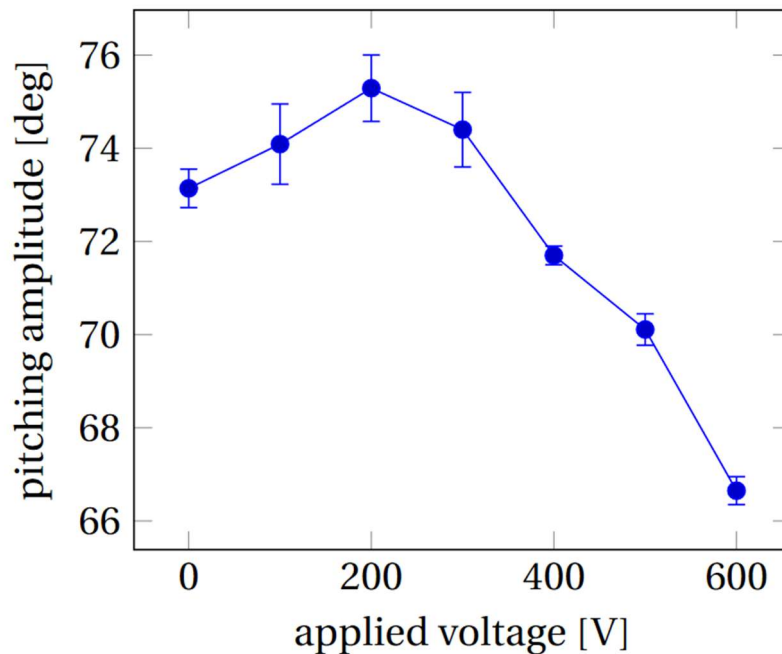


Figure 27: Pitching amplitude of the wing plotted versus the applied voltage, image from (Wang, 2017).

Thankfully, there are still results that can be used to compare this method with the other methods. An experiment has been carried out in (Wang, 2017) using a Stick-slip wing hinge for the Atalanta project, as shown in Figure 27. In this experiment Wang is able to achieve a change in pitching amplitude of 8.3% using a maximum voltage of 600 V. According to the model, this change would result in a 20% change in lift generation, which would be more than sufficient to achieve control in a FWMAV.

### 3.4 Design Variations

With all the results of the first round now available, it is time to select the most promising concepts and try to improve them. To achieve this, the two most promising and realistic designs are selected and a

number of variations are tested to see what works best. Figure 28 shows a comparison between all the designs mentioned in this chapter so far.

The first design that is picked is the first piezo design in the second scenario, shown in Figure 16. This design features two strips of piezoelectric material at the root of the beam which deform in opposite directions, inducing a stress in the beam which can increase its deformation up to 6.5 times in this admittedly simple conceptual model. The second design is the second piezo design in the first scenario. This design implements an array of piezoelectric strips between two steel plates, allowing a deformation increase of about 2.5%. Even though this design is not as effective as the designs in the cross-section expansion category, the piezoelectric strips fixed between two steel plates allow for an easy application of an electric potential, and the gaps between the strips allow for the possibility of for instance an adhesive to fix the strips to the plates. The design does not achieve the 5.15% stiffness increase that is required for the desired change in lift but the hope is that with some variations the effectiveness can be increased to a degree where it satisfies the design specifications. With these two designs, there is the combination of a highly effective design and an easier to implement design. The second cross-section expansion design also shows a lot of potential, but the deformation of the cross-section on the free end makes attaching a wing in a robust way very complex. Therefore, the potential of the method is acknowledged, but it is decided to move further with just the first two designs.

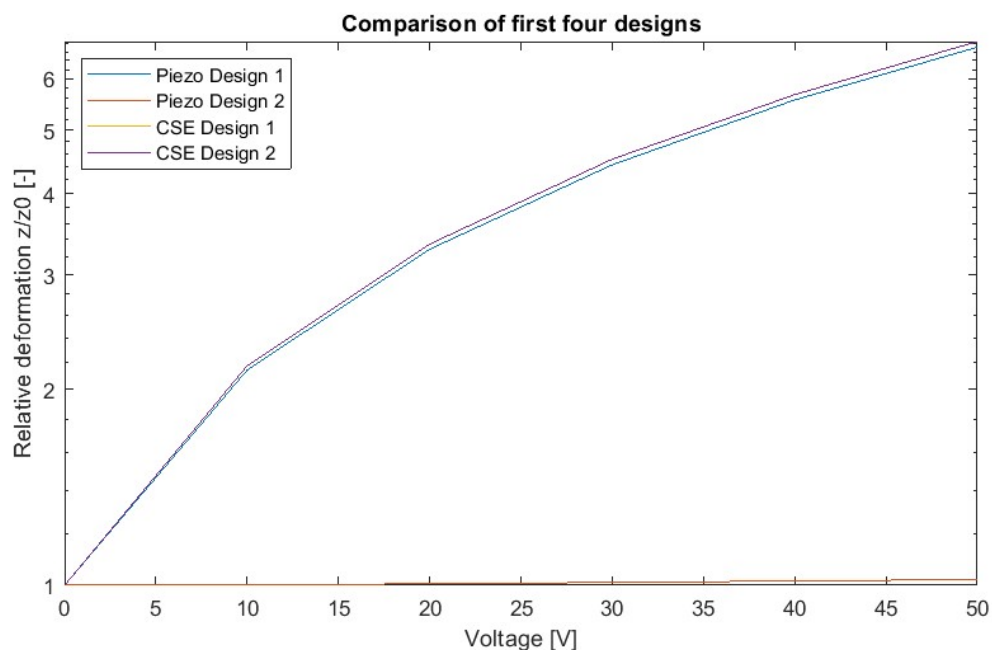


Figure 28: Comparison of first four designs.

Both designs will be modelled in a number of different variations in the next two subsections in an attempt to find a more optimized hinge. In this section for all designs the sign of the electric potential is chosen in such a way that it increases the deformation rather than reducing it. This makes it easier to compare different designs since some designs have deformations large enough that it fully nullifies the original deformation and displaces the hinge in the opposite direction.

### 3.4.1 Design Variations of Design 1

The first design to look at is Design 1. For the first variation a system is implemented to allow for the application of an electric field over the piezoelectric strips, and some adhesion film is added between the steel sheets to keep the design together. The design is shown in Figure 29. Here gray material is steel,

yellow material is PZT and the dark blue material is adhesion film. Once again, the left side is the fixed side and the right side has the boundary load. Figure 30 shows the deformation related to the applied voltage.

Figure 30 shows that this variation can reduce the deformation by about 90%, which is very promising. As discussed in Section 3.1, even if the effectiveness is already very high, it is useful to try and improve it since a lower voltage required will likely help reduce the weight the complete system takes up on the Atalanta design. So, for the next variation we attempt to increase the effectiveness and improve the ease of manufacturing by extending the piezoelectric strips over most of the hinge surface, and increasing the area of the adhesion film. Variation 2 is shown in Figure 31. It is important to note that in the top part of the image the top steel layer is hidden, showing the layout of the piezoelectric material and the adhesion film. Figure 32 shows the relative deformation for the applied voltage.

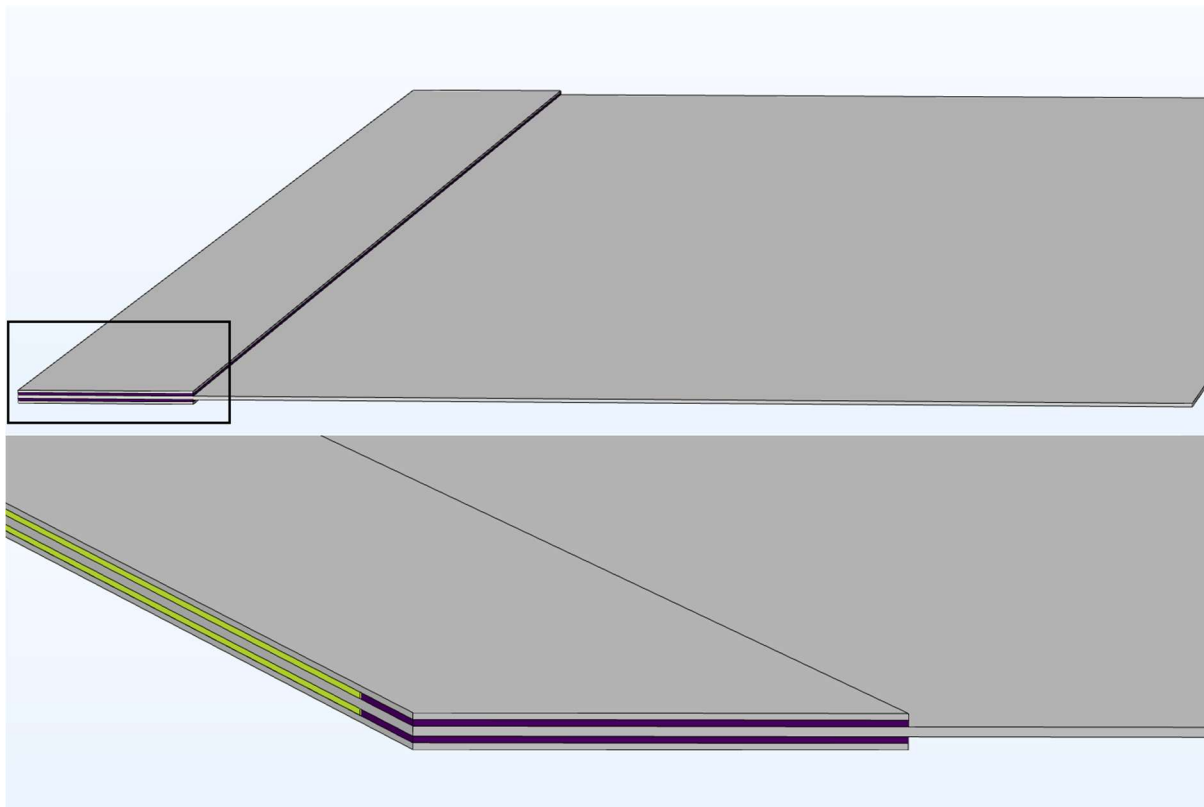


Figure 29: Design 1 Variation 1.

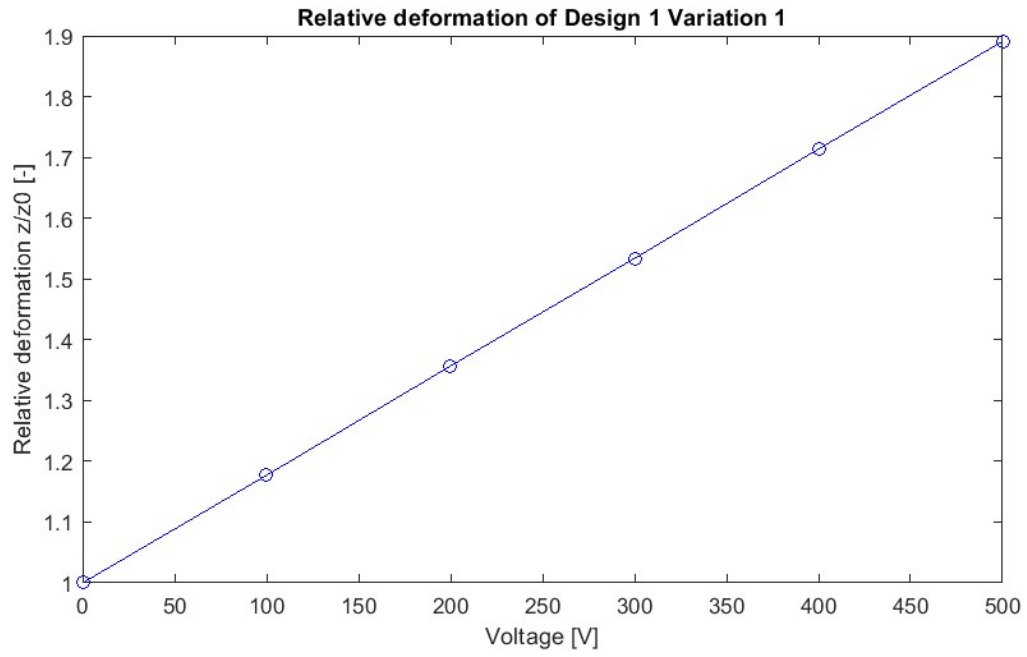


Figure 30: Voltage plotted versus relative deformation for Design 1 Variation 1.

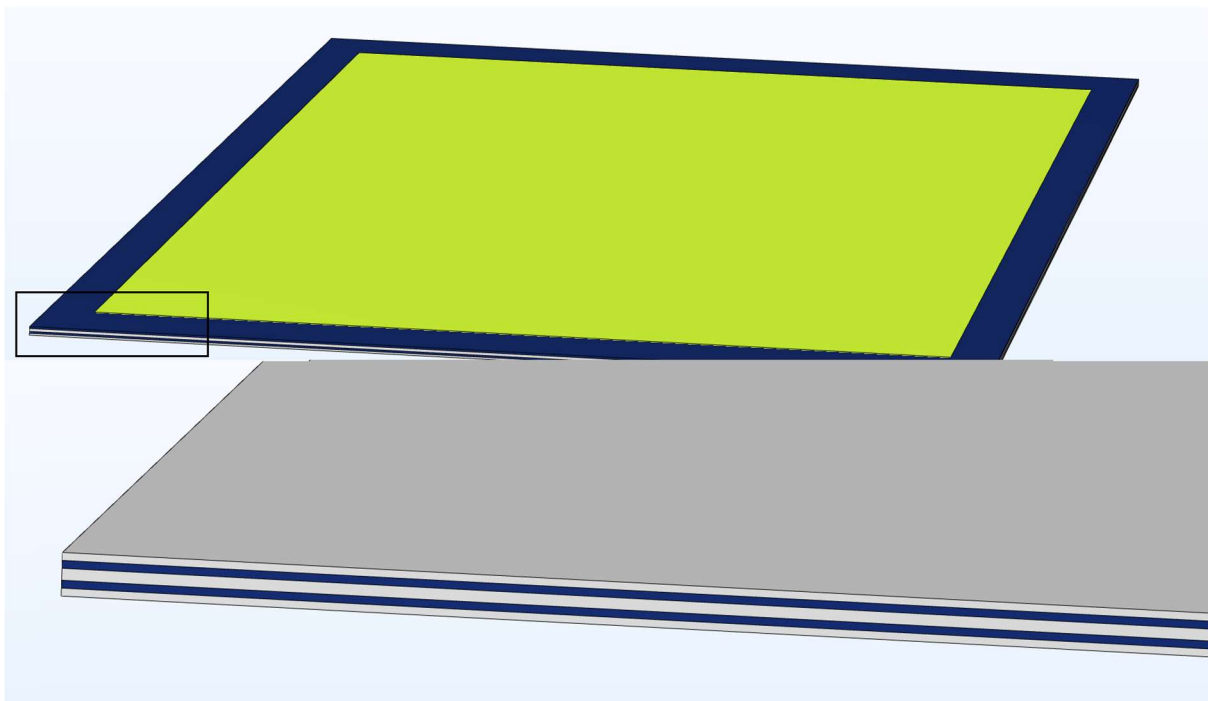


Figure 31: Design 1 Variation 2.

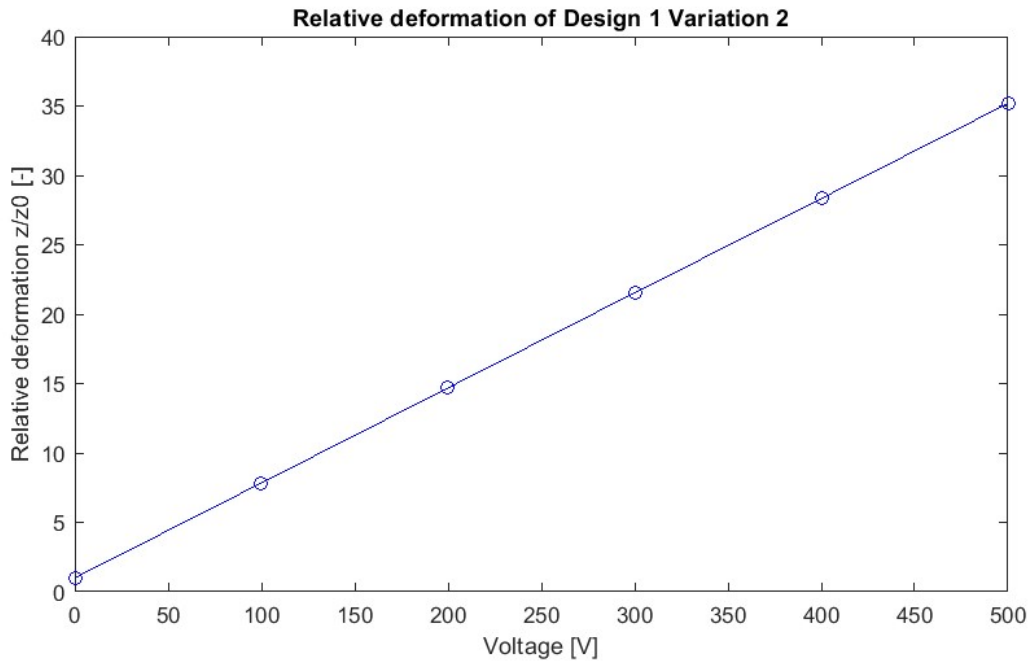


Figure 32: Voltage plotted versus relative deformation for Design 1 Variation 2.

This variation does indeed have an increased effectiveness, increasing the deformation by up to 35 times over the applied voltage range. Looking at the graph if this design were implemented in the Atalanta FWMAV a voltage of about 10 V would probably be more than enough to allow for control of the vehicle, which would greatly reduce the weight of the system.

### 3.4.2 Design Variations of Design 2

The second design we look at is the second piezo design. This design is chosen due to its practical design, allowing the possibility of applying an electric field over the piezoelectric strips using the steel top and bottom plates as well as leaving room for adhesion between the piezoelectric strips. However, the effectiveness is a lot lower than some other discussed designs and insufficient from a design perspective, so in this subsection it is attempted to improve the design.

The first variation increases the size of the piezoelectric strips to increase the effectiveness, shown in Figure 33 The relative deformation plotted versus the applied voltage is shown in Figure 34.

This variation proves to not be very effective, struggling to reach a 0.3% difference in deformation. To test a similar idea but this time with added adhesive layers Variation 2 is created, shown in Figure 35. Its relative deformation is shown in Figure 36. This design shows a very slight increase in effectiveness which corresponds to the very slight increase in volume of the piezoelectric strip. From the still relatively weak results it is clear that this is not the right design direction.

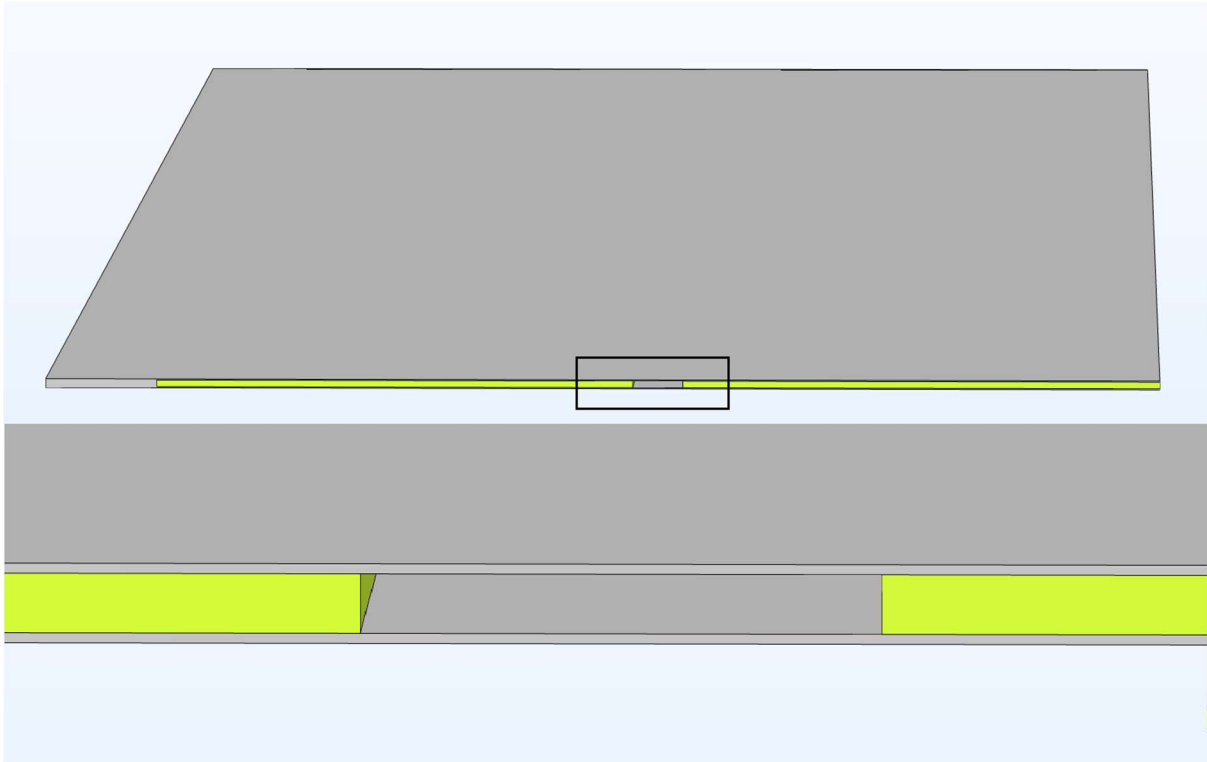


Figure 33: Design 2 Variation 1.

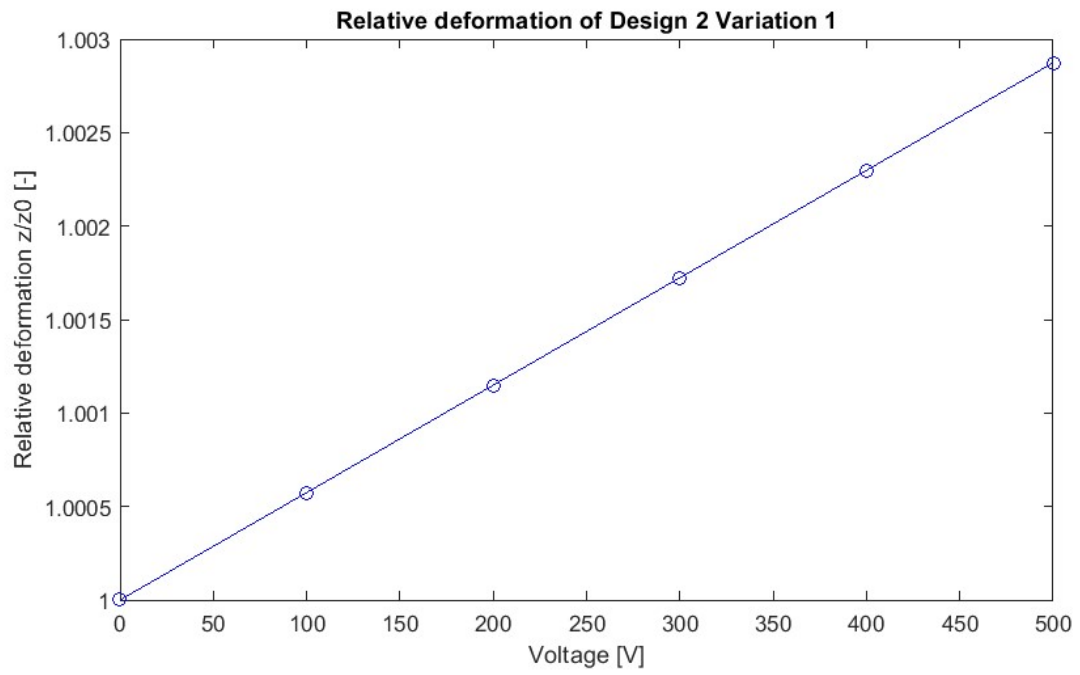


Figure 34: Voltage plotted versus relative deformation for Design 2 Variation 1.

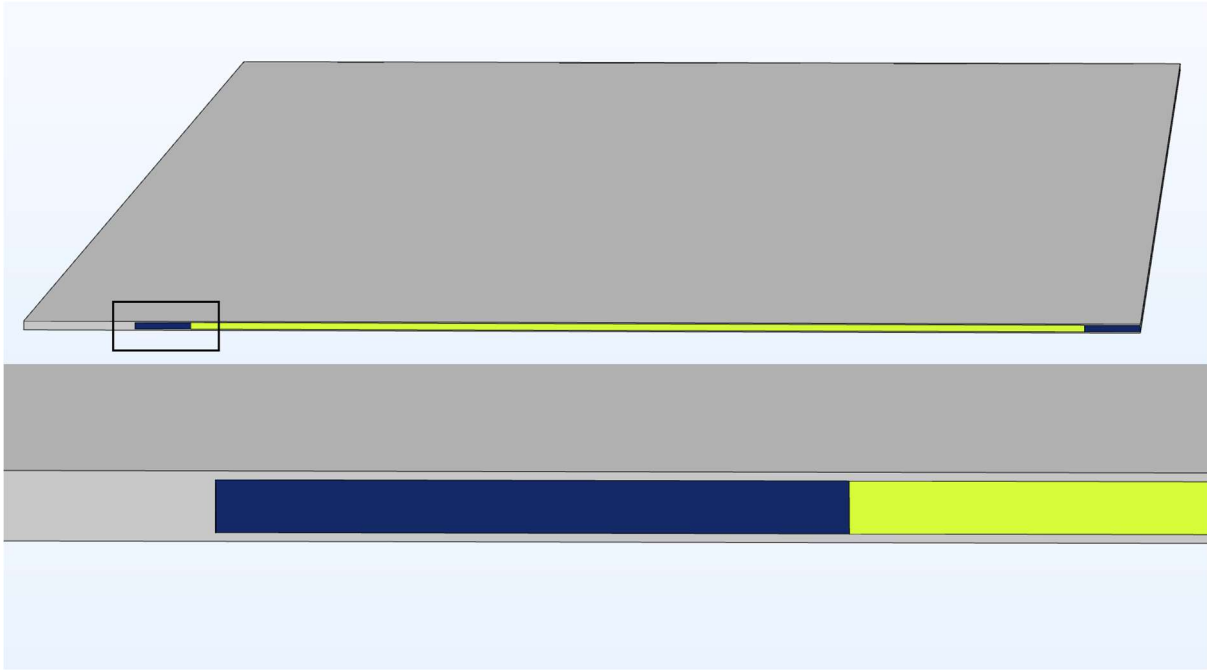


Figure 35: Design 2 Variation 2.

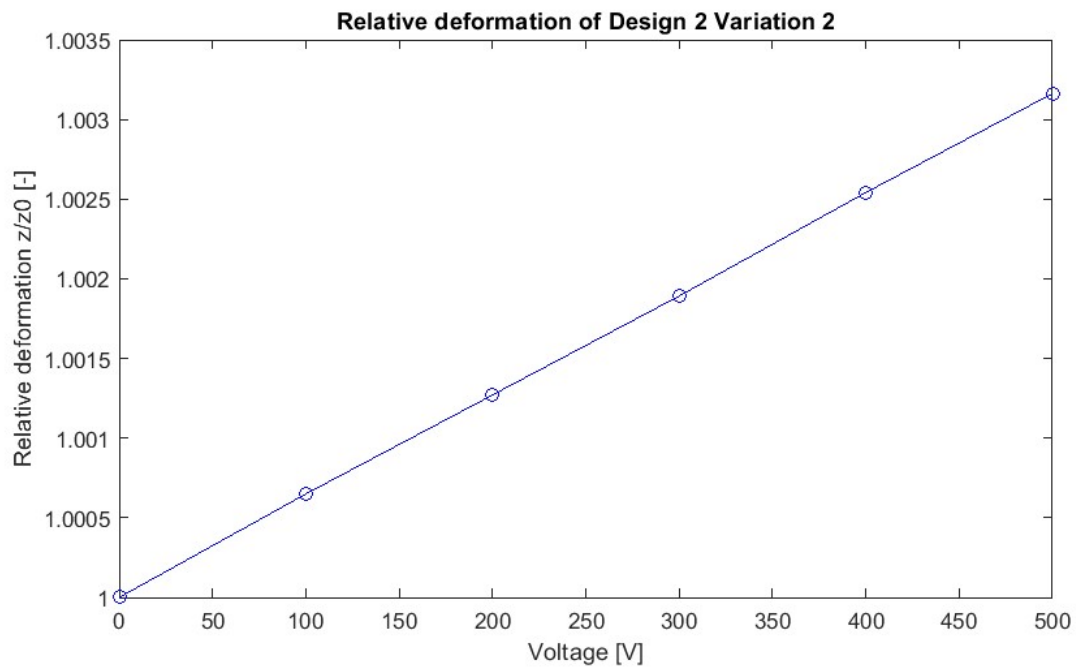


Figure 36: Voltage plotted versus relative deformation for Design 2 Variation 2.

For the next variation we decrease the size of the piezoelectric strips as in the original design, and we connect the metal sheets on the sides instead of on the fixed end. This is done to perhaps use the induced stress in the width direction to increase the stiffness. The design is shown in Figure 37 where the lines in the top image show the size and direction of the strips. Its relative deformation is shown in Figure 38. This design shows an even lower effectiveness, so perhaps to improve the results we need to try something else.

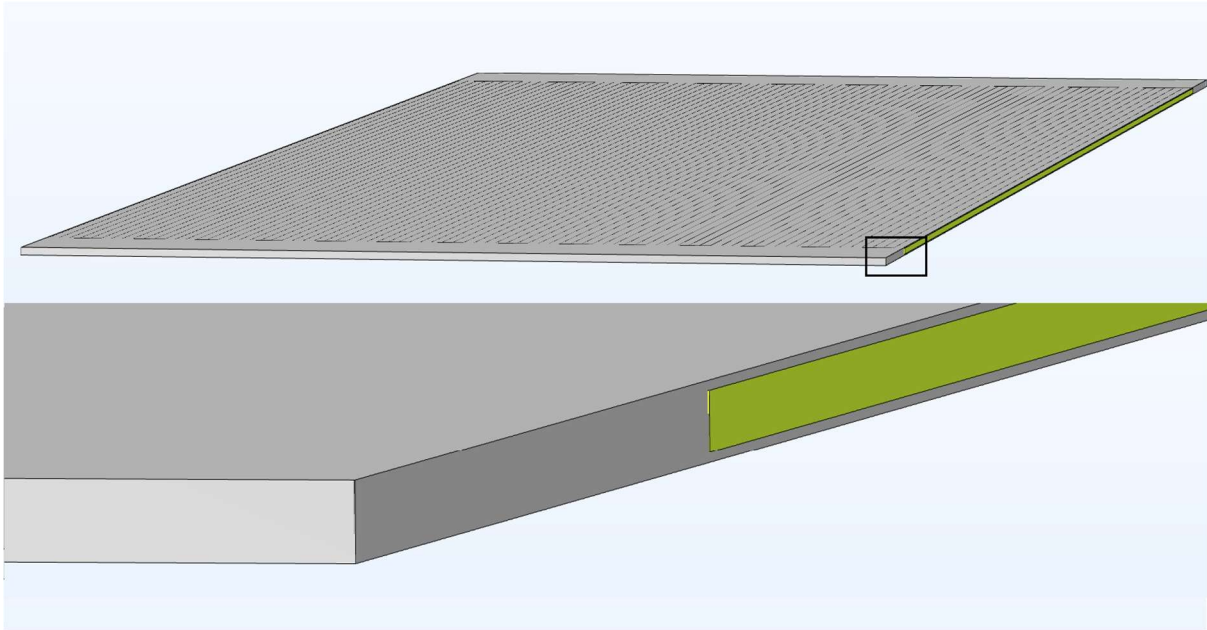


Figure 37: Design 2 Variation 3.

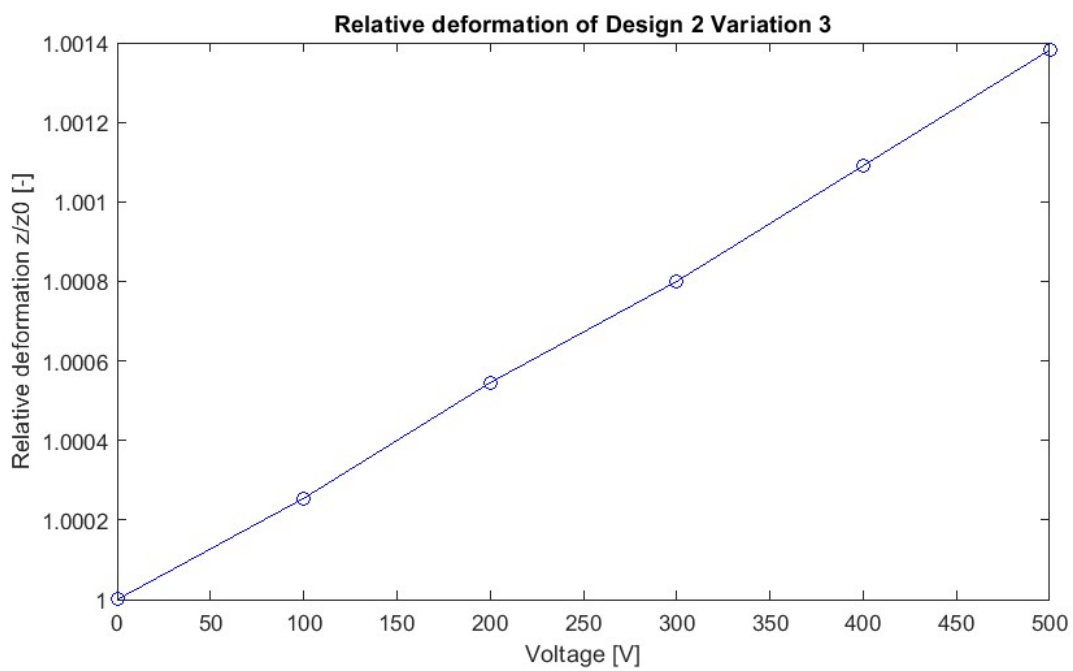


Figure 38: Voltage plotted versus relative deformation for Design 2 Variation 3.

The final variation, Variation 4, changes the orientation of the piezoelectric strips to the longitudinal direction, and adds a strip of adhesive between the piezoelectric layers. It is shown in Figure 39. In the bottom image the surrounding steel structure is hidden to show the orientation and structure of the piezoelectric and adhesive strips inside. The relative deformation graph is shown in Figure 40.

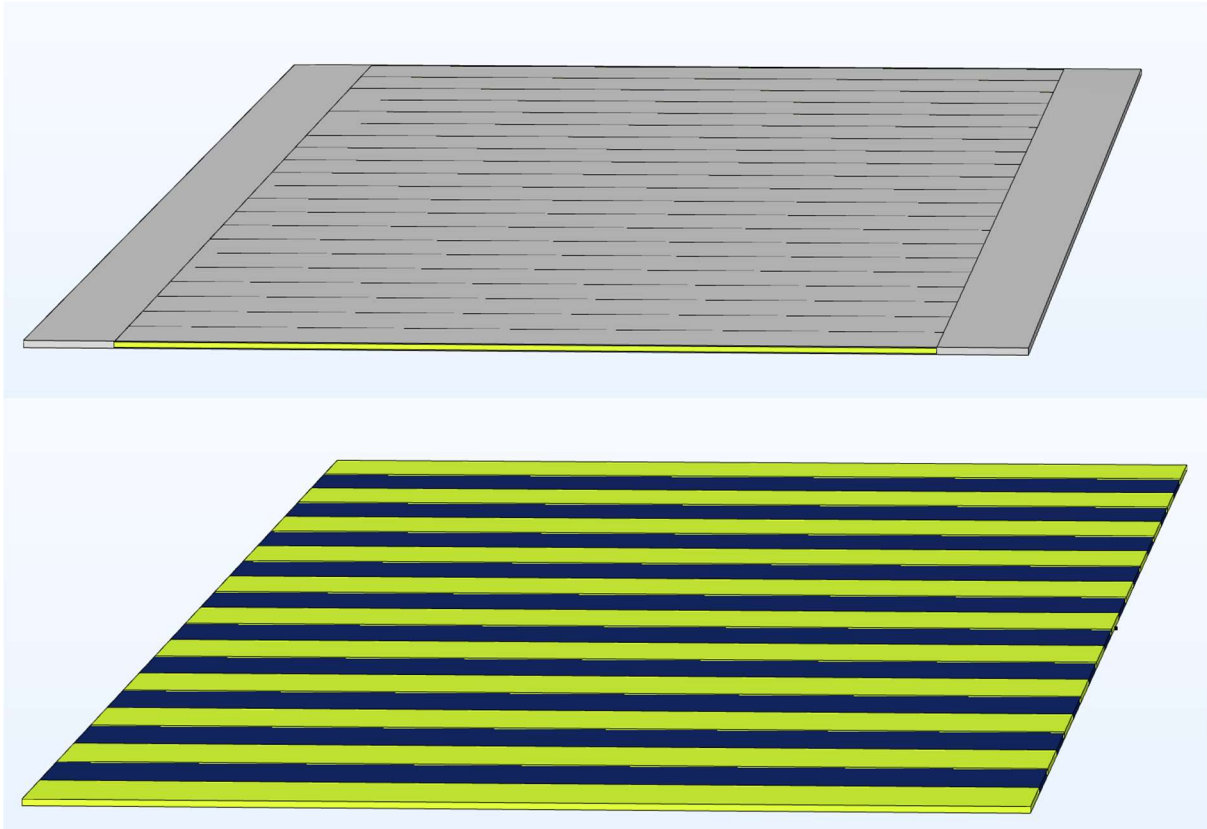


Figure 39: Design 2 Variation 4.

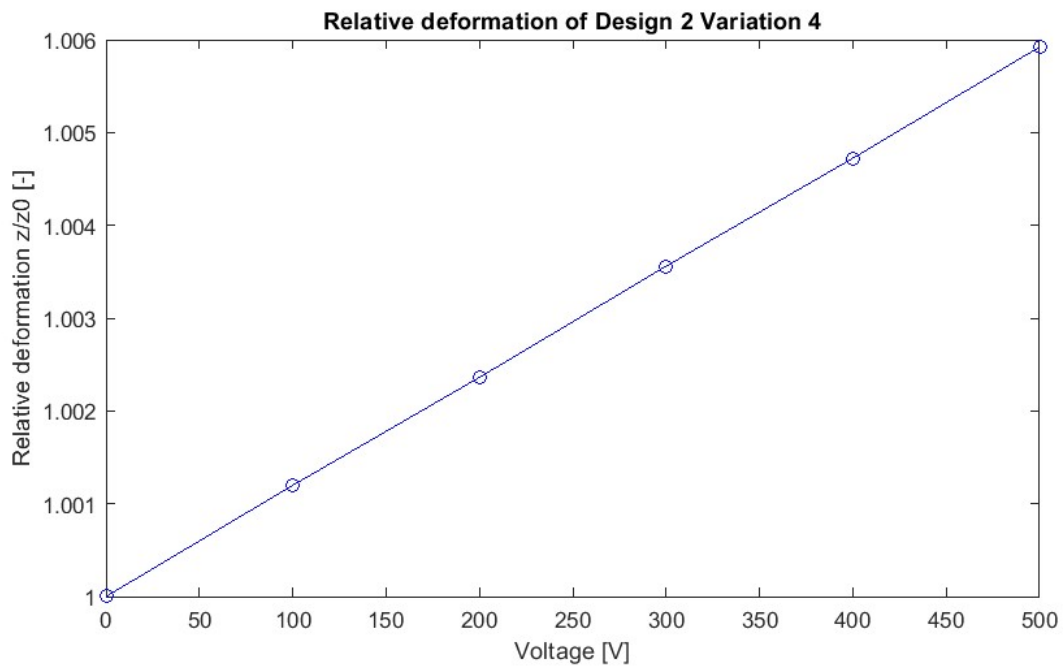


Figure 40: Voltage plotted versus relative deformation for Design 2 Variation 4.

This final variation also does not reach the 5.15% deformation threshold mentioned in Section 3.1 and sadly still performs worse than the original Piezo Design 2. The optimal direction of the piezoelectric strips seems to be latitudinal and multiple smaller strips give the largest effectiveness.

### 3.5 Conclusions

Two of the methods have been numerically tested, and after picking the two most promising designs and trying out a number of variations it is now time to pick one to develop into a final design. We start off with a few comparisons. Figure 41 shows the results for the Design 1 and its variations, and Figure 42 shows the results for Design 2 and its variations.

Table 4 gives the effectiveness of all the variations of the two designs.

Table 4: Effectiveness of the designs and their variations.

	Effectiveness [-]
<b>Design 1</b>	671%
<b>Variation 1</b>	89%
<b>Variation 2</b>	3500%
<b>Design 2</b>	2.12%
<b>Variation 1</b>	0.29%
<b>Variation 2</b>	0.32%
<b>Variation 3</b>	0.14%
<b>Variation 4</b>	0.59%

It seems clear which is the design to use moving forward. The second variation on the first design not only greatly increased its effectiveness but also improved its manufacturability, making the individual parts larger which will make the hinge easier to construct. In the next chapter we will take this design and detail a final design. After that this final design will be adapted to allow for an experimental setup.

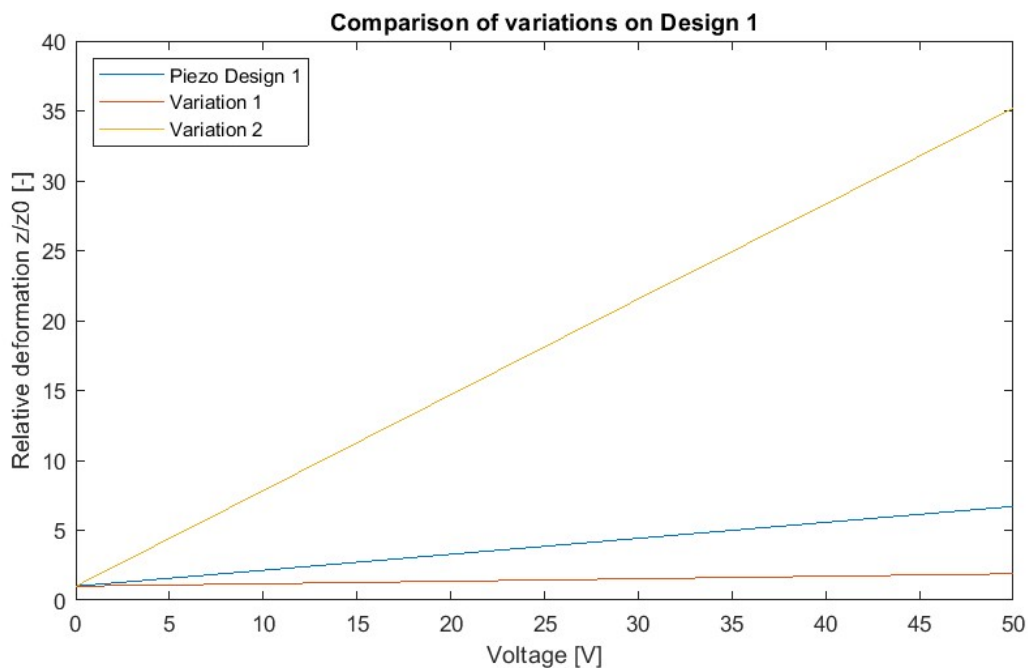


Figure 41: Comparison Design 1 and its variations.

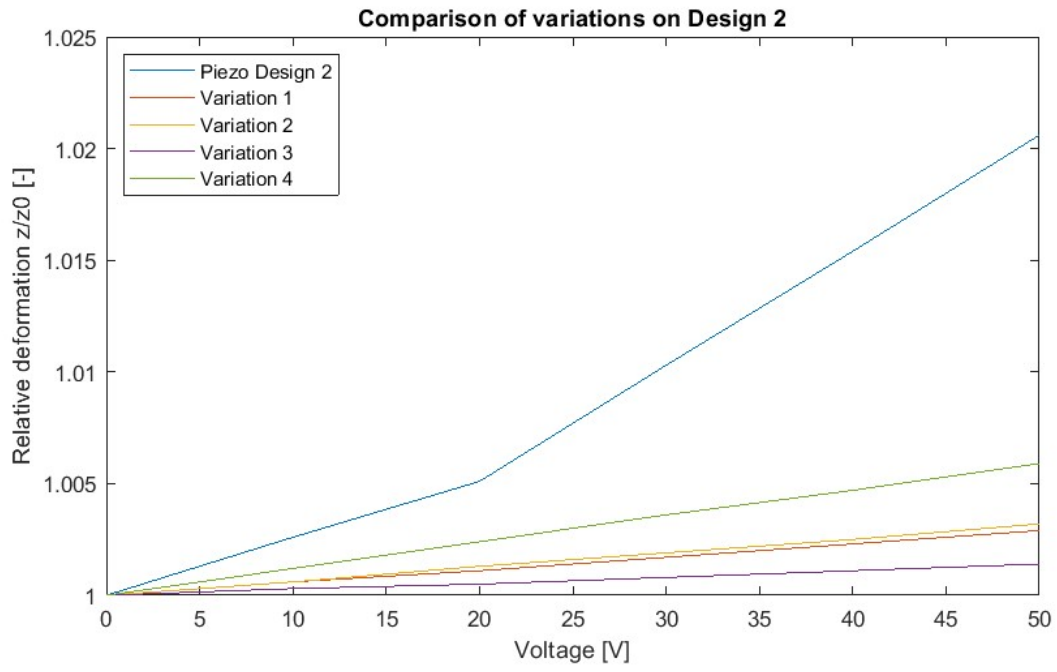


Figure 42: Comparison Design 2 and its variations.

## 4. Design Details and Experiment Adaptation

---

The elimination process has finally concluded, and a design is chosen that is deemed to be the best fit for achieving control in the Atalanta project. But while the working concept and general arrangement of the design are now clear, there are still some details to work out like material choice and final dimensions. Choices have to be made based on how the design will operate within the Atalanta project and its associated goals. It is also important to consider potential auxiliary systems required for the electric potential. All these factors are used to adapt the design into a finalized version that theoretically could be used in the Atalanta project. However, it is also important to find out whether the theorized potential can be realized in a real-world setting. This will be tested using an experimental set-up detailed in Chapter 5 and Appendix B. However, to be able to execute this experiment some changes will have to be made to the design due to available materials and method of testing. While these changes are not part of the finalized design, they do influence the results of the experiment and can be adapted into a design in further research executed within the Atalanta project. This chapter will explain some of the choices made for the final and experiment design, and give a more detailed description of its parts and dimensions.

Section 4.1 will detail the design process for the final design starting from the most successful design from the previous chapter. Section 4.2 will show the adaptation of the design based on the requirements and availability of materials for the experimental set-up.

### 4.1 Finalization of Design

The most promising design determined in Chapter 3 consisted of a sandwich structure with two piezoelectric films surrounded by adhesive positioned between three steel layers. While this design shows promising results, it is not yet ready for implementation within the Atalanta project. Three main characteristics need to be considered:

- **Material:** The materials picked for the numerical models were general materials not specifically tuned for the design application. Picking the right materials requires taking into account their effect on the performance of the design but also their commercial availability and the design specifications.
- **Electric potential:** The electric potential needs to be generated, converted and applied all from within the vehicle itself. This has influence on the available voltages.
- **Dimensions:** The dimensions need to fit within the Atalanta project but also influence availability of materials and ease of manufacturing.

Throughout this chapter these three characteristics will be used to tune the design and produce a finalized version.

#### 4.1.1 Material

In the previously discussed models, some standard materials were used, but it is now time to look more in depth at what is required of the design. The design consists of three materials, of which all three fulfill specific functions:

- The two outside and middle layers need to conduct electricity to allow for the application of an electric field over the piezoelectric material, and need to provide most of the stiffness to simulate the original wing hinges proposed by Bolsman (Bolsman, 2010).
- The piezoelectric films are of course the working materials which increase the stiffness due to the applied electric field.
- The adhesion films keep the construction together but also need to provide electrical insulation to prevent short-circuiting between the conducting layers.

On top of these specific functions all materials are subjected to relatively large deformations as the pitching angle can be up to  $80^\circ$  (Wang, 2017). The Atalanta project also operates on a flapping frequency of about  $27\text{ Hz}$ , which means the deformations are not only large but also frequent, and materials are preferred which can handle at least  $6000 * f$  cycles, a number proposed by Peters (Peters, 2016). Here  $f$  represents the flapping frequency and  $6000 * f$  represents 100 times a flight-time of one minute, which results in about  $10^6$  cycles for the chosen flapping frequency.

The original design by Bolsman uses spring steel for the wing hinge combined with polystyrene. Similarly, Wang's design also uses steel in combination with the dielectric material mylar. Since the effect of the wing hinge on the motion of the wing has been extensively discussed and modelled by these two authors, and since the steel is the main source of the hinge stiffness in both their designs, it is decided to also use steel for this report's design. Spring steel is available in thicknesses within the design range for the hinge (Jeveka, 2023). Its robust but flexible nature makes it a reliable material and its electrical properties allow it to create the electric field the design requires. Research by Myung (Myung, 2021) shows spring steel in bending conditions can handle up to  $10^8$  cycles. On top of this it is a widely commercially available material, which not only helps for setting up the experiment but is also beneficial in the theoretical situation the Atalanta project ever sees mass production.

For the piezoelectric material PZT is used in the numerical models, which represents Lead Zirconate Titanate, a piezoelectric ceramic material. It is a commonly used piezoelectric material used in ultrasonic transducers (Gururaja, 1985) and resonators (Smith, 2012). However, its ceramic nature means it is not the best match for the Atalanta project. Although (Badescu, 2008) shows relatively high effectiveness even after  $10^9$  cycles, the magnitude of the deformation in bending conditions is not high enough (Anton, 2012). A more fitting group of materials are the piezoelectric polymers, of which (Proto, 2016) denotes PVDF as the most available on the market. In terms of cycles (Shin, 2018) shows no notable decrease of effectiveness after  $10^7$  cycles. In addition (Wu, 2018) shows a high effectiveness for larger bending angles for a PVDF membrane. These factors together make us opt for PVDF piezoelectric film as the working piezoelectric material in the final design.

Finally, for the adhesion a thin film double-sided adhesive tape is chosen in the form of Kapton HN polyimide film (Kapton, 2023). Polyimide films boast high resistivity even at small thicknesses, and the films can be coated with adhesive to hold the structure together. Coupled with high flexibility and commercial availability this material is definitely sufficient for the hinge design.

#### 4.1.2 Electric Potential

As discussed thoroughly in the literature survey the biggest constraint for the Atalanta project is its weight. The current prototype is too heavy to achieve liftoff so when adding components to the design minimizing the mass is of the highest priority. The current design does yet feature any sort of battery pack but if a form of energy storage were implemented one could assume it would be as small as possible. Previously in Chapter 3 the applied voltage was modelled from 0 to  $500\text{ V}$  but considering the weight constraint and the significant weight both energy storage and step-up converters bring to the vehicle it is important to consider for a moment what voltages exactly are realistic in a FWMAV. A lot of assumptions will be made because designing a complete electric set-up is not within the scope of this research.

First, we look at miniature batteries to see what kind of voltages we are dealing with on this scale. Recent research on high-voltage miniature batteries by Kim show a voltage up to  $12.5\text{ V}$  for a volume of less than  $0.165\text{ cm}^3$  (Kim, 2023). The batteries use bifacial dense electrodeposited  $\text{LiCoO}_2$  cathodes and lithium anodes, and are used to power motors and actuators. While this voltage is quite low when

compared to the 500 V used in the numerical models there are ways to boost up the voltage a little bit, specifically DC-DC step-up converters. While some very specialized extremely high effectiveness step-up converters exist, such as a 3.7 V DC to 100 V AC converter (Xu, 2018), or a 3 – 5 V DC to 200 V DC-AC converter (Chen, 2018), these convert to AC currents and weigh 91 g and 108 g respectively. It goes without saying that these types of weights are not viable for a 10 g flying vehicle. In the commercial sector one can find DC-DC converters that can step from 2 V to 28 V (Electronicavoorjou, 2023), or from 3 V to 35 V (Components101, 2023). These converters show high but more realistic weights of 4.4 g and about 7 g respectively. Combined with the battery these electrical systems still take up significantly too much weight but with a healthy dose of optimism for the future voltages up to 35 V can be considered for the design. Any numerical models run from this point onward will take voltages up to 50 V into account which has to do with the experiment and will be explained in Section 4.2.

#### 4.1.3 Dimensions

In Chapter 2 a number of dimensions were introduced for the hinge, namely length  $L = 5 \text{ mm}$ , width  $d = 12.7 \text{ mm}$  and thickness  $t = 0.04 \text{ mm}$ . These dimensions were largely based on the Stick-slip hinge designed by Wang (Wang, 2017). Since Wang has done a lot of aerodynamic modelling emulating his design dimensions seemed like a smart choice. However, while the design that resulted from Chapter 3 showed a very high effectiveness, the choices made in this chapter will reduce the effectiveness by quite a bit. Piezoelectric polymers have significantly lower coupling factors than their ceramic counterparts (Preumont, 2018) and reducing the voltage will logically reduce the effectiveness as confirmed by Figure 32. We take a look at the model using the same layer thicknesses as Wang’s hinge, being  $20 \mu\text{m}$  for the center layer and  $5 \mu\text{m}$  for the other layers, and the newly chosen materials, shown in Figure 43.

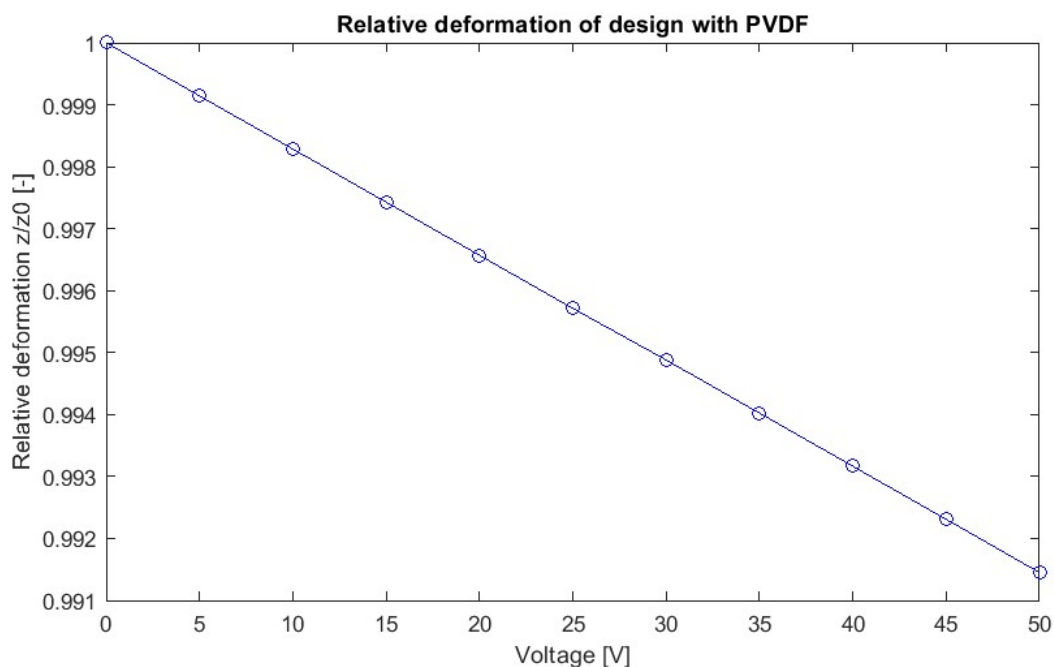


Figure 43: Relative deformation of design with PVDF.

Recalling the 5.15% threshold calculated in Section 3.1 this design does not fit the bill. To increase the effectiveness of the design through its dimensions, the most effective method is to change the ratio between piezoelectric material and the steel layers, in other words increasing the thickness of the sandwiched layers. Figure 44 shows an array of different thicknesses and their effectiveness. In this

design all steel layers are changed to be 0.01 mm thick to make manufacturing easier while keeping the same total area of steel.

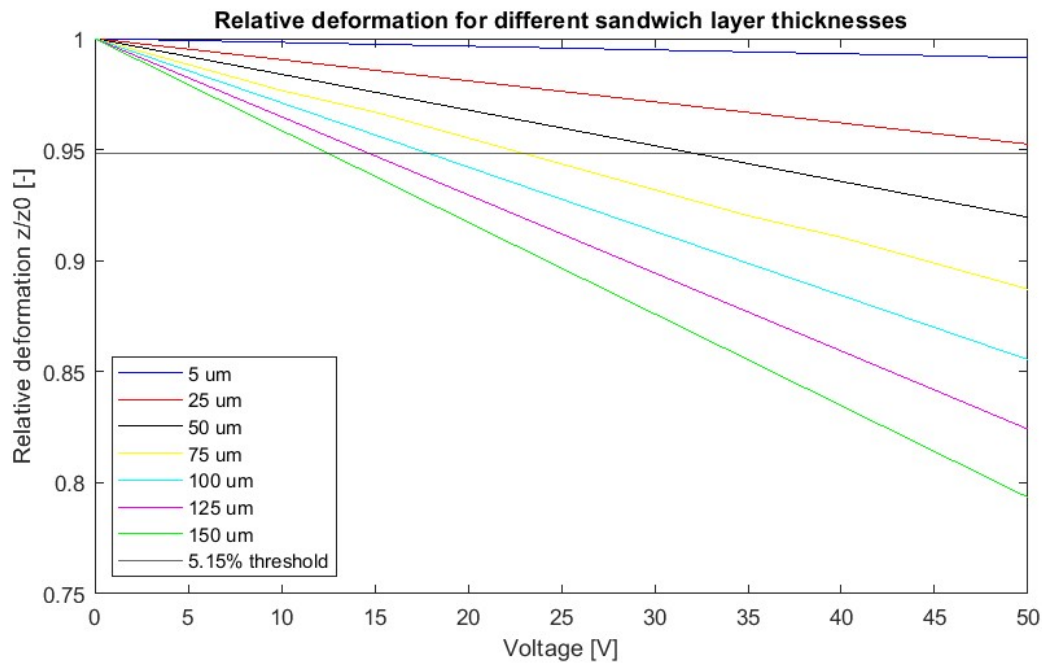


Figure 44: Voltage vs relative deformation for an array of different sandwich layer thicknesses.

In the theoretical case where a voltage of 50 V can be achieved within the Atalanta vehicle a thickness of around 25  $\mu m$  is required and for the currently viable voltage of 35 V a thickness of 50  $\mu m$  would be required. However, by using a thickness of 150  $\mu m$  the need for a converter could be eliminated entirely, greatly decreasing the weight of the electric system. For the final design a thickness of 150  $\mu m$  will be used since weight is the biggest design constraint, therefore making the result with a 150  $\mu m$  thickness the most likely to be adopted in the Atalanta design. In future research higher thicknesses could be used to tune the design for even lower voltages. Or in a more extreme form research could be done into constructing the hinge out of electrode coated PVDF films such as produced by PolyK (PolyK, 2023).

#### 4.1.4 Final Design

We consider the sum of all that we have learned from the previous subsections to formulate a final design. This design is the most optimal according to the theory in this research for use as a wing hinge within the Atalanta project. A recap of final changes is given in Table 5.

Table 5: Recap of changes made in the three characteristic categories.

Characteristic	Changes
<b>Material</b>	<i>Conducting layers:</i> Spring steel <i>Adhesion:</i> Polyimide adhesion film <i>Piezoelectric material:</i> PVDF
<b>Electric potential</b>	0 to 50 V DC
<b>Dimensions</b>	<i>Steel layers:</i> 10 $\mu m$ <i>Sandwich layers:</i> 150 $\mu m$

The final dimensions are illustrated in Figures 45 and 46. Here gray represents steel, dark blue represents adhesion film and yellow represents piezoelectric material. The hinge is fixed at one of the long ends with the boundary load being applied at the other long end.

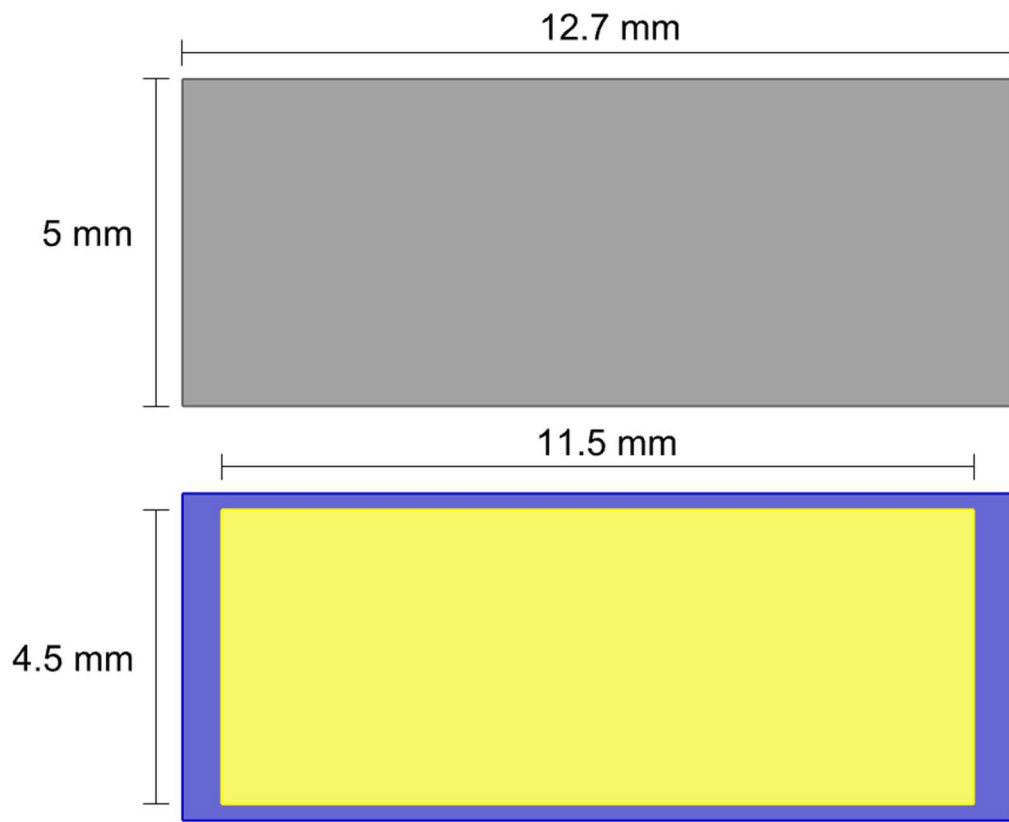


Figure 45: Final dimensions as seen from the top.

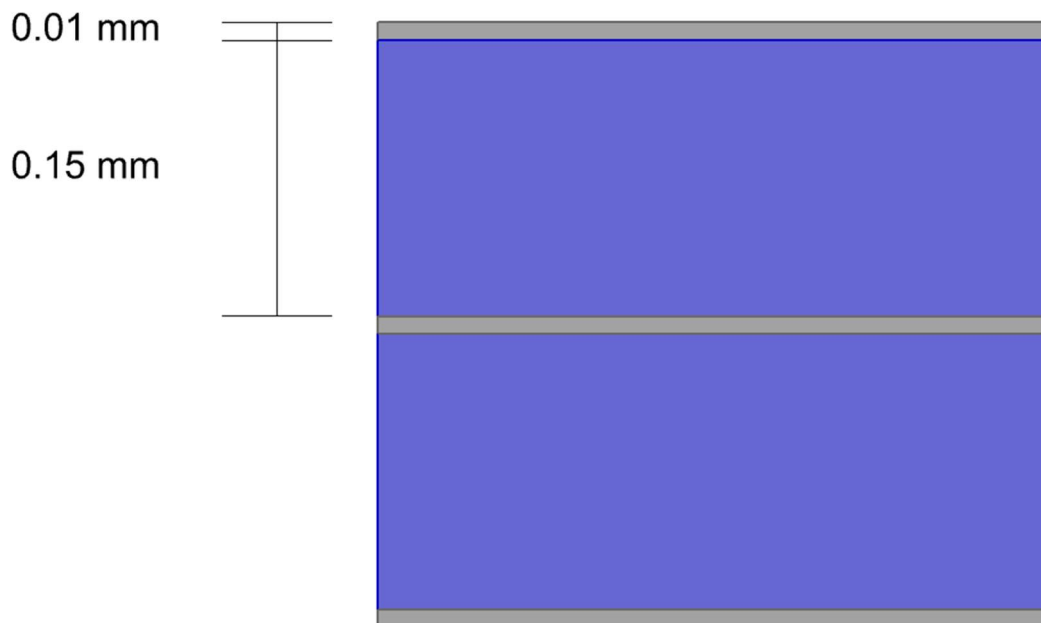


Figure 46: Final dimensions as seen from the side.

## 4.2 Experiment Adaptation

The experiment, as detailed in the next chapter, will tell us whether the theoretically viable hinge design will actually work in the real world and show results as promising as the models give us. However, resources are somewhat limited for a master thesis so the design went through a number of changes to properly adapt it for an experimental validation. These changes had to keep in mind the availability of materials, both in price and time, the assembly of the hinge and the instruments available in the lab. This section will discuss the changes in a similar way to the previous section, keeping the same three categories in mind that are recapped in Table 5.

### 4.2.1 Material

The university generally provides student with a plethora of options in ordering materials and machinery for creating your own materials, but these processes are often expensive and time consuming. In building an experimental set-up to show the working principal of the design some materials were picked simply due to being available already, while others were ordered.

The 10  $\mu\text{m}$  thick steel film is available in the PME lab, in strips with a width of 12.7 mm which uncoincidentally is the exact width of the hinge.

For the adhesion film two films were available, 3M 300LSE with a thickness of 50  $\mu\text{m}$  and 3M 7955MP with a thickness of 132  $\mu\text{m}$ . Both films were used in the assembly of a hinge prototype and it was found that the 132  $\mu\text{m}$  thick film was a lot easier to work with. Combining this with the fact that the final design uses a 150  $\mu\text{m}$  thick adhesive film, it is decided to continue further prototypes using the 3M 7955MP. The film boasts a high bond strength and is recommended for use in industrial electronic device assembly (3M, 2023).

The initial plan for the piezoelectric polymer was to use stencil printing to print a layer of *Piezotech RT-TS*, a printable P(VDF-TrFE-CTFE) terpolymer. This printing method promises easy assembly as all that is required is pouring a liquid into a mold and the piezoelectric film would form itself to fit the space made for it. However, on closer inspection, it proves more complicated than initially thought due to absorption in the peel-off layers of the adhesion film, and a relatively low electrostrictive coefficient of the resulting film (Arkema, 2023). The material also requires a thermal annealing, which might negatively impact the other materials in the design. Instead, PVDF film was ordered made with the Arkema ink but produced by a specialized lab, allowing for high quality film, pre-annealed film with the option for poling. The film chosen is a uniaxially poled PVDF film with a high coupling coefficient in the 31-direction, which is the bending direction used in the final design as mentioned in Subsection 2.2.1 (PolyK, 2023).

### 4.2.2 Electric Potential

The electric potential that can be generated in a lab is easily upwards of 500 V and therefore the main constraint for the voltage is design voltage and lab safety. As mentioned in Subsection 4.1.2 voltages available through commercial step-up converters are at most 35 V, but the maximum voltage in Figures 43 and 44 was taken as 50 V. The decision for this higher maximum voltage is due to two reasons:

- A higher voltage means a higher effectiveness according to the models, and for the experimental set-up it is decided that it would be beneficial to grant some room in this department to help the measurement process.
- The 50 V number specifically is chosen due to lab safety at the University allowing for up to 50 V without requiring special safety measures. These measures in this case would require the entire set-up to be shielded by transparent and insulating material, greatly increasing the complexity of the experimental set-up.

Even though this voltage is a little higher than the viable voltage discussed in Subsection 4.1.2 with a little bit of optimism it is not too hard to imagine that a method of generating this voltage in a micro-sized drone is already possible through some more complicated processes or will be possible in the near future due to technological advances.

#### 4.2.3 Dimensions

Concerning the dimensions, we start off continuing the train of thought on the electric potential. How the potential is applied to the hinge in the Atalanta design is not discussed in this thesis because it depends heavily on the design of the Atalanta itself, which is far from finished, and the other on-board electrical systems such as optical systems for control and navigation (Van Vrede, 2018) and the available power supply. For the experiment however, a way of applying the voltages needs to be integrated into the design. For this purpose, three contacts, each attached to one of the three steel layers, are added to the design, each with a length of  $7.9\text{ mm}$  and a width of  $3.356\text{ mm}$ .

The previous subsection mentioned using a higher voltage than realistically available to increase effectiveness and thus improve measurement results. In the dimensions category a similar change is applied, in the form of increasing the length of the part of the hinge containing the piezoelectric material, as well as further increasing the length of the hinge overall. This change not only increases the effectiveness of the design but also makes both assembly of the hinge itself and the full experimental set-up significantly easier. The length of the piezoelectric material is increased from  $4.5\text{ mm}$  to  $12.6\text{ mm}$ . The overall length of the effective part of the hinge is increased from  $5\text{ mm}$  to  $13.6\text{ mm}$ . The total hinge length is increased to  $15\text{ mm}$  to leave room for the clamping structure.

#### 4.2.4 Experiment Design

We once again consider the sum of all the changes made in the previous subsections to see what the final design for the experiment looks like. The changes are recapped in Table 6.

Table 6: Recap of changes made to the design for the experimental set-up.

Characteristic	Changes
<b>Material</b>	<i>Conducting layers:</i> Spring steel <i>Adhesion:</i> 3M 7955MP Double Lined Adhesive Transfer Tape <i>Piezoelectric material:</i> PolyK Uniaxially Poled PVDF Film
<b>Electric potential</b>	0 to 50 V DC
<b>Dimensions</b>	Piezoelectric length changed to $12.6\text{ mm}$ Effective length changed to $13.6\text{ mm}$ Total length changed to $15\text{ mm}$ Three $7.9$ by $3.356\text{ mm}$ contacts added

Illustrations for the design are shown in Figures 47 through 49. Here again gray represents steel, dark blue represents adhesive film and yellow represents PVDF.

The assembly of the hinge is shown in Appendix A.

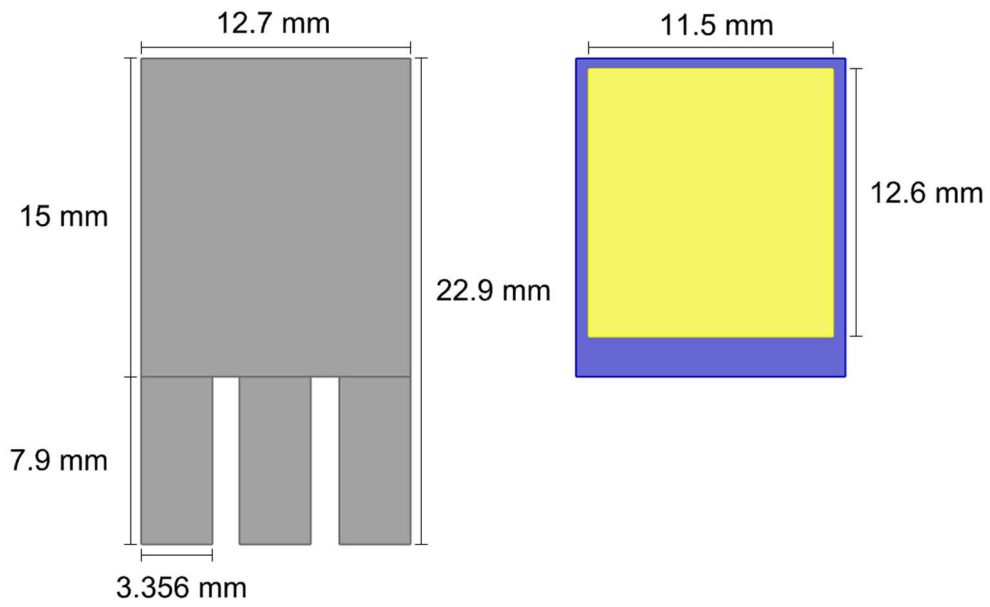


Figure 47: Dimensions of experiment design as seen from the top.

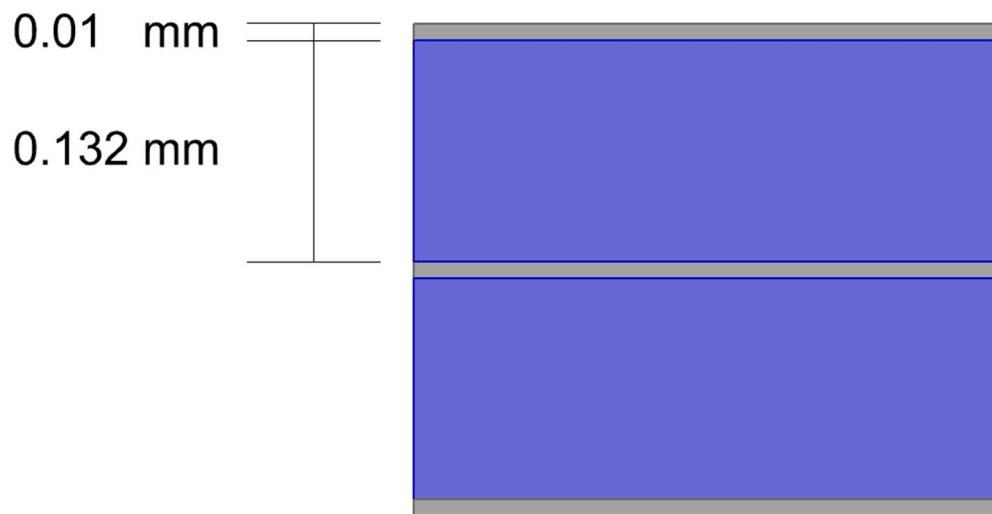


Figure 48: Dimensions of experiment design as seen from the side.

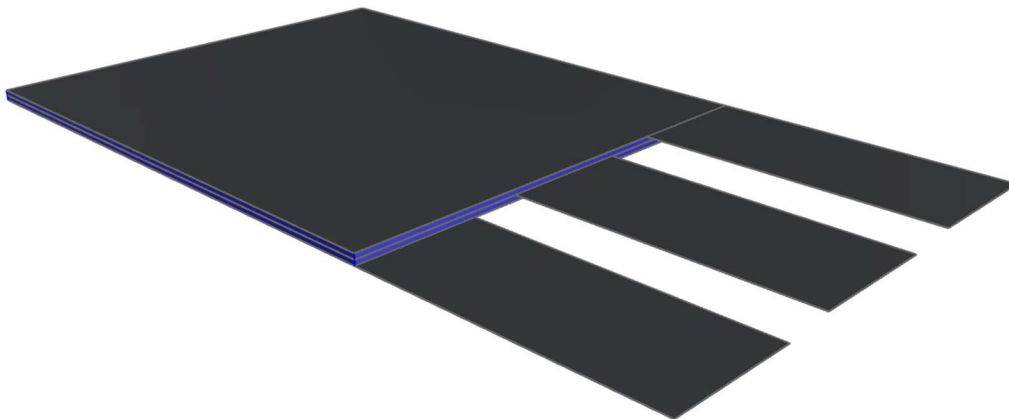


Figure 49: Angled perspective of experiment design to show contact offset.

## 5. Experimental Analysis

---

A final design has been presented based on the theoretical knowledge developed so far into the research project. This design is deemed the most fitting for the Atalanta project within the scope of the research assuming that the numerical models are accurate. However, the Atalanta drone is not just a theoretical project, but a real vehicle. It is important to see through the execution of an experiment whether the design actually does what the models say it will do, and in the process garner additional knowledge about assembly and operation. Setting up an experiment is a great way not only to validate the models, but also to see whether a project is actually realistic. In the previous chapter an extra design was detailed, specifically to be used in the experiment. This design features larger dimension to make assembly of the hinge and the experimental set-up easier and has contacts added to the design to allow for the application of the electric potential.

In this chapter the experiment is explained and detailed. Section 5.1 explains the goal of the experiment and discusses two different methods of analysis. Section 5.2 will discuss the methodology behind the experiment. Section 5.3 talks about the set-up and its individual elements. Section 5.4 shows the results of the experiment. Finally, in Section 5.5 the results are discussed and a conclusion is drawn about the viability of the design.

### 5.1 Goal

Before you start an experiment, it is important to consider what exactly it is that you want to know. In the case of this research, after the elimination of the materials based on damping in Section 2.4, all the remaining methods and materials were focused on variable stiffness. The final design reflects this, showing a reduction in deformation caused by a load due to a change in stiffness in the piezoelectric material and an induced stress in the structure caused by piezoelectric deformation. Section 2.1 related the 0.5% lift threshold posed by Lu (Lu, 2013) to a 5.15% stiffness change in the wing hinge. Thus, it makes sense for the experiment to try and determine the stiffness of the design for different electric potentials, and see if the measured difference in stiffness agrees with the model and the design works as intended. However, stiffness is not a value that can be measured directly. It has to be derived from different measured parameters. Determining a structures stiffness experimentally is done through measuring its deformations. There are many different measurement methods, such as using a cantilever beam pressed into an object's surface (Yang, 2008), using two springs with different spring constants to press against an object (Peng, 2010), or using resonant vibrational frequencies (Murayama, 2004). In this section, two different methods will be considered, namely a static and a dynamic method. The two methods will briefly be explained in the next two subsections.

#### 5.1.1 Static Method

The first method is the static method. This method is based on one of the most fundamental definitions of stiffness, discussed earlier in Section 3.1, and recapped here in Equation 5-1 (Bauchau, 2009).

$$k = \frac{p}{w}. \tag{5-1}$$

Here, bending stiffness  $k$  is defined as being a direct relation between the applied bending load  $p$  and the beam deflection  $w$ . For small deflections and angles this analytical formula can be used to fairly accurately calculate the stiffness. On very small scales knowing the magnitude of the applied force can be tough due to deformation of the mechanism applying the force itself (Sul, 2017). However, for the hinge design we can simply use gravity to generate a force.

The experiment set-up would consist of the hinge clamped horizontally, with a boundary load being applied on the free end through the use of for instance a magnet with a known weight. When the magnet is attached to the hinge, due to the gravitational load the hinge would deform downward. Measuring this deformation using a laser would grant enough information to calculate the stiffness using Equation 5-1. Next the magnet is removed and the hinge is restored to its original position. A voltage is applied and the magnet is once again attached, deforming the hinge. Calculating this stiffness and comparing it to the previously calculated stiffness would grant the difference in stiffness, showing whether the design is able to achieve the required stiffness change to allow for control of the FWMAV. The principle is illustrated in Figure 50.

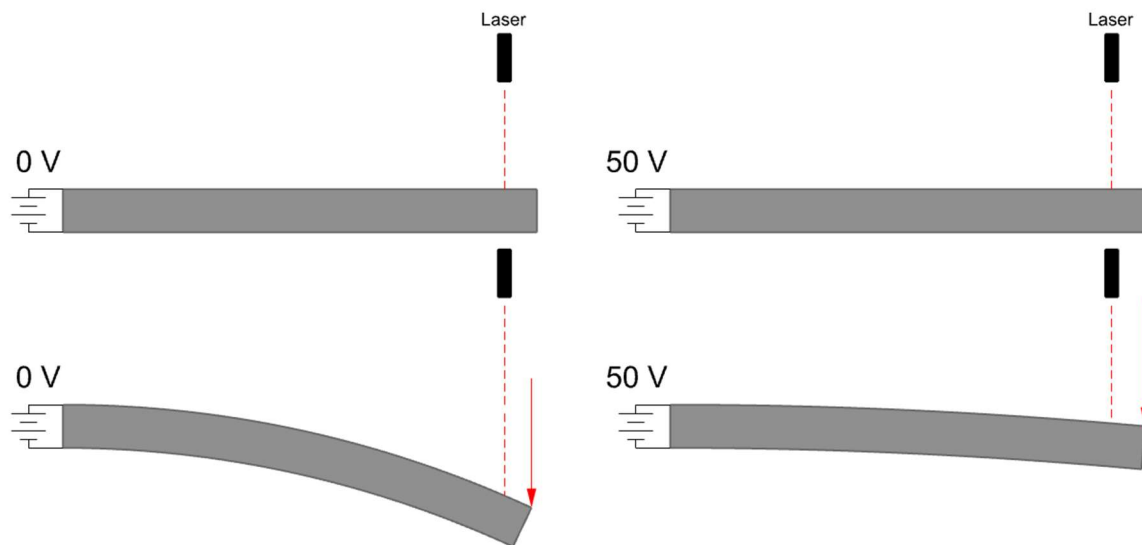


Figure 50: Illustration of the static measurement.

This set-up coincides with how the numerical models were used to simulate a change in bending stiffness. However, a problem with this method presents itself when looking at the results of the numerical models. Throughout this report so far, the focus was on the relative vertical deformation, defined as the deformed  $z$ -coordinate divided by the  $z$ -coordinate from when there is no voltage applied, indicated in graphs by  $z/z_0$ . This gives a good idea of a design's effectiveness compared to a different design, but it gives no insight on how big or small the actual deformations are. Figure 51 shows the magnitude of the difference between minimal and maximal deformations throughout the design process. Note that the  $y$ -axis is in log-scale.

Figure 51 shows that the difference between minimum and maximum deformations has decreased quite a lot throughout the design process. The main reasons for this were the switch to PVDF material and the reduction of the voltage to a maximum of  $50\text{ V}$ . For the experiment design the difference is about  $8 \cdot 10^{-6}\text{ m}$ , or about  $8\ \mu\text{m}$ . The measuring precision of laser displacement triangulation sensor is about  $8\ \mu\text{m}$  (Micro-Epsilon, 2023). This means that unless extremely precise measurement techniques are available this method of experimentation is not viable for the current design.

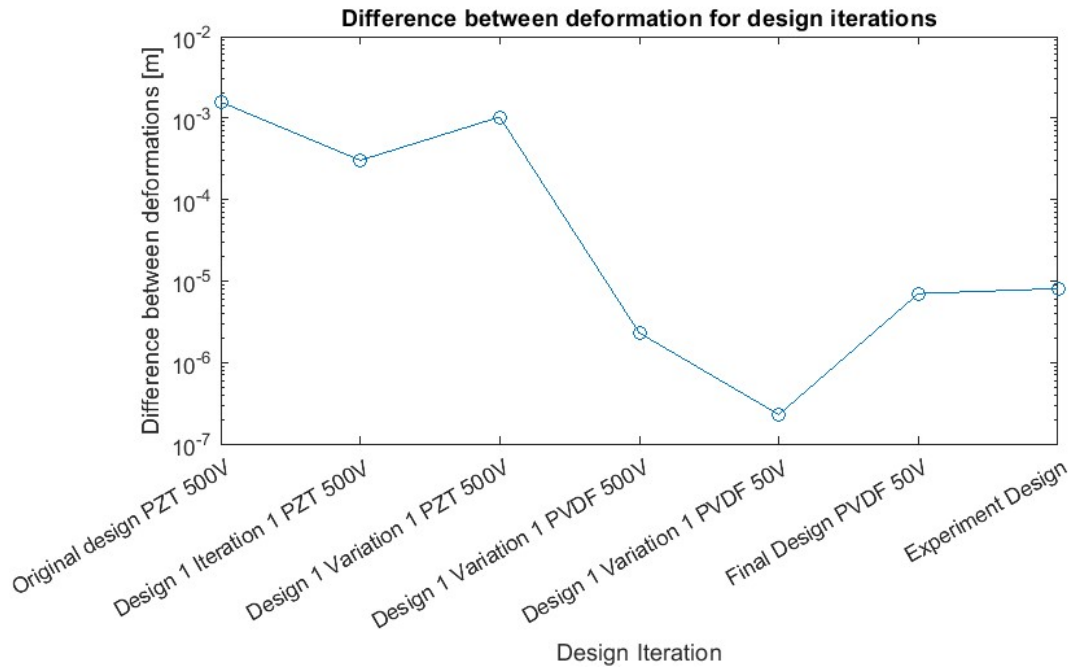


Figure 51: Difference between minimum and maximum deformations of different design iterations.

### 5.1.2 Dynamic Method

The second method is the dynamic method. This method uses the eigenfrequency of the system to measure the stiffness. The relation between stiffness, mass and eigenfrequency for a mass-spring system is given in Equation 5-2 (COMSOL, 2018).

$$\omega_0 = \sqrt{\frac{k}{m}}. \quad (5-2)$$

If we imagine the hinge as a mass-stiffness system we can calculate a sort of equivalent stiffness using this equation and by comparing stiffnesses for different voltages we can once again calculate the change in bending stiffness of the hinge. The benefits of the dynamic method are:

- In resonance the structure shows a response amplitude that is a relative maximum, allowing for relatively large deformations that can more easily be measured.
- Additional components can be added to the structure to influence the eigenfrequencies, and as long as the dimensions and properties of these parts are known the original stiffness can still be calculated with relatively high accuracy (Banerjee, 2012).

An experimental set-up would consist of the hinge hanging vertically in some form of clamping mechanism that is actuated at a variable frequency. Measuring the deflection using a laser the eigenfrequencies could be determined by locating the frequency at which the deflections are maximal. The set-up is illustrated in Figure 52.

The problem the static method has where deformations in the current design are not large enough to measure accurately are not present in the dynamic method, due to resonance responses being relatively high in amplitude and the ability to add components with known properties to influence the eigenfrequency and its amplitude. This improved measurability and flexibility made this method the preferred choice for this research, and the execution will be explained in more detail in the next few sections.

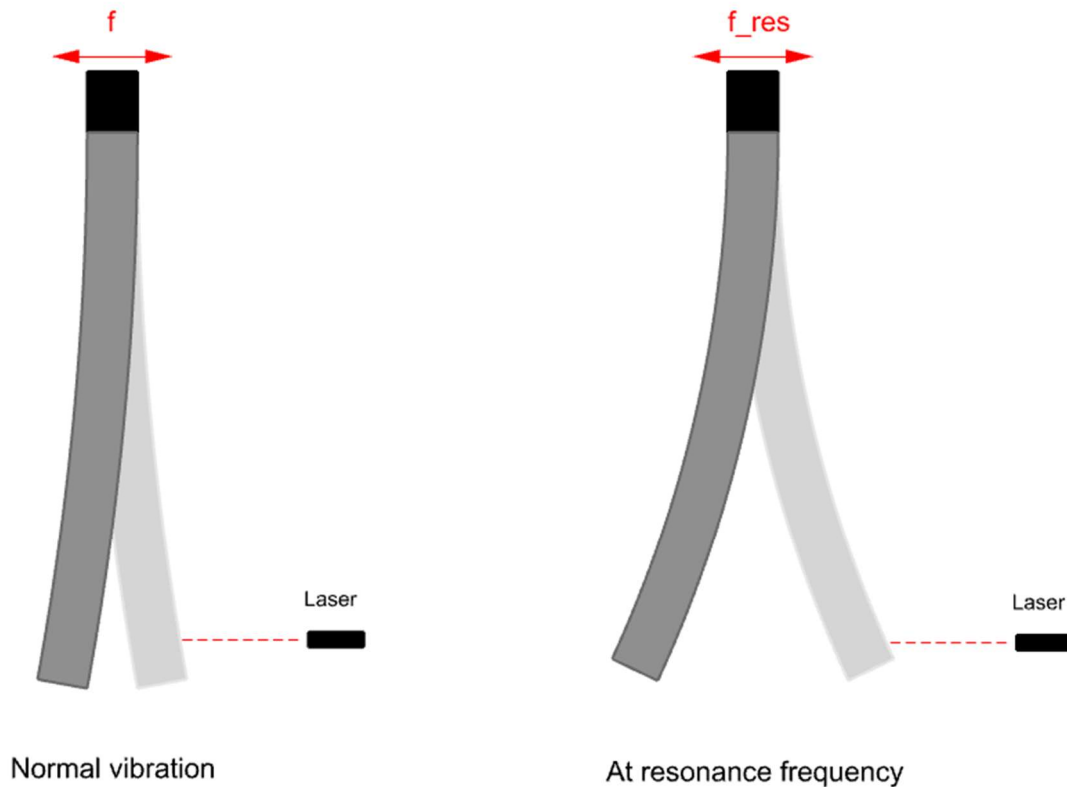


Figure 52: Illustration of the dynamic measurement.

## 5.2 Methodology

Before the measuring starts it is important to know what exactly needs to be measured and what we want to get out of it. The property that we want to know is the change in stiffness, for which the parameter to be calculated is the stiffness. As mentioned in Subsection 5.1.2 the eigenfrequency for a mass-spring system is  $\omega = \sqrt{\frac{k}{m}}$ . This can be rewritten to:

$$k = m * \omega^2. \quad (5-3)$$

This means if we want to know the stiffness, we will need the mass and the eigenfrequency. The mass of the system is known, since the mass of the hinge and any attached elements can be measured by simply weighing them. The eigenfrequency is determined from the measurement set-up as shown in Figure 52. A laser is used to measure the amplitude of the system by measuring the deflection of the end. Measuring over a range of different frequencies and noting the amplitude for each one will allow for the creation of a frequency-displacement plot. The location of peak values in this plot will correspond to eigenfrequencies of the system (Vlab, 2011). This method is used for crack detection in cantilever beams, with Figure 53 showing an example of a plot (Elshamy, 2018). Here the amplitude is measured in terms of acceleration but the principle is the same.

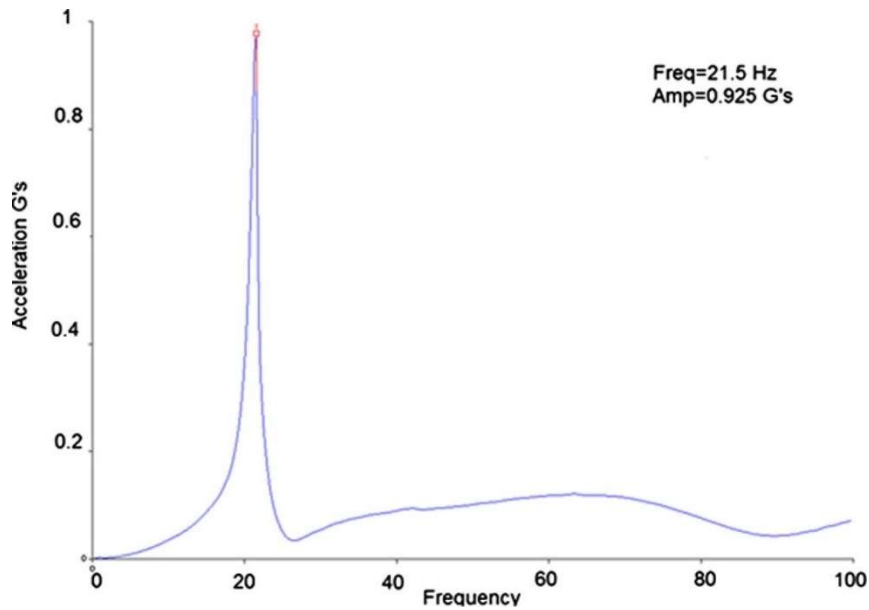


Figure 53: Example of eigenfrequency determination through a frequency-acceleration plot. Image from (Elshamy, 2018).

To increase the deformation and allow for tuning of the eigenfrequency an additional structural element is added to the hinge. In the completed Atalanta project, a wing will be added to the end of the hinge, but for the experiment a simple steel strip is added. The new structure is shown in Figure 54. Here the smaller rectangle on the left is the hinge with the fixed end being the left edge, and the larger rectangle is the added steel strip. The reason the strip is added on the top layer instead of attached under the hinge like the wing would be is to make it easier to attach and prevent short-circuiting of the electrical circuit.

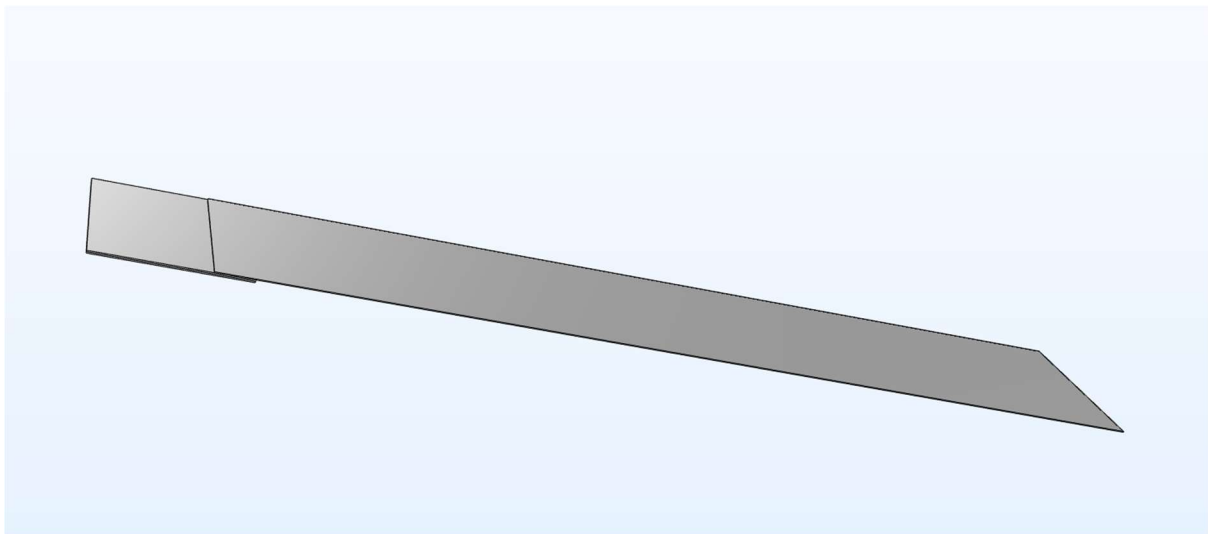


Figure 54: Hinge with additional structure.

The strip is made of spring steel with a thickness of  $0.1\text{ mm}$ , or ten times thicker than the steel used in the hinge design. This is a readily available thickness of steel and makes the strip robust so it can be handled easily. This strip can be implemented in the numerical model to analyze the eigenfrequencies for the system with and without an electric potential. The resulting eigenfrequencies and their relative difference are given in Table 7.

Table 7: Eigenfrequencies for the modified structure.

Length strip = 6 · Length hinge			
Eigenfrequency [Hz]	0 V	50 V	Difference
First	10.561	10.639	0.74%
Second	84.531	84.584	0.06%
Length strip = 8 · Length hinge			
Eigenfrequency [Hz]	0 V	50 V	Difference
First	6.1612	6.2810	1.94%
Second	55.861	55.931	0.13%
Length strip = 10 · Length hinge			
Eigenfrequency [Hz]	0 V	50 V	Difference
First	3.3951	3.5062	3.27%
Second	22.807	22.913	0.46%

Both the eight- and ten-times hinge length strips show a large difference between the first eigenfrequency with and without the applied voltage, but the strip of ten times hinge length also shows a large difference for the second eigenfrequency. Application of an actuation frequency in the range of 1/100<sup>th</sup> of a Hz is viable with a signal generator, so the strip of ten times hinge length seems sufficient for the experimental set-up. The change in eigenfrequency for this length based on the first eigenfrequency seems to be about 5.7% according to formula 5-3.

The numerical model of course calculates the eigenfrequency for the entire structure, not just the hinge, and thus allows for only calculating the stiffness of the entire structure if Equation 5-3 is used. So, to allow for approximation of the hinge stiffness an analytical model is set up. The model approximates the structure as a system consisting of two springs and two masses, each with their own mass and stiffness coefficient, shown in Figure 55.

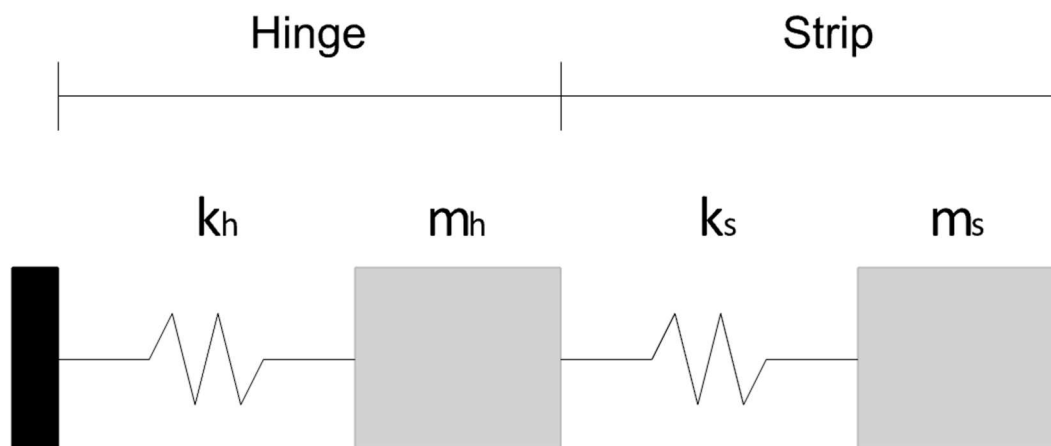


Figure 55: Illustration of mass-spring system.

The mass of the hinge and strip,  $m_h$  and  $m_s$  respectively, can be measured, and the stiffness of the strip,  $k_s$ , can be calculated since the strip dimensions and material are known. This leaves the stiffness of the

hinge  $k_h$  as the only unknown. To calculate this stiffness when the eigenfrequency is known we use an analytical solution for the eigenfrequency (Tatum, 2013). We start off with the kinetic and potential energies  $T$  and  $V$ .

$$T = \frac{1}{2}m_h\dot{x}_h^2 + \frac{1}{2}m_s\dot{x}_s^2. \quad (5-4)$$

$$V = \frac{1}{2}k_hx_h^2 + \frac{1}{2}k_s(x_s - x_h)^2. \quad (5-5)$$

From these we can derive the Lagrange's equations of motion.

$$m_h\ddot{x}_h = -(k_h + k_s)x_h + k_sx_s. \quad (5-6)$$

$$m_s\ddot{x}_s = k_sx_h - k_sx_s. \quad (5-7)$$

Next, we seek solutions of the form  $\ddot{x}_h = -\omega^2x_h$  and  $\ddot{x}_s = -\omega^2x_s$ . We substitute these into Equations 5-6 and 5-7, and we obtain the following:

$$(k_h + k_s - m_h\omega^2)x_h - k_sx_s = 0. \quad (5-8)$$

$$k_sx_h - (k_s - m_s\omega^2)x_s = 0. \quad (5-9)$$

Expressing Equations 5-8 and 5-9 in terms of  $\frac{x_s}{x_h}$  and equating them finally gives the angular frequencies of the normal modes:

$$m_hm_s\omega^4 - (m_hk_s + m_s k_h + m_s k_s)\omega^2 + k_hk_s = 0. \quad (5-10)$$

Expressed in terms of the hinge stiffness  $k_h$  this is:

$$k_h = \frac{m_hk_s\omega^2 - m_hm_s\omega^4 + k_s\omega^2}{-m_s\omega^2 + k_s}. \quad (5-11)$$

Of course, the structure does not actually consist of two masses connected by two springs, but more closely resembles two cantilever beams attached end to end. To reflect this, bending stiffness is used for the spring stiffnesses, and effective masses of the beams are used for the masses (Irvine, 2012).

Equation 5-12 shows the bending stiffness and Equation 5-13 shows the effective mass for a cantilever beam, where  $\mu$  is the mass per length of the beam.

$$k = 3\frac{EI}{L^3}. \quad (5-12)$$

$$m_{eff} = 0.2235 * \mu L. \quad (5-13)$$

Figure 56 shows the obtained first eigenfrequencies of the model and compares them to the first eigenfrequencies found by the numerical models. While the eigenfrequencies differ with about a factor two, the trend in the eigenfrequencies is very similar. Figure 57 shows the difference between eigenfrequencies for both models. This figure shows that the model predicts the difference between the eigenfrequencies fairly well. Since the goal of the experiment is to see if the hinge has a high enough effectiveness to cause a change in lift of 0.5%, and this is achieved by reaching a change in stiffness of 5.15%, this analytical model is of use in approximating this change in stiffness.

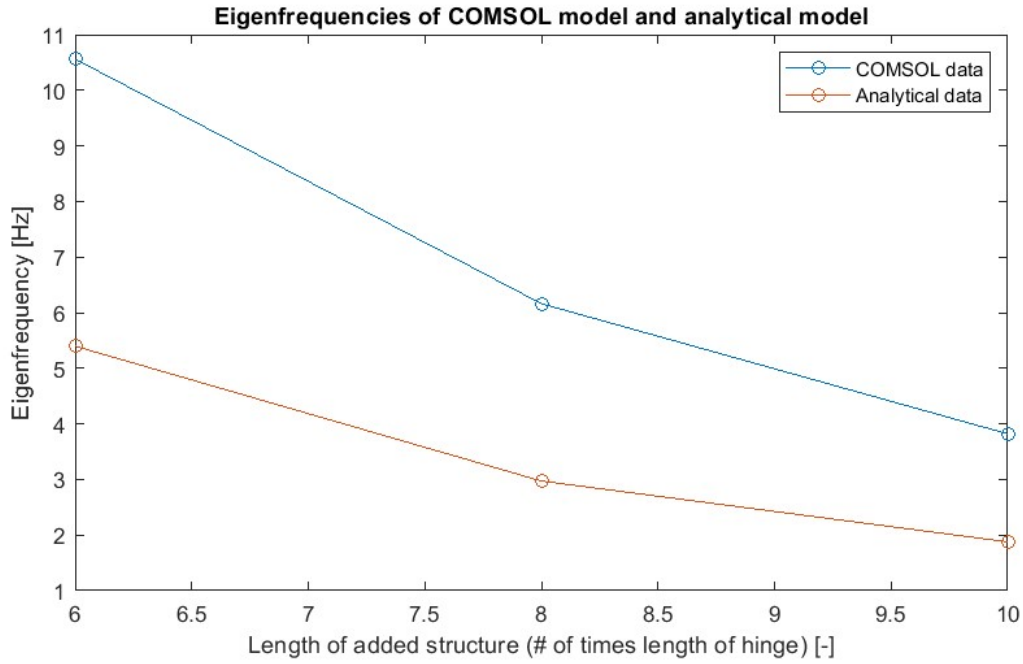


Figure 56: Eigenfrequencies of analytical model compared to numerical results.

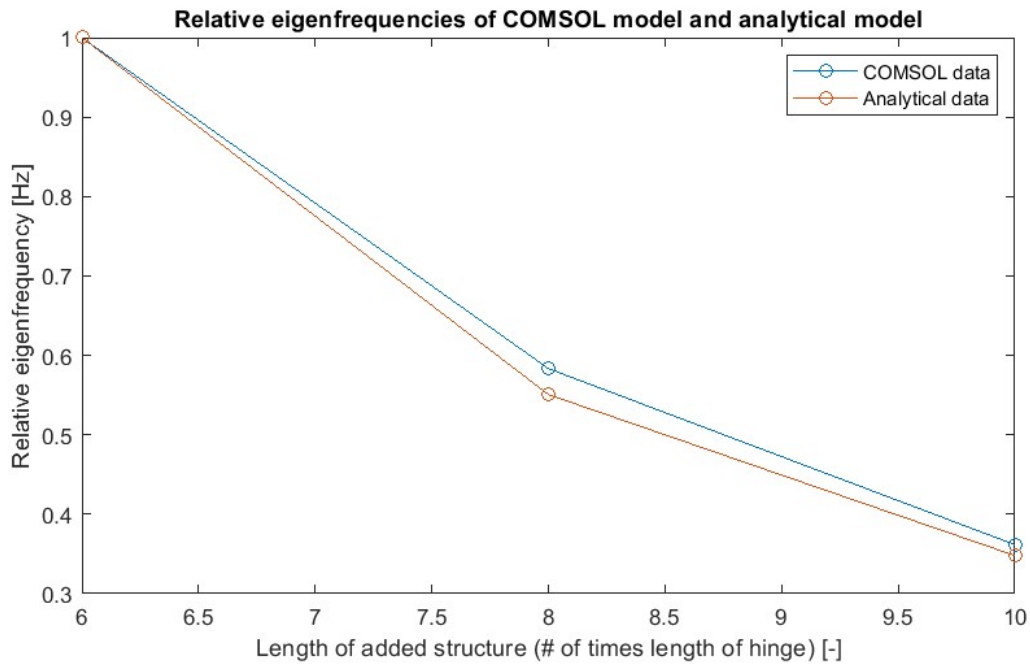


Figure 57: Relative eigenfrequencies of analytical model compared to numerical results.

## 5.3 Materials

The methodology describes the theory behind the experiment, but now it is time to move into the real world. An experimental set-up is built that fulfills a number of requirements. This section discusses the requirements, mentions the machines and components used to fulfill these requirements, and briefly shows the final set-up.

We know what we want to measure, but have not yet discussed how to measure it. Subsection 5.1.2 gave a global idea of what a set-up for the dynamic method should include, but a lot was left to the imagination. To detail a working set-up, we start off with a schematic overview of the set-up, to see what

materials are required. This schematic is shown in Figure 58. From this figure a list of requirements is detailed. The numbers shown Figure 58 correspond to equipment mentioned in Table 8.

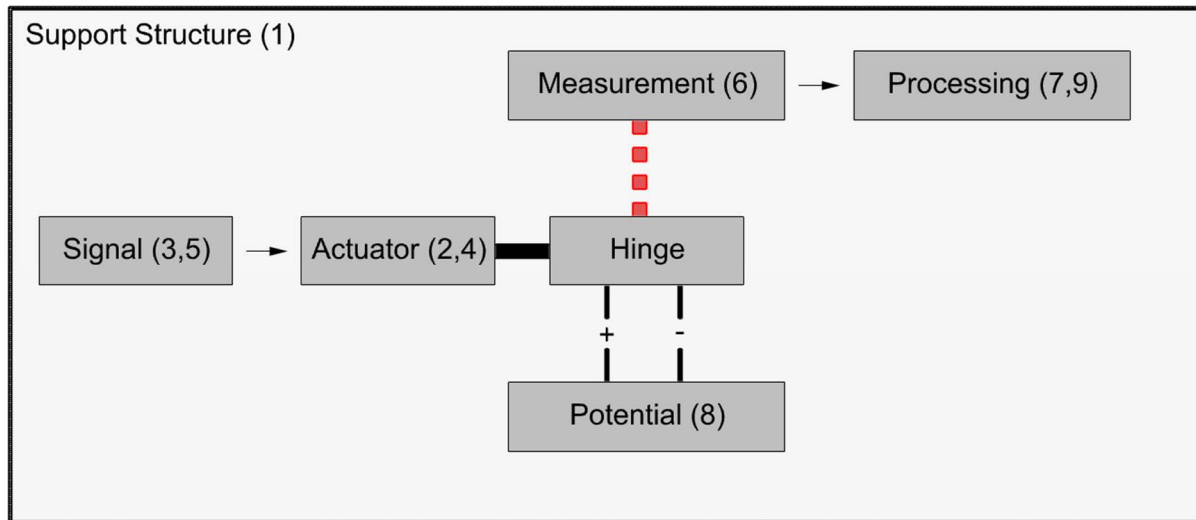


Figure 58: Schematic depiction of the experimental set-up.

- **Support structure:** The set-up needs a skeleton that is strong enough to hold all the components in place, and stiff enough to not influence the measurements.
- **Actuation:** The set-up needs to be able to excite the hinge at a range of frequencies around its first eigenfrequency. For this an actuator is required that can vary between frequencies of 1 to 50 Hz, with a step size of at least 0.1 Hz.
- **Measurement:** The amplitude of the structure will need to be measured at a high accuracy to be able to determine the eigenfrequency as accurately as possible.
- **Processing:** The measurement data needs to be processed into the desired form, in this case a frequency-displacement plot.
- **Apply potential:** A potential needs to be applied to the outer layers of the hinge to activate the piezoelectric material in the sandwich layers.

With the requirements clear we can detail the machinery and components used, which is done in Table 8. The experimental set-up is shown in Figure 59 and is further detailed in Appendix B.

Table 8: Overview of the components used in the experimental set-up.

	Component	Description
#	Support structure	
1	Thorlabs XE25 profiles, breadboard and connecting components [1]	These Thorlabs components were designed with opto-mechanics in mind but are very useful for building various rigid mechanical set-ups. The components are made out of solid aluminium and allow for robust and high stiffness constructions, with high flexibility in positioning due to the built-in rails. Used to build the experiment's support structure.
	Actuation	
2	RS Pro linear solenoid [2]	Lightweight actuator with stroke of up to 13.5 mm and an actuation force of up to 300 gf. Able to follow a signal up

		to 100 Hz (from experimentation). Used to excite the hinge and strip.
3	<i>Tektronix TDS 2024 oscilloscope [3]</i>	A 200 MHz 4-channel scope that can generate a signal to drive the actuator in the required range with a step size of 1/100 <sup>th</sup> of a Hz.
4	<i>Delta Elektronika D5 12VDC</i>	A 5 A 12 V power supply to supply power to the actuator.
5	<i>Custom printed circuit board</i>	A custom printed circuit board that acts as a switch driven by the signal generator.
Measurement		
6	<i>OptoNCDT 1420 smart laser [4]</i>	Triangulation displacement sensor with an accuracy of 8 $\mu\text{m}$ and a measuring rate of 4 kHz. Used to measure the displacement of the strip attached to the hinge.
Processing		
7	<i>National Instruments USB-6008 Multifunction I/O device [5]</i>	A bus-powered multifunction I/O device, used to record the output of the laser and convert it to data to be processed on the computer.
9	<i>Labview by National Instruments [6]</i>	Labview is a graphical programming environment used to develop and validate test systems. Used to process the output of the I/O device.
Apply Potential		
8	<i>Delta Elektronika ES300 [7]</i>	A 300 W DC power supply, allowing for a variable voltage up to 30 V and a variable current up to 10 A. Used to set up a static voltage over the layers of the hinge.
[1] <a href="https://www.thorlabs.com/newgrouppage9.cfm?objectgroup_id=194">https://www.thorlabs.com/newgrouppage9.cfm?objectgroup_id=194</a> [2] <a href="https://docs.rs-online.com/6dff/0900766b8167922c.pdf">https://docs.rs-online.com/6dff/0900766b8167922c.pdf</a> [3] <a href="https://w140.com/tekwiki/wiki/tds2024">https://w140.com/tekwiki/wiki/tds2024</a> [4] <a href="https://www.micro-epsilon.com/displacement-position-sensors/laser-sensor/optoncdt_1420_basic/?slang=en">https://www.micro-epsilon.com/displacement-position-sensors/laser-sensor/optoncdt_1420_basic/?slang=en</a> [5] <a href="https://www.apexwaves.com/modular-systems/national-instruments/usb-multifunction-devices/usb-6008?gclid=cj0kcqia6fafbhc1arisaiijl8kcvttpekqh3bnzhcmx_s94jktpkbemqi1uj0uk5udjdqwhndvhjo0aagfoealw_wcb">https://www.apexwaves.com/modular-systems/national-instruments/usb-multifunction-devices/usb-6008?gclid=cj0kcqia6fafbhc1arisaiijl8kcvttpekqh3bnzhcmx_s94jktpkbemqi1uj0uk5udjdqwhndvhjo0aagfoealw_wcb</a> [6] <a href="https://www.ni.com/nl-nl/shop/labview.html#pinned-nav-section2">https://www.ni.com/nl-nl/shop/labview.html#pinned-nav-section2</a> [7] <a href="https://delta-elektronika.nl/products/es300">https://delta-elektronika.nl/products/es300</a>		

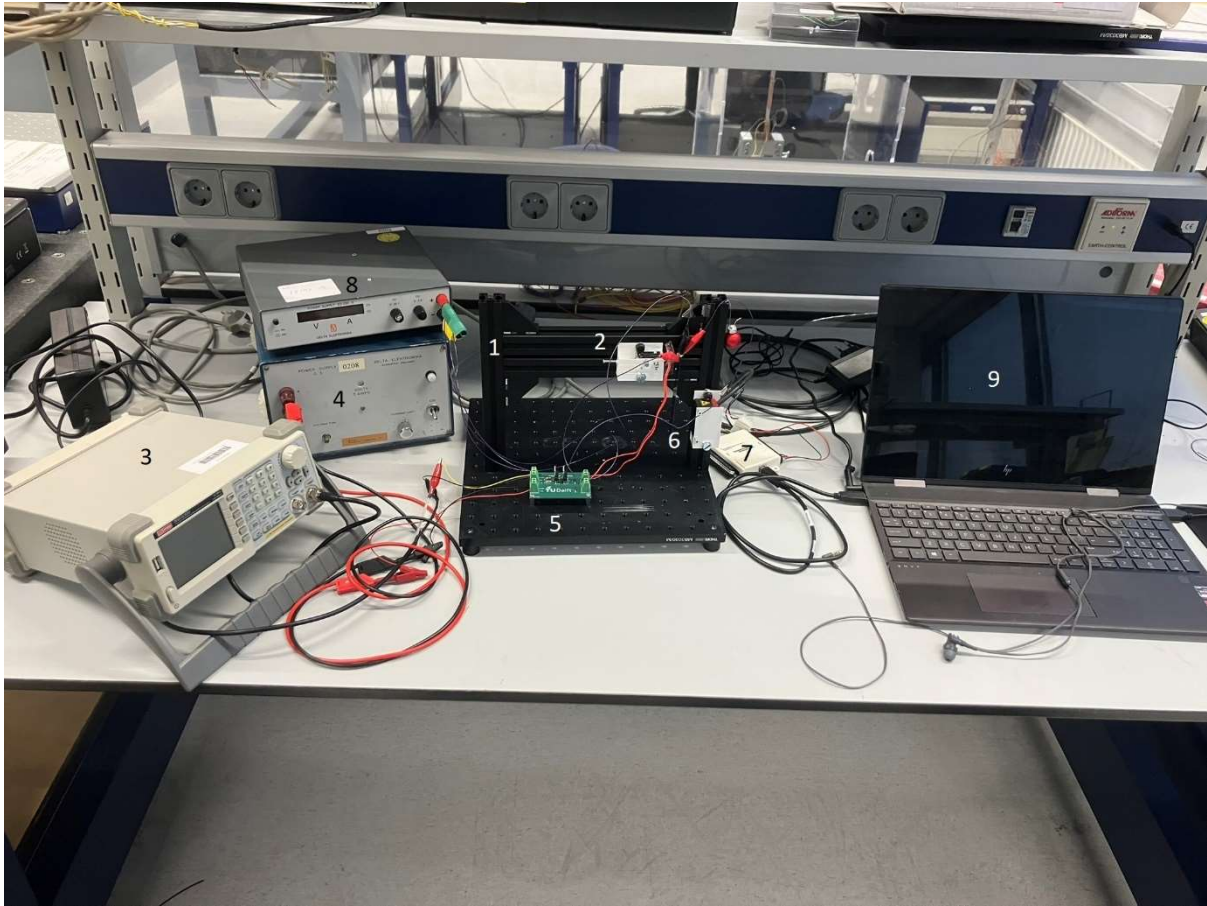


Figure 59: Experimental set-up with different parts numbered.

## 5.4 Results

With the set-up ready it is time to start measuring. The first subsection will detail how the measured data is processed. Next, three different prototypes were tested. The results for each one are discussed in their own subsection. It is important to note that in the end the experiment is executed using a 30 V maximum instead of 50 V, as will be mentioned in the discussion. The new predicted eigenfrequency values for the numerical model using a strip of length  $10 \cdot L$  are shown in Table 9.

Table 9: Eigenfrequency values for a 30 V set-up.

Length strip = 10 · Length hinge at 30 V			
Eigenfrequency [Hz]	0 V	30 V	Difference
<b>First</b>	3.3951	3.4441	1.44%
<b>Second</b>	22.807	22.861	0.24%

### 5.4.1 Measurement Processing

The process for each prototype is the same. It starts off with a measurement from 1 to 9 Hz with steps of 0.2 Hz. Eight seconds of data is measured for each step, which, with a measuring rate of 10 Hz, totals 80 data points for each step. The data is transformed in a 3-step process, illustrated in Figure 60. First, the average value of all the data points is calculated and added to the data points to center the data around zero. Next, the absolute value of the data is taken to mirror the data in the negative space onto the positive space. And finally, the average value of the transformed data is taken for each frequency step, to give an indication of the average magnitude of the displacement. The reason the absolute value is taken to mirror the data in the negative space onto the positive space is twofold. Just removing it reduces the

number of data processed per step, and due to the hinge manufacturing process not being perfect the displacement curve is often not symmetric around the average value.

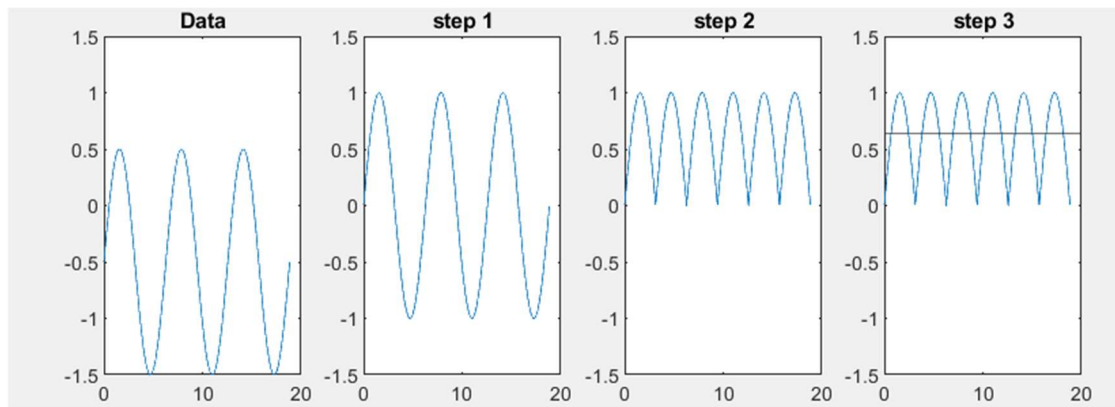


Figure 60: Illustration of data process.

The data from the first measurement is used to locate the first eigenfrequency of the structure. Differences in the hinges and strips due to assembly and gluing pieces together make these eigenfrequencies differ significantly so they have to be determined for each hinge. Once the eigenfrequency is located five measurement runs are executed in a frequency range around the eigenfrequency. For the first two prototypes these ranges were 2 Hz in length with steps of 0.2 Hz, and for the third prototype the range is only 1 Hz in length with steps of 0.1 Hz. The reason for this difference is that the third prototype was the first to be measured, and after the measurements were done, the decision was made to increase the size of the range to allow for more datapoints on the part of the trendline with the largest gradient, instead of just around the top of the trendline. However due to the way the experiment is set-up once a hinge is removed from the set-up it is usually too damaged to be used for measuring again.

The same data processing discussed earlier and illustrated in Figure 60 is applied to the datapoints from the five measurement runs, and the averaged values for each frequency are plotted together in a scatter plot. A polynomial trendline is then fitted to the data and is used to determine the x-value of the peak, representing the eigenfrequency. This x-value is used to calculate the peak's y-value, representing the average deflection. The calculation detailed in Section 5.2 is then used to determine the stiffness of the hinge. For the Prototypes 2 and 3 a polynomial trendline of order 2 is used. This quadratic polynomial is symmetric to the left and right of its peak, similar to how an ideal frequency-displacement plot should show a symmetric peak at the eigenfrequency. For prototype 1 a polynomial of order 3 is used, since it provided a better fit for the data due to the start of a second peak falling in the frequency range. The results for each prototype are discussed in the following subsections.

#### 5.4.2 Prototype 1

Prototype 1 is measured in a range from 3 to 5 Hz. The results are shown in Figure 61, and the numerical values are given in Table 10.

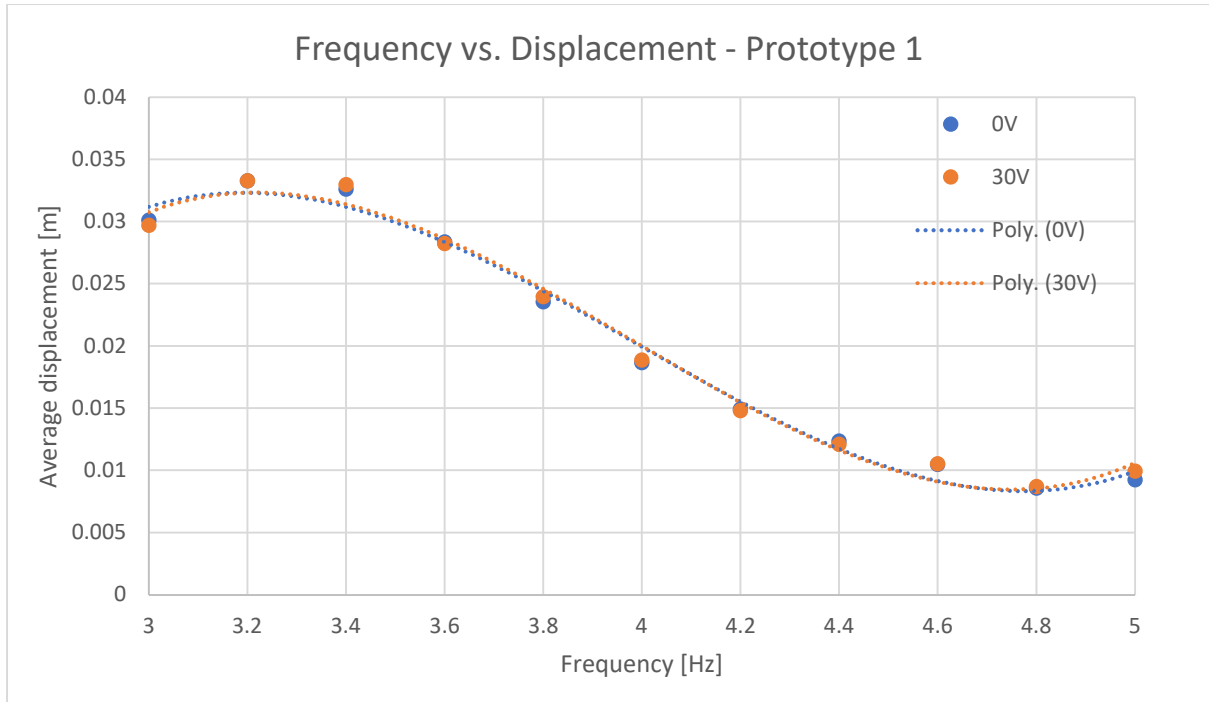


Figure 61: Frequency vs Displacement for Prototype 1.

Table 10: Numerical values for Prototype 1.

Prototype 1	0 V	30 V	Difference
<b>Eigenfrequency <math>\omega</math> [Hz]</b>	3.1967	3.2148	0.566 %
<b>Average deflection <math>w_{max}</math> [m]</b>	0.03270	0.03190	-2.45%
<b>Hinge stiffness <math>k_h</math> [m]</b>	10.31	10.43	1.15%

The eigenfrequency is close to the predicted eigenfrequency, but the difference in eigenfrequency when a potential is applied is significantly lower than the numerical model predicts. Another interesting thing to note is that the difference in average deflection is larger than the difference in stiffness. Formula 5-1 from Subsection 5.1.1 relates the deflection linearly to the stiffness; however, this is only the case in a situation where the deflection is measured in the same location the force is applied. In the case of this experiment, the hinge is excited at its fixed end and the deflection is measured about halfway of the added strip, which means this relation no longer applies. However, for the 0.5% lift threshold a hinge stiffness change of 5.15% was calculated, which this prototype does not achieve.

### 5.4.3 Prototype 2

Prototype 2 is measured in a range from 5 to 7 Hz. The results are shown in Figure 62, and the numerical values are given in Table 11.

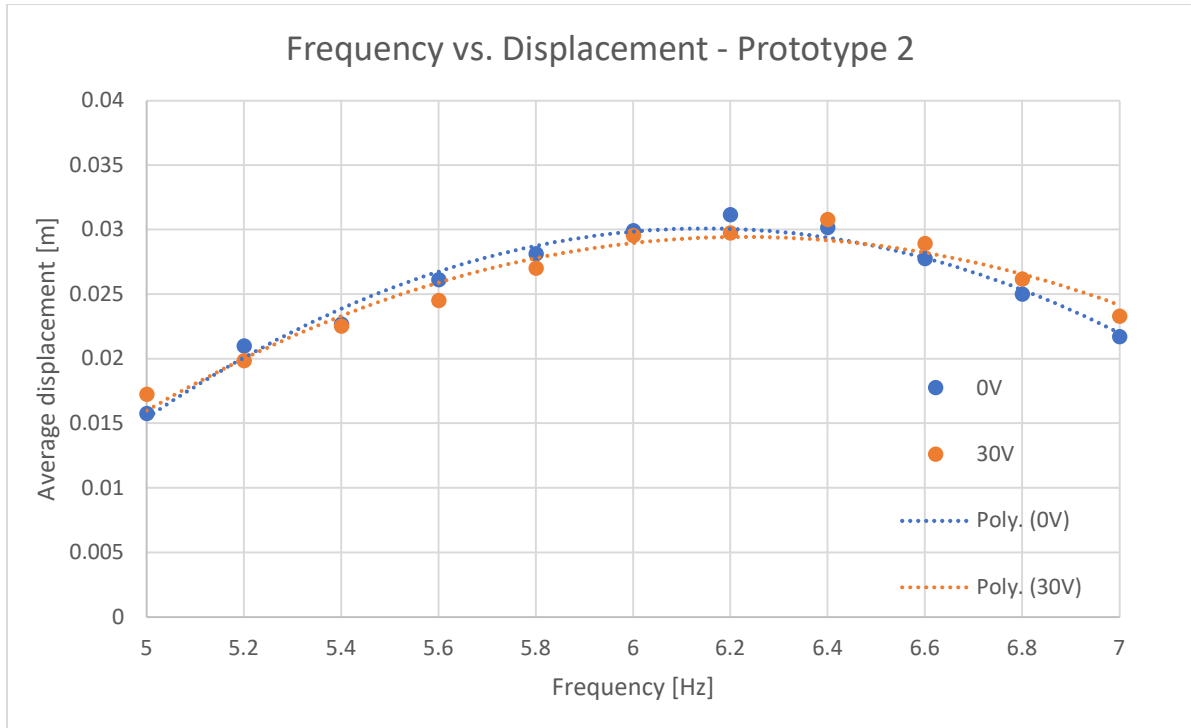


Figure 62: Frequency vs Displacement for Prototype 2.

Table 11: Numerical values for Prototype 2.

Prototype 2	0 V	30 V	Difference
Eigenfrequency $\omega$ [Hz]	6.176	6.225	0.79%
Average deflection $w_{max}$ [m]	0.03214	0.02915	-9.31%
Hinge stiffness $k_h$ [m]	39.45	40.10	1.65%

The eigenfrequency for this prototype is significantly higher, which could be due to faults in the assembly or because the eigenfrequency measurement picked up the second harmonic. However, despite of this discrepancy, this prototype shows the best results. The change in eigenfrequency is still not as high as the numerical model predicts but it does show a significant change in average deflection. The hinge stiffness still does not come near its intended goal of 5.15% but the deflection difference indicates that the design may still have some potential if perhaps analyzed through a different metric.

#### 5.4.4 Prototype 3

Prototype 3 is measured in a range from 3.5 to 4.5 Hz. The results are shown in Figure 63, and the numerical values are given in Table 12.

Table 12: Numerical values for Prototype 3.

Prototype 2	0 V	30 V	Difference
Eigenfrequency $\omega$ [Hz]	3.993	4.001	0.19%
Average deflection $w_{max}$ [m]	0.05640	0.05640	0.00%
Hinge stiffness $k_h$ [m]	16.17	16.24	0.40%

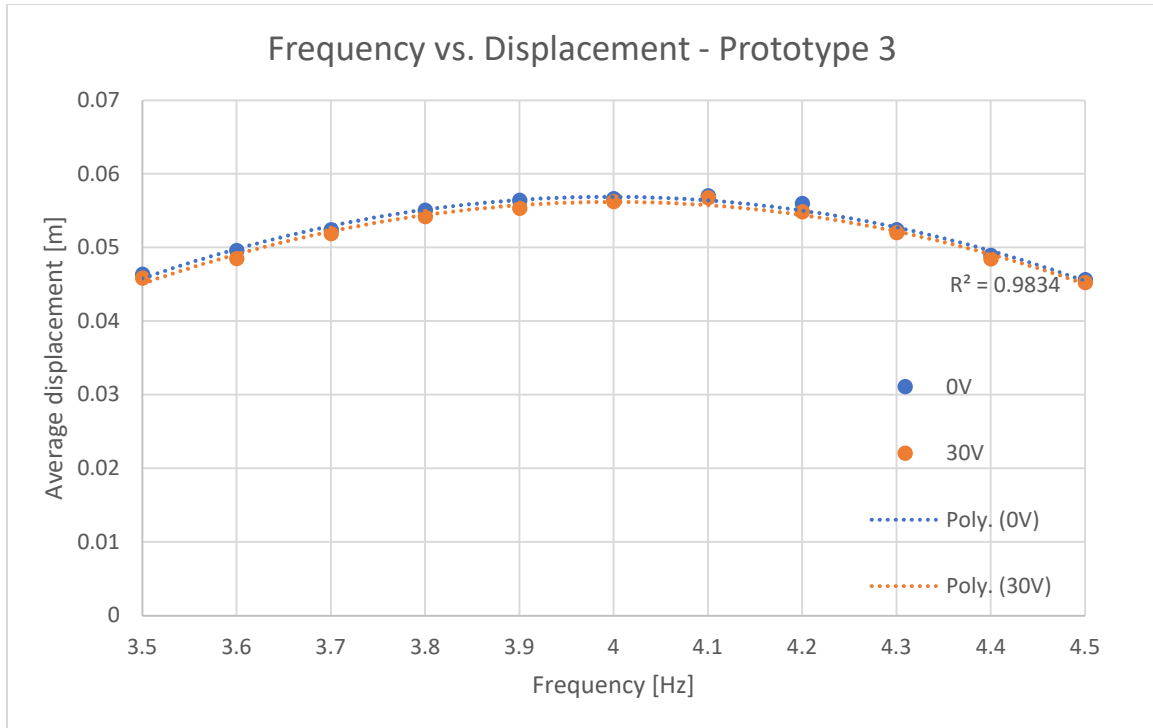


Figure 63: Frequency vs Displacement for Prototype 3.

This prototype is the worst performing prototype. It does still show a change in eigenfrequency though it is significantly smaller than the previous prototypes, and it displays no change in average deflection at all. Due to the small nature of the prototype, it is hard to say what exactly made this prototype less effective than the other two, but since the dimensions are the same as the other hinges the problem is sure to lie in the assembly process.

#### 5.4.5 Validation

The results in the previous sections seem to indicate that while none of the prototypes achieve the stiffness threshold, all of them show a measurable effectiveness. This section will briefly analyze whether this effectiveness could just be a statistical error. Before looking at the data itself we first check the  $R^2$  values of the polynomial trendlines fitted to the data. These are shown in Table 13.

Table 13:  $R^2$  values for the trendlines.

Prototype #	$R^2$ value for 0 V	$R^2$ value for 30 V
Prototype 1	0.990	0.990
Prototype 2	0.977	0.952
Prototype 3	0.986	0.983

The  $R^2$  value measures the strength of the relationship between the data and the model. A high  $R^2$  value usually indicates that the model fits the data well. In the case of the trendlines here, all  $R^2$  values are above 95%, with the values for Prototypes 1 and 3 being above 98%.

These high values indicate a good correlation between the data and the trendline, however, they are not conclusive. To look at the data through a different perspective, we will also perform an error estimate for the data. Equation 5-14 shows the formula for the error estimation of a mean.

$$\Delta \bar{x} = \frac{\sigma}{\sqrt{n-1}} \quad (5-14)$$

Here  $\sigma$  is the standard deviation and  $n$  is the number of datapoints, which is 4400 for each prototype. Performing this error estimate on the data for the average displacement gives the following results.

Table 14: Error estimates for the mean of the average displacement.

Prototype #	Error of the mean	Difference in means found in the experiment
Prototype 1	1.17%	-2.45%
Prototype 2	0.699%	-9.31%
Prototype 3	0.709%	0.00%

Table 14 shows that the results found for Prototypes 1 and 2 are significant, and only the results found for Prototype 3 are possibly statistical errors. With Prototype 3 being the least effective prototype, where a difference in average displacement of 0% was found this is no surprise.

## 5.5 Conclusions

To recap, the differences in physical characteristics of the three prototypes are shown in Table 13.

Table 15: Recap of experiment results.

Prototype #	Eigenfrequency	Average deflection	Hinge stiffness
Prototype 1	0.57%	-2.45%	1.15%
Prototype 2	0.79%	-9.31%	1.65%
Prototype 3	0.19%	0.00%	0.40%

Looking at the 5.15% stiffness change requirement, none of the prototypes are successful. However, the first and especially the second prototype show a significant reduction in average deflection. While no longer in the scope of this research, it is interesting to find a more well-defined threshold for the deflection at different points on the hinge and wing, and see if according to this new criterion the hinge design might have a high enough effectiveness.

## 6. Discussion

The presented research shows quite a journey, from basic analytical models to a finalized design and an experimental set-up. All choices and decisions made have as been based on previous research and established theory as well as possible. However, no research is executed perfectly, and this research is no exception. This chapter aims to place the findings of the research into context, and look at unexpected results and weaknesses.

Section 6.1 quickly summarizes the key findings of the research, and contextualizes them by relating them to previous research. Section 6.2 mentions the unexpected results found in the process, and addresses the weaknesses and limitations of the research. Finally, Section 6.3 shortly talks about the implications of the key findings.

### 6.1 Key Findings

Throughout the research different models have generated different results, so this chapter starts off with a quick timeline of the findings.

- 1) The analytical models showed the potential of the stiffness-based materials and methods, flaunting a potential 160% to 2500% change in stiffness theoretically possible for a hinge of standard dimensions. However, it also noted the low performance of the damping method, showing that a 1500% damping increase for the entire wing would be required to achieve the set lift threshold. The subsequent damping model predicted a damping increase in the hinge to require many times even the most optimistic theoretical values before even being close to start influencing the wing movement.
- 2) The numerical models showed a more similar picture at first, with the most successful piezoelectric material design able to achieve a 3500% change in stiffness, but as the design iterations furthered the potential effectiveness dropped, with the change from PZT to PVDF as piezoelectric material and the reduction of the maximum potential voltage from 500 V to 50 V causing large drops in the design's effectiveness. However, the finalized design still shows a stiffness change of slightly over 20% for the maximum voltage, meaning the effectiveness is still high enough to reach the set threshold for change in lift.
- 3) The experiment showed that the prototypes produced using the current assembly process do not live up to the numerical models. However, due to an unexpectedly large change in average deflection in the second prototype, the potential of the hinge is not fully extinguished.

Table 14 shows the effectiveness for the major design iterations throughout the entire research.

Table 16: Effectiveness of the different design iterations throughout the research.

Design iteration	Effectiveness
Analytical model	250%
Original piezoelectric design	650%
Iteration 1 (variation 1)	90%
Iteration 2 (variation 2)	3500%
Reduction of maximal voltage	500%
Switch to PVDF	100.9%
Finalized design	121%
Experiment design (Numerical simulation)	102.94% (based on eigenfrequency) 111.74% (based on deflection)

**Experiment design (Experimental findings)**

101.65% (based on eigenfrequency)

109.69% (based on deflection)

To put these results into context, we look at four previously performed research projects with a similar nature.

1) Research done on a Stick-slip hinge was done by Wang (Wang, 2017), and has been mentioned multiple times throughout this report. On top of this, Wang's model was the foundation for the analytical determination of the required thresholds for stiffness and damping. Wang also experimented on a wing hinge based on the Stick-slip method, results of which were previously showed in Figure 27, and are shown here again.

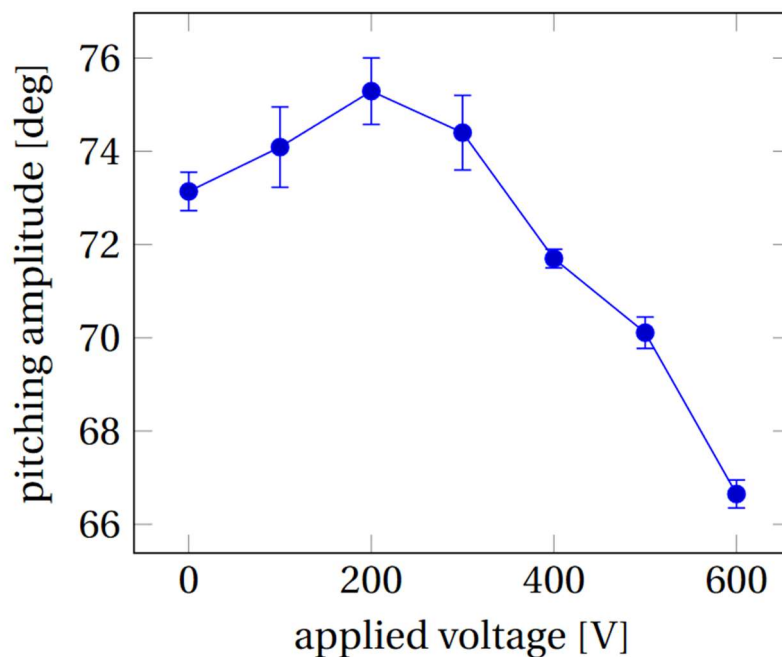


Figure 64: Repeat of Figure 27, showing pitching amplitude of the wing plotted versus the applied voltage. Image from (Wang, 2017).

Based on this figure, for a voltage of 50 V a change in angle of about 1° is achieved. We can estimate the change in stiffness using Equation 6-1 (Tinjum, 2011).

$$k_{rot} = \frac{M}{\theta}. \quad (6-1)$$

Assuming the applied moment  $M$  stays the same, the change in angle  $\theta$  gives a change in rotational stiffness of about 1.4%. Higher voltages did show a potential rotational stiffness change of about 8.2%.

2) Another research project on a Stick-slip method hinge was executed in (Drexhage, 2014), of which the results are shown in Figure 65. Although the graph is a bit hard to read, we can confidently say that this experiment showed a change in stiffness of less than 2.5% for a voltage up to 50 V. Again, higher voltage did show a higher potential change in stiffness, up to about 35%.

3) A research project on a passively damped hinge was performed in (Lu, 2013). Experimental testing revealed an effectiveness of 1.4% using a ceramic piezoelectric material in the form of PZT, and PVDF showing an effectiveness of less than 0.2%.

4) Finally, another research project on a variable stiffness hinge in the form of a beam with attached piezoelectric material described in (Sapin, 2013). This research concluded a 3.5% change in stiffness for a potential up to 50 V, and a maximal potential change in stiffness of a little closer to 4% at a voltage of about 60 V.

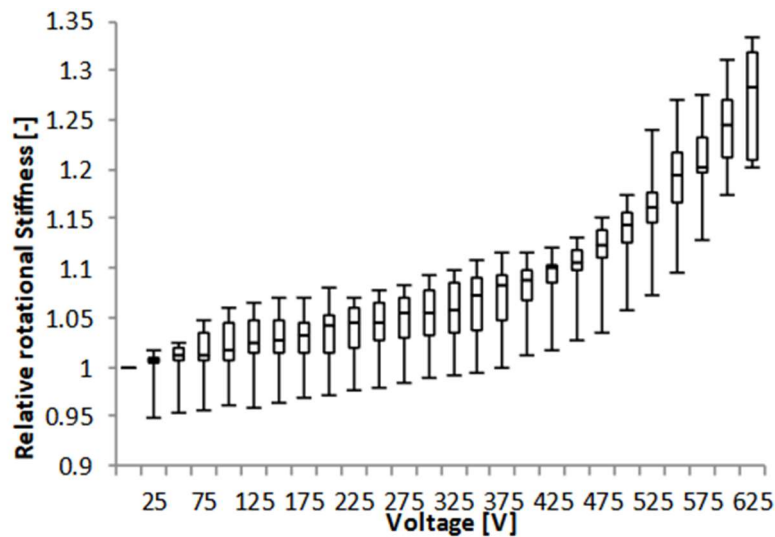


Figure 65: Voltage plotted versus relative stiffness in the research of (Drexhage, 2014).

The maximal theoretical change in stiffness this research found was 21% as shown in Table 14 for the finalized design. This value is significantly higher than most of the previously mentioned results from different research projects, although still smaller than the 35% change found in (Drexhage, 2014). The experimental results in this research showed a 9.69% effectiveness based on the deflection, and a 1.65% based on eigenfrequency. These numbers are a lot closer to the numbers in the previously mentioned research, and match the trend where research with an experimental set-up tend to show a smaller effectiveness due to the difference between numerical models and experimental validation. It is also important to mention that the used maximum electric potential of 30 V is a lot lower than some of the previously mentioned research project, which adds to the potential of the design for integration in the Atalanta design.

## 6.2 Unexpected Results and Research Limitations

This section discusses the weaknesses of the research by looking at the unexpected results and limitations of the research. The findings in this section are meant both as criticism of the research itself, and suggestions for future research. The recommendations in Chapter 7 will elaborate on some of the limitations mentioned here.

### 6.2.1 Unexpected Results

The first result that is unexpected is the large order difference between the internal damping moment of a cantilever beam and the actuation moment acting on the wing, discussed in Section 2.3. An order of difference of  $10^{12}$  seems almost too large to be correct. However, a number of factors do seem to indicate that the internal damping of the beam could be considered at the very least negligible. The ASTM International Standard (ASTM, 2017) recommends using a loss factor of zero for metal beams due to their low loss factor compared to other materials such as composites, and research by Mevada seems to support this with an experimentally determined damping factor of less than 0.007 for a mild steel cantilever beam (Mevada, 2016). On top of this the calculation in Section 2.3 only takes into account the internal damping of the beam, not the aerodynamic damping. This decision is made for two reasons, the

primary reason being that the use of smart fluids would not influence the aerodynamic damping. The second reason is that, as mentioned in Section 2.3, the aerodynamic damping of the hinge is significantly smaller than that of the wing, meaning it will barely influence the wing motion. Therefore, even though the result of the calculation is lower than expected, it is assumed that the internal damping moment of the beam is negligible compared to the other moments that dictate the wing movement.

The second unexpected result is the low deflection for the finalized and experiment design. Due to the nature of the research question, the focus throughout the research is on the change in stiffness, not the absolute stiffness value. This caused the low deflection values to not be discovered until the experiment was thought out. For a hinge that is supposed to undergo large deformations, a deflection change of a few hundred nanometers does not seem sufficient, even if the change in stiffness seems to reach the set threshold. The experiment found a relatively large change in deflection however, although this was in the case of a dynamic measurement, which included an attached strip to increase the deflection.

### 6.2.2 Research Limitations

The first limitation of the research is the damping model simply considering a metal beam with internal damping, causing a low effectiveness of the damping method. A more specific design that maximizes damping potential could achieve significantly higher results. For instance, a rotary damper design (Tse, 2014) could be used. The main problem with the damping devices based on smart fluids is that barely any of them are on a scale that fits within the Atalanta project (Liu, 2015). On small scales the preferred materials seem to be shape-memory alloys and piezoelectric materials (Choudhary, 2015). However, regardless of the material, the analytical calculations could still be modified to better represent more detailed damping designs. In a similar vein, the cross-section expansion designs were discarded due to their deformation at the free end making it hard to attach the wing. However, with different boundary conditions perhaps these designs could properly work within the Atalanta project. For instance, a design inspired by (Walsh, 1992), consisting of two leaf spring between which the distance is increased.

The second limitation of the research is the inability to numerically model the Stick-slip method. Section 3.3 already touched on this and mentioned that while in literature COMSOL is used to model Stick-slip behavior (Jalili, 2018 & Zhang, 2021), these models involve only a small number of contact points. So, one option could be to model the design in COMSOL using less contact points, but it is hard to make sure the findings would be relevant for a surface-on-surface case. Another option is to consider a more in-depth analytical model of the Stick-slip phenomenon, such as discussed in (Awrejcewicz, 2007). Similar suggestions go for the modelling of a honeycomb structure material to facilitate cross-section expansion, since these materials are not implemented in COMSOL yet. The uniform increase in volume could be modelled using for instance thermal expansion, however it would again be hard to make sure the acquired results would be realistic.

The third limitation is the absence of a systemic approach to design variations in Chapter 3. Most of the variations are based on engineering intuition and estimated guesses. Some design variations are not pursued further due to a lack of time and resources or an inability to properly model them. Based on a proper design approach as detailed in (Childs, 2003), the *analysis* step can be improved. Setting up a robust theory can help predict which design variations will be more successful and can support a more systematic approach to varying the design to provide more optimized results. Furthermore, more evaluation can be implemented in the design process, for instance testing the variations not only on their static displacement but also on their dynamic displacements or their eigenfrequency responses.

The fourth limitation of the research is the 30 V limit to the voltage applied to the hinge in the experiment. Subsection 4.2.2 details the choice for reducing the voltage in the numerical models to 50 V,

with the intention of using this limit in the experiment as well. However, due to time constraints and lab safety reasons it was later decided to stick to a maximum voltage of 30 V. Since commercial step-up DC-DC converters are limited at 35 V this does make the experiment results more realistic, but it also reduces the significance of the results and therefore their reliability.

The final limitation of the research is the limited frequency range used in the experiment. To properly fit a trendline to data more datapoints are always useful, but especially the datapoints away from the peak, there where the gradient of the fitted curve is largest, can improve the accuracy of the results. Although, as discussed in Subsection 5.4.5, the  $R^2$  values for the trendline are fairly high, increasing the frequency range would probably still have increased the quality of the results, especially for Prototypes 2 and 3. These prototypes feature data mostly centered around their eigenfrequency peak.

It is also important to quickly mention that according to Table 14, the experiment design already did not achieve the 5.15% stiffness threshold based on eigenfrequency. This is an oversight that was discovered later on in the research, when the experiment was already in progress.

### 6.3 Research Implications

Even though the research has its unexpected results and limitations, it has also produced some relevant findings for the Atalanta project. Here some of the key findings are restated, and their implications are mentioned.

Firstly, the analytical model ruling out damping methods for the cantilever beam hinge concept allows the focus of the research towards stiffness methods. Previous research within the Atalanta project never really focused on damping methods, even though they are mentioned by the likes of Peters (Peters, 2016). The findings of this research show that for a cantilever beam design a method based on increase of internal damping would require unrealistic amounts of damping increase to be effective.

Secondly, even though the final design proved experimentally to not be effective enough, the numerical model still shows a potential of reaching the 5.15% stiffness change threshold. Improvements on manufacturing or a deeper analysis on the design could optimize it, and might possibly lead to a working design based on the same principle as the design discussed in this research.

Finally, the experiment shows that the prototypes do not achieve the effectiveness promised by the numerical model, in a measure based on the eigenfrequency. However, based on the average deflection, one of the prototypes shows an unexpected potential, reducing the average deflection by 9.31%.

Since the scope of this research is finite, all the findings mentioned in this chapter to improve the research are left as recommendations to future researchers. The Recommendations in Chapter 7 briefly mentions the improvements discussed in this chapter.

## 7. Conclusions and Recommendations

---

This research set out to design and test a controllable hinge for achieving control in a FWMAV. Through the use of analytical models, it was found that hinge designs based on a change in stiffness were the most promising, and a numerical threshold for effectiveness was set. Numerical modelling was used to finalize a design which could achieve a high enough effectiveness and could theoretically be implemented in the Atalanta design. The design uses a PVDF film sandwiched between spring steel layers attached using adhesive film. An experiment was carried out to test the design, which found that while a change in stiffness could be measured, the design did not reach the effectiveness threshold...

The research is limited in its exploration of designs based on a change in damping. Additionally, assembly and testing of the prototypes can be improved. However, the research shows a theoretical potential for the design, which is lightweight and uses a relatively low voltage.

To further build on this research, a number of things could be done:

- In-depth research on a hinge design build around maximizing internal damping through the use of smart fluids.
- Improvements to the numerical models that allow for the modelling of the Stick-slip method and honeycomb materials.
- Developing a systematic approach to optimize the current design or one of its variations. This could include a more robust methodology but could also implement techniques like topology optimization. Research could also be done into how to better use the materials, for instance using electrode coated PVDF films.
- An improved experimental set-up featuring different testing methodologies and higher voltages.
- Setting up a well-defined criterion for a threshold in reduction in deflection, since especially Prototype 2 shows an unexpected potential in this category.

## References

---

- 3M, 2023. 3M™ Adhesive Transfer Tape Double Lined 8132LE. [https://www.3m.com/3M/en\\_US/p/d/b40065942/](https://www.3m.com/3M/en_US/p/d/b40065942/)
- Andersen, A., Pesavento, U. & Wang, Z. J., 2005. Unsteady aerodynamics of fluttering and tumbling plates. *Journal of Fluid Mechanics*, 541, 65–90.
- Anton, S.R., Erturk, A. and Inman, D.J., 2012. Bending strength of piezoelectric ceramics and single crystals for multifunctional load-bearing applications. *IEEE transactions on ultrasonics, ferroelectrics, and frequency control*, 59(6), pp.1085-1092.
- Arkema, 2023. Technical Guide Piezotech RT-TS. <https://page.arkema.com/rs/253-HSZ-754/images/Technical%20Guide%20Piezotech%20RT-TS.pdf>
- ASTM, 2017. Standard Test Method for Measuring Vibration-Damping Properties of Materials. <https://compass.astm.org/document/?contentCode=ASTM%7CE0756-05R17%7Cen-US&proxycl=https%3A%2F%2Fsecure.astm.org&fromLogin=true>
- Awrejcewicz, J. and Olejnik, P., 2007. Occurrence of stick-slip phenomenon. *Journal of Theoretical and Applied Mechanics*, 45(1), pp.33-40.
- Badescu, M., Sherrit, S., Bao, X., Aldrich, J., Bar-Cohen, Y. and Jones, C., 2008. Extended life PZT stack test fixture. In *Behavior and Mechanics of Multifunctional and Composite Materials 2008* (Vol. 6929, pp. 15-21). SPIE.
- Banerjee, J.R., 2012. Free vibration of beams carrying spring-mass systems– A dynamic stiffness approach. *Computers & structures*, 104, pp.21-26.
- Banks, H.T. and Inman, D.J., 1991. On damping mechanisms in beams.
- Bergamini, A., Christen, R., Maag, B. and Motavalli, M., 2006. A sandwich beam with electrostatically tunable bending stiffness. *Smart materials and structures*, 15(3), p.678.
- Bolsman, C. T., 2010. Flapping-wing actuation using resonant compliant mechanisms. PhD thesis, <https://repository.tudelft.nl/islandora/object/uuid%3A9c277bea-9b50-4ba4-82c5-09083ffe053a?collection=research>
- Bonnecaze, R.T. and Brady, J.F., 1992. Dynamic simulation of an electrorheological fluid. *The Journal of chemical physics*, 96(3), pp.2183-2202.
- Chen, C., Liu, M. and Wang, Y., 2018. A dual stage low power converter driving for piezoelectric actuator applied in micro mobile robot. *Applied Sciences*, 8(9), p.1666.
- Childs, T.H.C., 2003. *Mechanical design*. Elsevier.
- Choudhary, N. and Kaur, D., 2015. Vibration damping materials and their applications in nano/micro-electro-mechanical systems: a review. *Journal of Nanoscience and Nanotechnology*, 15(3), pp.1907-1924.
- Components101, 2023. XL6009 DC Behaviour Step Down Voltage Regulator Module. <https://components101.com/modules/xl6009-dc-dc-step-down-voltage-regulator-module>
- COMSOL, 2018. Eigenfrequency Analysis. <https://www.comsol.com/multiphysics/eigenfrequency-analysis>

- Cordero, F., 2018. Quantitative evaluation of the piezoelectric response of unpoled ferroelectric ceramics from elastic and dielectric measurements: Tetragonal BaTiO<sub>3</sub>. *Journal of Applied Physics*, 123(9), p.094103.
- De Croon, G.C.H.E., De Clercq, K.M.E., Ruijsink, R., Remes, B. and De Wagter, C., 2009. Design, aerodynamics, and vision-based control of the Delfly. *International Journal of Micro Air Vehicles*, 1(2), pp.71-97.
- Desai, A., 2008. Size effect on the mechanical properties in zinc oxide. The Pennsylvania State University.
- Drexhage, T. H., Nelissen, W. E. D., Hoogerbrugge, A. J., Kapelle, D., 2014. Controlling the bending stiffness of a cantilever hinge. BsC Thesis
- Diekerhof, R., 2016. Resonating structures with flapping wings. MSc Thesis
- Dudley, R., 2002. *The biomechanics of insect flight: form, function, evolution*. Princeton University Press
- Eichhorn, C., Tchagsim, R., Wilhelm, N. and Woias, P., 2011. A smart and self-sufficient frequency tunable vibration energy harvester. *Journal of Micromechanics and Microengineering*, 21(10), p.104003.
- Electronicavoorjou, 2023. MT3608 Step Up. <https://elektronicavoorjou.nl/en/product/mt3608-step-up/>
- Ellington, C. P., 1984. The aerodynamics of hovering insect flight. IV. Aerodynamic mechanisms. *Philosophical Transactions of the Royal Society B: Biological Sciences*, 305 (1122), p. 79–113.
- Elshamy, M., Crosby, W.A. and Elhadary, M., 2018. Crack detection of cantilever beam by natural frequency tracking using experimental and finite element analysis. *Alexandria engineering journal*, 57(4), pp.3755-3766.
- Farrell Helbling, E., and Robert J. Wood, 2018. A review of propulsion, power, and control architectures for insect-scale flapping-wing vehicles. *Applied Mechanics Reviews*, 70.1
- Floreano, Dario, and Robert J. Wood., 2015. Science, technology and the future of small autonomous drones. *Nature*, 521.7553, p. 460-466.
- Greenewalt, Crawford H., 1960. The wings of insects and birds as mechanical oscillators. *Proceedings of the American Philosophical Society*, 104.6, p. 605-611.
- Gururaja, T.R., Schulze, W.A., Cross, L.E., Newnham, R.E., Auld, B.A. and Wang, Y.J., 1985. Piezoelectric composite materials for ultrasonic transducer applications. Part I: Resonant modes of vibration of PZT rod-polymer composites. *IEEE Trans. Sonics Ultrason*, 32(4), pp.481-498.
- Hassanalain, Mostafa, and Abdessattar Abdelkefi, 2017. Classifications, applications, and design challenges of drones: A review. *Progress in Aerospace Sciences*, 91, p. 99-131.
- Hedley, Carolyn., 2015. The role of precision agriculture for improved nutrient management on farms. *Journal of the Science of Food and Agriculture*, 95.1, p. 12-19.
- Henke, M. and Gerlach, G., 2014. On a high-potential variable-stiffness device. *Microsystem technologies*, 20(4), pp.599-606.
- Hines, Lindsey, Domenico Campolo, and Metin Sitti, 2013. Liftoff of a motor-driven, flapping-wing microaerial vehicle capable of resonance. *IEEE Transactions on Robotics*, 30.1, p. 220-232
- Howell, L.L., 2001. *Compliant Mechanisms*. John Wiley & Sons.

- Irvine, T., 2012. Bending Frequencies of Beams, Rods and Pipes, Revision S. <https://www.vibrationdata.com/tutorials2/beam.pdf>
- Jalili, H., Salarieh, H. and Vossoughi, G., 2018. Motion type analysis of a piezoelectric-actuated vibratory micro-robot in hybrid stick-slip-jump mode. *Journal of Sound and Vibration*, 436, pp.81-94.
- Jeveka, 2023. H + S Precisionfoil. <https://jeveka.com/nl/technische-producten/hs-precisiefolie/hs-precisie-folieband>
- JPE Innovations, 2022. Structural Damping Properties of Mechanical Systems. <https://www.jpe-innovations.com/precision-point/structural-damping-properties-mechanical-systems/>
- Kapton, 2023. DuPont Kapton HN. <https://www.dupont.com/products/kapton-hn.html>
- Karásek, Matěj, et al., 2018. A tailless aerial robotic flapper reveals that flies use torque coupling in rapid banked turns. *Science*, 361.6407, p. 1089-1094.
- Kawai, Y., Ono, T., Meyers, E., Gerber, C. and Esashi, M., 2006, January. Piezoelectric actuator integrated cantilever with tunable spring constant for atom probe. In *19th IEEE International Conference on Micro Electro Mechanical Systems* (pp. 778-781). IEEE.
- Kawamura, S., Yamamoto, T., Ishida, D., Ogata, T., Nakayama, Y., Tabata, O. and Sugiyama, S., 2002, May. Development of passive elements with variable mechanical impedance for wearable robots. In *Proceedings 2002 IEEE International Conference on Robotics and Automation (Cat. No. 02CH37292)* (Vol. 1, pp. 248-253). IEEE.
- Kim, S., Patra, A., Kohlmeyer, R.R., Jo, S., Yue, X., Johnson, A., Kiggins, C.T., Zahiri, B., Jeong, K., Koo, J. and Kang, T., 2023. Serially integrated high-voltage and high power miniature batteries. *Cell Reports Physical Science*, 4(1).
- Kindervater, Katharine Hall., 2016. The emergence of lethal surveillance: Watching and killing in the history of drone technology. *Security Dialogue*, 47.3, p. 223-238.
- Korth Kristalle, 2022. Lithium Niobate. <https://www.korth.de/en/materials/detail/Lithium%20Niobate>
- Liao, Y. and Sodano, H.A., 2012. Optimal placement of piezoelectric material on a cantilever beam for maximum piezoelectric damping and power harvesting efficiency. *Smart materials and structures*, 21(10), p.105014.
- Lin, Jih-Lung, Chin-Yi Wei, and Chi-Yu Lin., 2007. Design and testing of fixed-wing MAVs. *Aircraft Engineering and Aerospace Technology*.
- Ling, Geoffrey, and Nicole Draghi., 2019. Aerial drones for blood delivery. *Transfusion*, 59.S2, p. 1608-1611.
- Liu, C., Jing, X., Daley, S. and Li, F., 2015. Recent advances in micro-vibration isolation. *Mechanical Systems and Signal Processing*, 56, pp.55-80.
- Liu, Hao, et al., 2016. Biomechanics and biomimetics in insect-inspired flight systems. *Philosophical Transactions of the Royal Society B: Biological Sciences*, 371.1704, p. 20150390.
- Lu, Y., 2013. Structural control method research motivated for MAV lift force Modification. Master Thesis
- Majidi, C. and Wood, R.J., 2010. Tunable elastic stiffness with microconfined magnetorheological domains at low magnetic field. *Applied Physics Letters*, 97(16), p.164104.

- Megahed, S.M. and Nada, A.A., 2003, January. Dynamic modeling of a flexible cantilever beam: An experimental technique. In *International Design Engineering Technical Conferences and Computers and Information in Engineering Conference* (Vol. 37033, pp. 449-455).
- Mevada, H. and Patel, D., 2016. Experimental determination of structural damping of different materials. *Procedia Engineering*, 144, pp.110-115.
- Micro-Epsilon, 2023. OptoNCDT Laser Displacement Sensors Data Sheet. <https://www.micro-epsilon.com/download/products/cat-optoncdt/dax--optoNCDT-1420--en.html#page=2&zoom=Fit>
- Murayama, Y. and Omata, S., 2004. Fabrication of micro tactile sensor for the measurement of micro-scale local elasticity. *Sensors and Actuators A: Physical*, 109(3), pp.202-207.
- Murray, G., Gandhi, F. and Kang, S.G., 2009. Flexural stiffness control of multilayered beams. *AIAA journal*, 47(3), pp.757-766.
- Myung, N., Wang, L. and Choi, N.S., 2021. High-cycle and very high-cycle bending fatigue strength of shot peened spring steel. *Journal of Mechanical Science and Technology*, 35, pp.4963-4973.
- Nazeer, H., Abelmann, L., Tas, N.R., van Honschoten, J.W., Siekman, M.H. and Elwenspoek, M.C., 2009. Determination of young's modulus of pzt and co80ni20 thin films by means of micromachined cantilevers. In *20th Micromechanics Europe Workshop, MME 2009* (pp. 278-281). LAAS-CNRS.
- Newton, D., Garcia, E. and Horner, G.C., 1998. A linear piezoelectric motor. *Smart Materials and Structures*, 7(3), p.295
- Park, Y., Daneshpajoo, H., Scholehwar, T., Hennig, E. and Uchino, K., 2020. Physical Parameter and Loss Determination of Piezoceramics Using Partial Electrode: k31 and k33 Mode Cases. *arXiv preprint arXiv:2012.07053*.
- Paulsen, F. and Welo, T., 2001. Cross-sectional deformations of rectangular hollow sections in bending: part II—analytical models. *International journal of mechanical sciences*, 43(1), pp.131-152.
- Peng, P., Sezen, A.S., Rajamani, R. and Erdman, A.G., 2010. Novel MEMS stiffness sensor for force and elasticity measurements. *Sensors and Actuators A: physical*, 158(1), pp.10-17.
- Peters, H. J., 2016. A Controllability Approach for Resonant Compliant Systems. PhD thesis, <https://repository.tudelft.nl/islandora/object/uuid%3A76b5467e-63ba-4fb6-bc4c-4f2f8548ff95?collection=research>
- Phule, P.P. and Ginder, J.M., 1998. The materials science of field-responsive fluids. *MRs Bulletin*, 23(8), pp.19-22.
- PolyK, 2023. PolyK Piezo PVDF Properties. <https://piezopvdf.com/piezoelectric-poled-pvdf-film-d31/>
- Pornsirak, T. Nick, et al., 2001. Microbat: A palm-sized electrically powered ornithopter. *Proceedings of NASA/JPL workshop on biomorphic robotics, Vol. 14*.
- Preumont, A., 2018. *Vibration control of active structures: an introduction* (Vol. 246). Springer.
- Proto, A., Fida, B., Bernabucci, I., Bibbo, D., Conforto, S., Schmid, M., Vlach, K., Kasik, V. and Penhaker, M., 2016, December. Wearable PVDF transducer for biomechanical energy harvesting and gait cycle detection. In *2016 IEEE EMBS Conference on Biomedical Engineering and Sciences (IECBES)* (pp. 62-66). IEEE

- Ramaratnam, A., Jalili, N. and Dawson, D.M., 2004, June. Semi-active vibration control using piezoelectric-based switched stiffness. In *Proceedings of the 2004 American control conference* (Vol. 6, pp. 5461-5466). IEEE
- Ras, M., Design, 2019. Fabrication and Testing of a Resonant Flapping-Wing Micro Air Vehicle. Literature survey
- Sabarianand, D.V., Karthikeyan, P. and Muthuramalingam, T., 2020. A review on control strategies for compensation of hysteresis and creep on piezoelectric actuators based micro systems. *Mechanical Systems and Signal Processing*, 140, p.106634.
- Sapin, L., Abolade, O., Willemstein, N., van Rijen, L., 2013. Wing control of a Flapping Wing Micro Air Vehicle (FWMAV) using piezoelectrics. BSc Thesis
- Schwab, A. L. & Meijaard, J. P., 2006. How to draw Euler angles and utilize Euler parameters. In *proceedings of IDETC/CIE ASME 2006 International Design Engineering Technical Conferences & Computers and Information in Engineering Conference*, pp. 1–7. Philadelphia, Pennsylvania, USA.
- Shin, Y.H., Jung, I., Park, H., Pyeon, J.J., Son, J.G., Koo, C.M., Kim, S. and Kang, C.Y., 2018. Mechanical fatigue resistance of piezoelectric PVDF polymers. *Micromachines*, 9(10), p.503
- Smith, G.L., Pulskamp, J.S., Sanchez, L.M., Potrepka, D.M., Proie, R.M., Ivanov, T.G., Rudy, R.Q., Nothwang, W.D., Bedair, S.S., Meyer, C.D. and Polcawich, R.G., 2012. PZT-based piezoelectric MEMS technology. *Journal of the American Ceramic Society*, 95(6), pp.1777-1792.
- Snodgrass, R.E., 2018. *Principles of insect morphology*. Cornell University Press.
- Structx, 2022. Hollow Oval – Geometric Properties. [https://structx.com/Shape\\_Formulas\\_035.html](https://structx.com/Shape_Formulas_035.html)
- Sul, O., Choi, E. and Lee, S.B., 2017. A portable stiffness measurement system. *Sensors*, 17(11), p.2686.
- Tabata, O., Konishi, S., Cusin, P., Ito, Y., Kawai, F., Hirai, S. and Kawamura, S., 2001. Micro fabricated tunable bending stiffness devices. *Sensors and Actuators A: Physical*, 89(1-2), pp.119-123.
- Tatum, J. B., 2013. *Classical Mechanics*. University of Victoria.
- Tinjum, J.M. and Christensen, R.W., 2011. Site investigation, characterization and assessment for wind turbine design and construction. In *Wind energy systems* (pp. 28-45). Woodhead Publishing.
- Tse, T. and Chang, C.C., 2004. Shear-mode rotary magnetorheological damper for small-scale structural control experiments. *Journal of structural engineering*, 130(6), pp.904-911.
- Ueda, J., Secord, T.W. and Asada, H.H., 2009. Large effective-strain piezoelectric actuators using nested cellular architecture with exponential strain amplification mechanisms. *IEEE/ASME transactions on mechatronics*, 15(5), pp.770-782.
- Van Vrede, D., 2018. flight control and collision avoidance for quadcopter and flapping wing MAVs using only optical flow. Master Thesis
- De Vicente, J., Klingenberg, D.J. and Hidalgo-Alvarez, R., 2011. Magnetorheological fluids: a review. *Soft matter*, 7(8), pp.3701-3710.
- Walsh, P.L. and Lamancusa, J.S., 1992. A variable stiffness vibration absorber for minimization of transient vibrations. *Journal of sound and vibration*, 158(2), pp.195-211.

- Wang, B.T. and Rogers, C.A., 1991. Modeling of finite-length spatially-distributed induced strain actuators for laminate beams and plates. *Journal of Intelligent Material Systems and Structures*, 2(1), pp.38-58.
- Wang, H., Li, Y., Wang, X., Liu, Z., Ahmed, M.F. and Zeng, C., 2021. Preparation and Characterization of Piezoelectric Foams Based on Cyclic Olefin Copolymer. *Engineered Science*, 16, pp.203-210.
- Wang, Qi., 2017. Modeling, design and optimization of flapping wings for efficient hovering flight. <https://repository.tudelft.nl/islandora/object/uuid%3Ae6fc3865-531f-4ea9-aeff-e2ef923ae36f?collection=research>
- Ward, Thomas A., et al., 2015. A review of biomimetic air vehicle research: 1984-2014. *International Journal of Micro Air Vehicles*, 7.3, p. 375-394.
- Ward, Thomas A., et al., 2017. A bibliometric review of progress in micro air vehicle research. *International Journal of Micro Air Vehicles*, 9.2, p. 146-165.
- Warner, A.W., Onoe, M. and Coquin, G.A., 1967. Determination of elastic and piezoelectric constants for crystals in class (3 m). *The journal of the acoustical society of America*, 42(6), pp.1223-1231.
- Winslow, W.M., 1949. Induced fibrillation of suspensions. *Journal of applied physics*, 20(12), pp.1137-1140.
- Wood, R.J., 2007, October. Design, fabrication, and analysis of a 3DOF, 3cm flapping-wing MAV. In *2007 IEEE/RSJ international conference on intelligent robots and systems* (pp. 1576-1581). IEEE.
- Wu, C.M., Chou, M.H. and Zeng, W.Y., 2018. Piezoelectric response of aligned electrospun polyvinylidene fluoride/carbon nanotube nanofibrous membranes. *Nanomaterials*, 8(6), p.420.
- Vlab. 2011. Free Vibration of a Cantilever Beam (Continuous System). Retrieved 7 February 2023, from [vlab.amrita.edu/?sub=3&brch=175&sim=1080&cnt=2065](http://vlab.amrita.edu/?sub=3&brch=175&sim=1080&cnt=2065)
- Xu, Z., Wang, Y. and Chen, C., 2018. Micro converter with a high step-up ratio to drive a piezoelectric bimorph actuator applied in mobile robots. *International Journal of Advanced Robotic Systems*, 15(2), p.1729881418763458.
- Yang, G.Y., Wen, Y.H., Foldy, C., Tang, W.C. and Soltesz, I., 2008. Sensor for stiffness measurements within the adult rat hippocampus. *IEEE Sensors Journal*, 8(11), pp.1894-1899.
- Ye, Z.G. ed., 2008. *Handbook of advanced dielectric, piezoelectric and ferroelectric materials: Synthesis, properties and applications*. Elsevier
- Zhang, S., Liu, L., Li, M., Zhang, Y., Tang, J. and Yi, X., 2021. Stick-slip nucleation triggering of Wenchuan earthquake. *Geodesy and Geodynamics*, 12(1), pp.11-20.
- Zhu, X., Jing, X. and Cheng, L., 2012. Magnetorheological fluid dampers: a review on structure design and analysis. *Journal of intelligent material systems and structures*, 23(8), pp.839-873.
- Zinoviev, P.A. and Ermakov, Y.N., 2018. *Energy dissipation in composite materials*. Routledge

# Appendix A: Hinge Construction

A mentioned in Chapter 4 the hinge is constructed from three materials:

- *Conducting layers:* Spring steel
- *Adhesion:* 3M 7955MP Double Lined Adhesive Transfer Tape
- *Piezoelectric material:* PolyK Uniaxially Poled PVDF Film

The only machinery used in the assembly process is a Lasea laser cutter, shown in Figure 66.



Figure 66: Lasea laser cutter.

The first step is to cut the shape shown in Figure 67 out of the adhesion film.

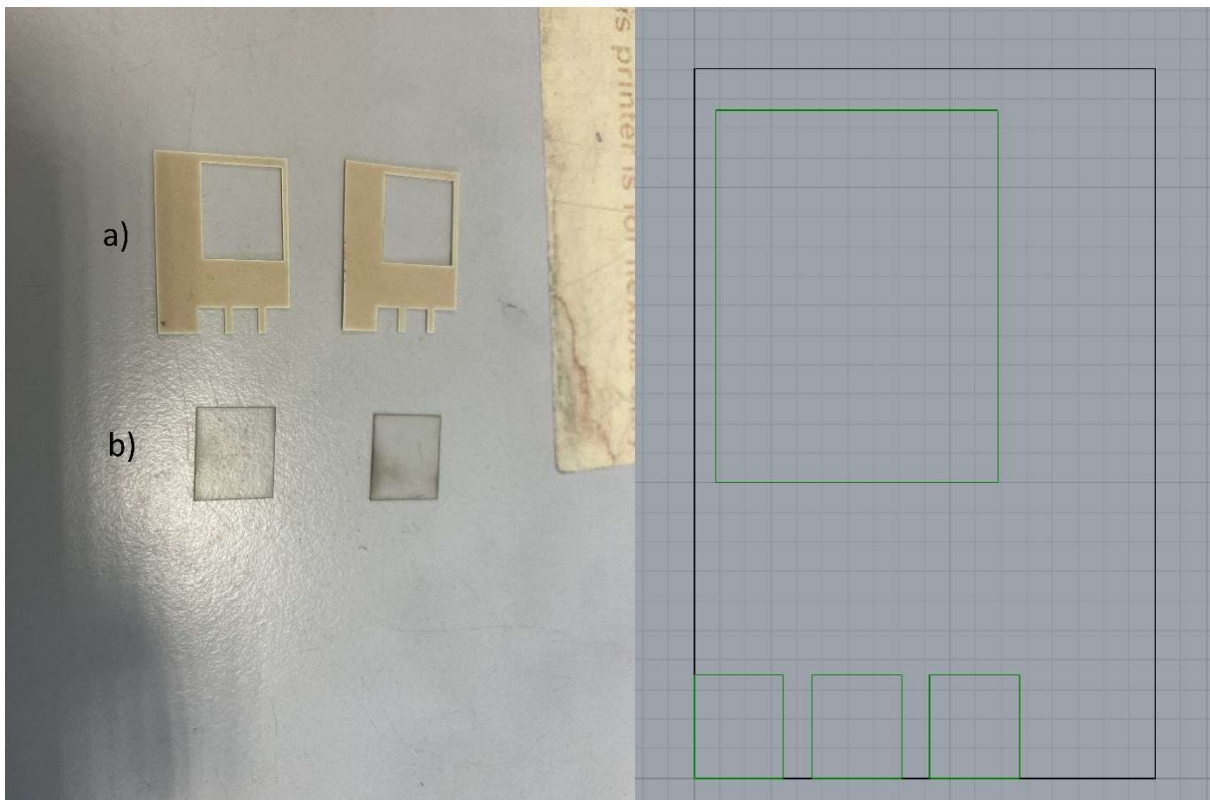


Figure 67: The cut shape for the adhesion layer, and the corresponding cut adhesion film (a). b) Shows the cut PVDF film.

Next, one of the liner layers is removed and a strip of steel sheet is affixed on top of the cut part of the adhesion film. A rectangle is cut out of the PVDF film, and placed in the corresponding hole in the adhesion film, shown in Figure 68.



Figure 68: Adhesion layer on top of steel strip, with PVDF film placed in the corresponding hole.

The second liner layer is removed and another strip of steel film is attached. On top of this, the next layer of cut adhesion film can be placed to repeat the process, including inserting the second piece of PVDF in the second adhesion layer. The final steel strip is placed on top, and the laser cutter cuts out the pattern shown in Figure 69.

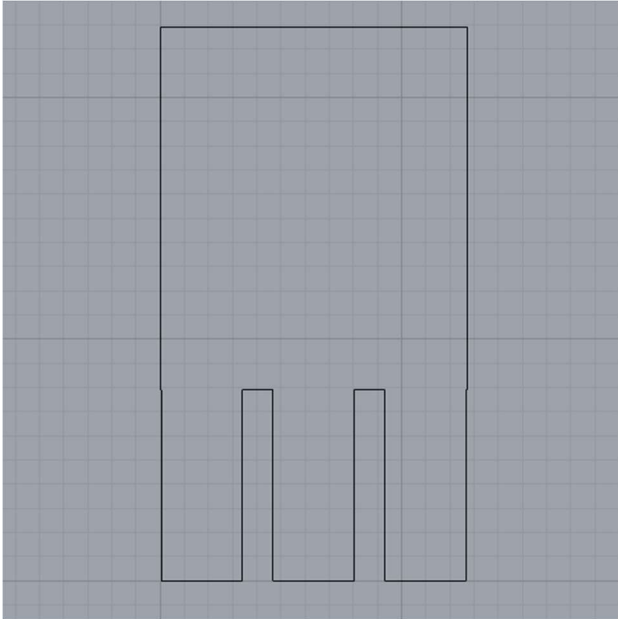


Figure 69: Laser cut through all layers to form the final shape of the hinge.

The hinge is almost done but still has three layers of steel at every contact. The final step is to cut away two of the three steel layers at the contacts so that each layer has one contact. Three complete hinges were assembled, shown in Figure 70.

The hinges are tested using a multimeter to make sure there is no short-circuiting between the layers.



Figure 70: Three final hinge prototypes.

## Appendix B: Experimental Set-up

The experimental set-up consists of the following components:

Table 17: Experimental set-up components.

Number	Component
1	Support structure built from Thorlabs components
2	RS Pro linear solenoid
3	Tektronix TDS 2024 oscilloscope
4	Delta Elektronika D5
5	Custom printed circuit board
6	OptoNCDT 1420 smart laser
7	National Instruments USB-6008 multifunction I/O device
8	Delta Elektronika ES300 power supply
9	Computer with Labview installed

Figure 71 shows the schematic drawing of the set-up based on the methodology discussed in Section 5.2. Figure 72 shows the set-up and its components. Figure 73 shows the Labview interface.

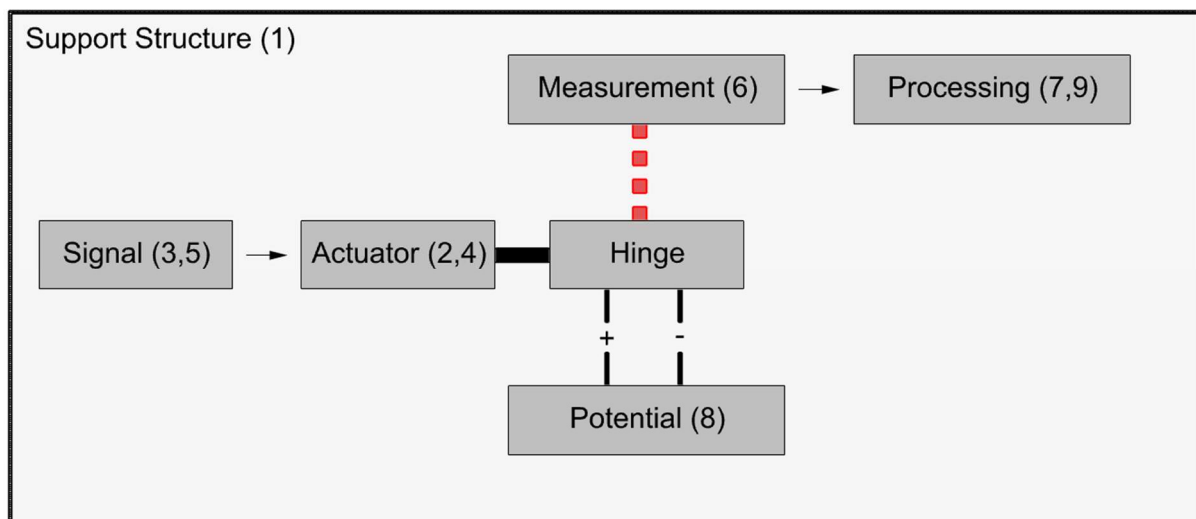


Figure 71: Schematic drawing of the experimental set-up.



Figure 72: Photo of the experimental set-up.

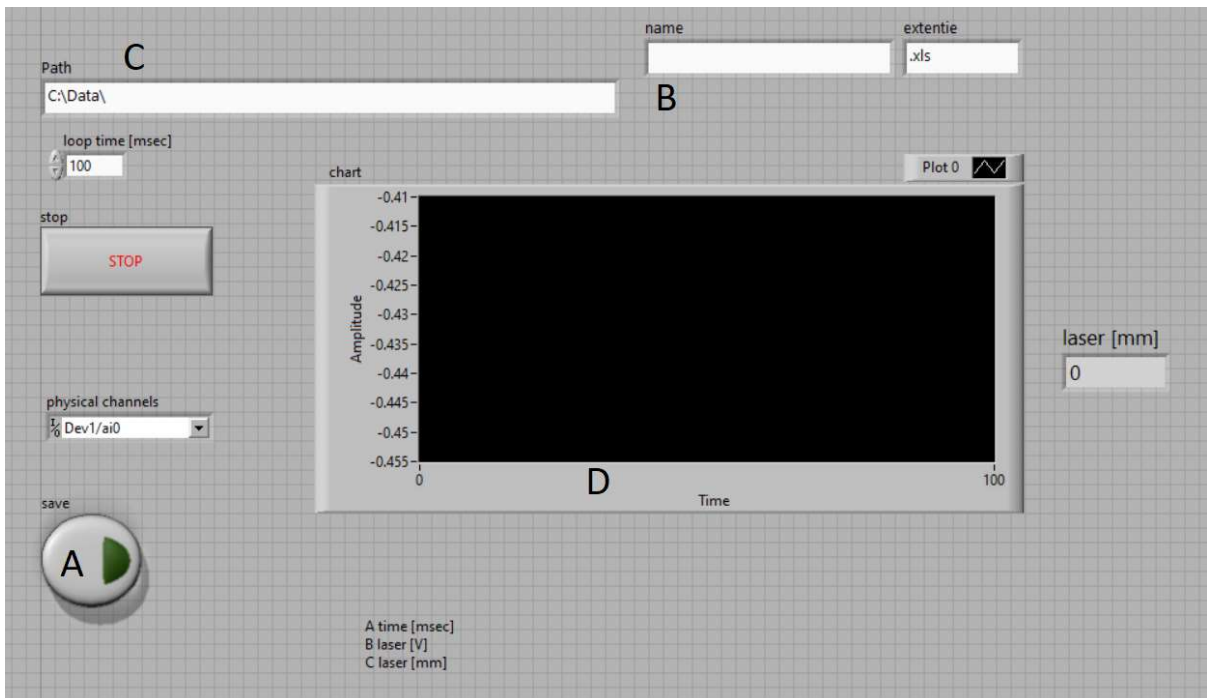


Figure 73: Labview interface.

The measurements were executed using the following method:

1. Turn on the Labview interface (shown in Figure 73).

2. Set the frequency of the signal generator (number 3).
3. Turn on the power supply to the actuator (number 4).
4. Toggle the measurement recording in Labview (button A).
5. Wait 8 seconds, then toggle of measurement recording (button A again).
6. Change frequency on signal generator (number 3).
7. If not at the final frequency of the measuring range, go back to step 4.
8. Remove data from excel sheet for processing.

The data was saved to an excel workbook, which could be named using field B, and would be saved in a location detailed in field C. The monitor D in the Labview interface could be used to check displacements in real time and judge if the structure was near its eigenfrequency.

The hinges were attached to the actuator in the following way. The actuator plunger had a M1.6 wire twisted into it. A M1.6 bolt was glued to thin metal strip using contact glue. This strip was then glued to the hinge to simulate a fixed constraint. The long metal strip for tuning the eigenfrequency and increasing the displacements was glued to the other side of the hinge. A fully prepared hinge is shown in Figure 74.

The laser was set-up to measure about halfway of the strip, to make sure the deflection stays within the 10 mm measuring range.



Figure 74: Photo of a hinge with additional components glued to it.

The electric potential was applied to the outer layers of the hinge using the Delta Elektronika ES300 (number 8). The potential was transferred to the spring steel using crocodile clips, shown in figure 75. The red clips carried a potential of 30 V and the black clip connected the middle layer to ground.

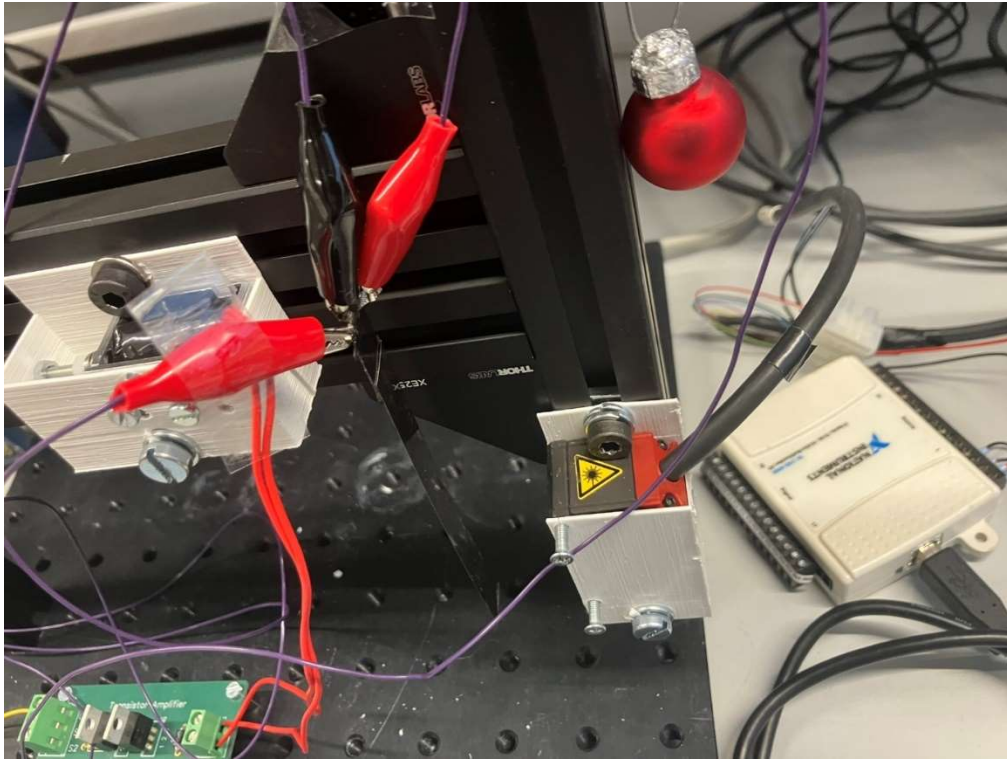


Figure 75: Crocodile clips transferring electric potential to the hinge.